Design of a Two-Stage Level-Two Bidirectional On-Board Battery Charger for Plugin Vehicles

by

Noreen Nga-Yee Wong

A thesis
presented to the University of Waterloo
in fulfillment of the
thesis requirement for the degree of
Master of Applied Science
in
Electrical and Computer Engineering

Waterloo, Ontario, Canada, 2013

I hereby declare that I am the sole author of this thesis. This is a true copy of the thesis, including any required final revisions, as accepted by my examiners.

I understand that my thesis may be made electronically available to the public.

Abstract

Depletion of fossil fuel reserves, increasing awareness of air pollution levels and continuous rise in gasoline prices are some of the major drives that have been revolutionizing the automotive industry since the last decade. These factors combined are causing conventional automobiles with internal combustion engines (ICE) to be replaced with plugin vehicles. The on-board rechargeable battery packs in plugin vehicles can be recharged by connecting to the utility grid using a plug. The energy stored in the on-board battery packs has attractive benefits for grid support, and this promotes the idea of Vehicle-to-Grid (V2G). V2G power transactions allow energy from the on-board battery packs to be sent back to the utility grid for support in peak shaving and provide reactive power compensation. One natural consequence that arises with the introduction of V2G is a sharp increase in the need for high-performance power electronic interface between the utility grid and the battery pack. Therefore, research on bidirectional battery chargers for plugin vehicles is imperative in order to aid in the promotion of V2G. This thesis focuses on the design and development in a two-stage level-two on-board bidirectional battery charger.

This research first conducts a literature review in existing bidirectional battery charger topologies, and discusses the three standardized charging levels. Then, the specifications of the developed battery charger are described. A detailed analysis in the electrical circuit battery model is presented to characterize the steady-state and transient behaviours of Li-ion, NiMH and lead-acid batteries.

With regards to the AC-DC converter design, it is important to choose an appropriate converter topology and design a controller that is customized for a bidirectional battery charger. Thus, this thesis presents three controller designs. Their performances are analyzed and compared based on their ability to perform sinusoidal current waveshaping, voltage regulation at the dc-link, and power factor control (not necessarily unity).

With regards to the DC-DC converter design, it is desirable to select a converter topology that has low cost, high power capability, high efficiency, low weight and small volume. Therefore, six different DC-DC converter topologies are analyzed and compared. Two bidirectional battery charger designs are proposed.

Lastly, experimental results of a lab prototype of a full-bridge DC-DC converter are provided. The experiment results demonstrate the operation of three modes of operation: constant-current (CC) charging, constant-voltage (CV) charging and discharging as well as bidirectional power transfer.

Acknowledgements

I would like to express my deepest gratitude to my family. They have always encouraged me to follow my interest and given me the freedom to pursue my dreams. Words cannot express for appreciation for them. I especially want to thank my sister, Irene, for supporting me to pursue graduate studies. You are more than a sister to me!

I am forever grateful for Wallace, my love, who has always been by my side throughout the last two years in my graduate studies to share all the successes and setbacks in my research. Your words of encouragement and your confidence in me have led me to overcome all the obstacles. You are the 'WALL' that I can always lean on.

I would also like to extend my gratefulness to my supervisor, Dr. Mehrdad Kazerani. The creation of this thesis would not have been possible without his close guidance and continuous support. He is a caring, encouraging and a highly approachable supervisor. I want to thank him for helping me whenever I hit a road block in my research and motivating me to strive for the best.

I would like to acknowledge Kun Zhuge for his assistance in making the converter prototype.

My graduate studies has been supported by Ontario Graduate Scholarship. I would like to thank the Selection Board for selecting me and see the potentials in my research.

I want to recognize the support from all my friends. Lily, Yuki and Alice, thank you for all the caring and the crazy moments! Thomas, Abraham, Jeffrey and Osman, thank you for helping me so much in and outside of the classrooms. Patrick, Kenneth and Ronald, thank you for your continuous words of encouragement. Lastly, a big thank you for those who have also helped and motivated me throughout my graduate studies.

Dedication

I dedicate this thesis to my dad, Chak-Man, my mom, Lavinia, my sister, Irene and my love, Wallace.

Table of Contents

List of Tables

List of Figures

Chapter 1

Introduction

1.1 Motivation

Depletion of fossil fuel reserves, increasing awareness of air pollution levels and continuous rise in gasoline prices are some of the major drives that have been revolutionizing the automotive industry since the last decade. These factors combined are causing conventional automobiles with internal combustion engines (ICE) to be replaced with newer and cleaner technologies.

A report released in 2004 by U.S. Energy Information Administration indicates that most, if not all, of Earth's prolific petroleum basins are identified and are partially to near-fully explored. Moreover, all or nearly all of largest oil fields are already in production [1]. To further extend the seriousness of this issue, this report also reveals that the demand of the world crude oil has been growing at an annualized compound rate slightly over 2% in recent years. The highest demand growth rate belongs to developing nations, such as China, India, Africa and South America. At this rate of demand growth, it is expected that by year 2037 the world's conventional crude oil production will reach its peak at a volume of 53.2 billion barrels per year [1].

Another report, written by Department of Infrastructure, Transport, Regional Development and Local Government of Australian Government, states that the world crude oil production will reach its peak in 2016 [2]. After year 2016, the model is forecasting a "the 2017 drop-off", which is a long decline in oil production beginning in 2017.

Despite the discrepancy predicted by various government bodies regarding the year when the oil production will reach its peak, the fundamental issue is that the limited supply of crude oil will not satisfy the increasing demand. Based on the economic model in supply and demand, a continuing increase in oil prices can only be observed in the near future. Figure 1.1 shows the average crude oil prices from year 1990 to present. It can be seen that the oil price has risen more than 2.5 times in the last decade using inflation adjusted prices.

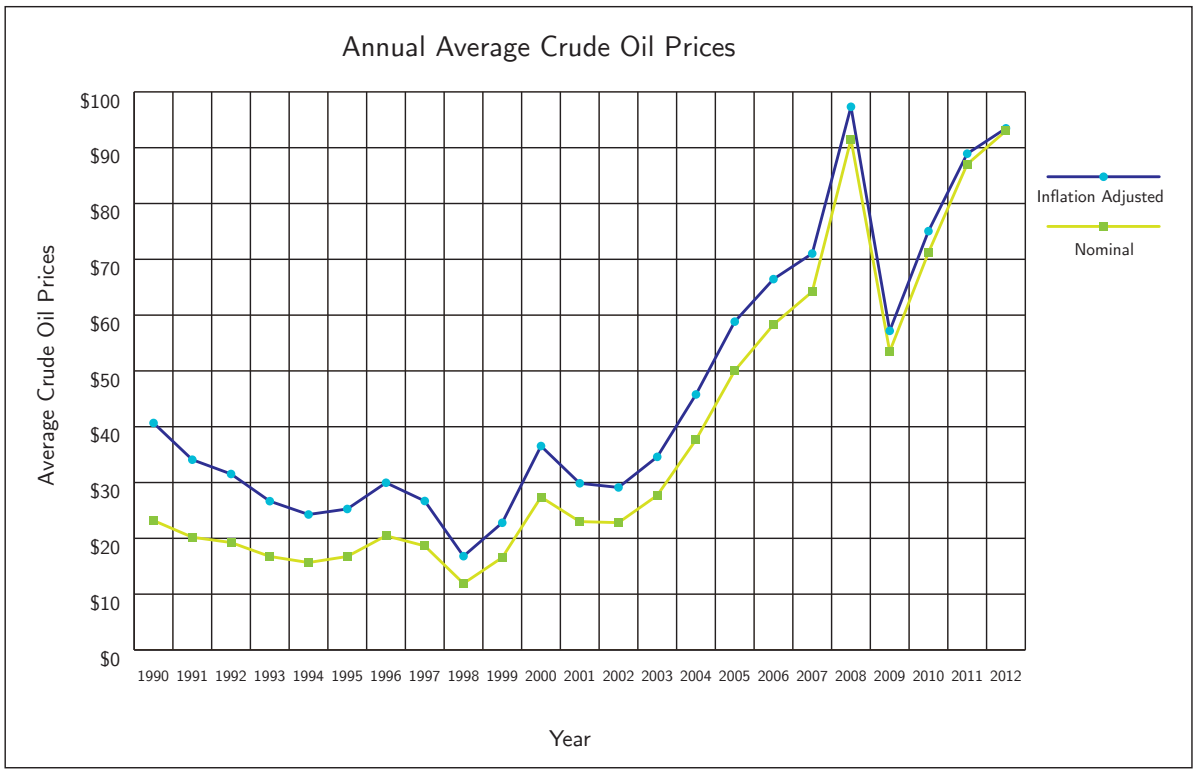

Figure 1.1: Annual average crude oil prices [3]

Other than the concerns of diminishing supply of reserve and increase in prices, some serious adverse environmental effects are also associated with using oil as the main source of energy. Burning fossil fuels creates carbon dioxide (CO_2) emissions that contribute to global warming, and other air pollutants like nitrogen oxides, sulfur dioxide, volatile organic

compounds, and etc [4]. These substances are known as the greenhouse gases. According to a publication by the Intergovernmental Panel on Climate Change, "greenhouse gas (GHG) emissions resulting from the provision of energy services have contributed significantly to the historic increase in atmospheric GHG concentrations" [5]. This publication further concludes that "Most of the observed increase in global average temperature since the mid-20th century is very likely due to the observed increase in anthropogenic greenhouse gas concentrations." [5]. Fossil fuel burning is also directly responsible for the formation of acid rains and they are the most predominant contributors to environmental pollution, mainly in the form of water pollution [4]. It is estimated that about 40% of deaths worldwide are caused by water, air and soil pollution. Therefore, the soceity has an urgent need to shift to using renewable energies in order to reduce oil dependency.

The number of vehicles worldwide surpassed 1 billion in 2010 and the United States constitutes the largest vehicle population with 239.8 million of cars [6]. Conventional automobiles with ICE consume one third of world's oil production [7]. Being such a major consumer of oil, it is imperative that the automotive industry shift to other powertrain technologies to reduce oil consumption and reduce greenhouse gas emissions.

One solution to shift away from using ICE's is to electrify the vehicles. This implies that part or all of the oil-powered powertrain of the car is replaced by electric propulsion technology. Electrification has become more realizable with battery advancement to increase power density and storage capability as well as the ability for faster charging time. The roadmap to transitioning to having only all-electric vehicles on the road will be a lengthy journey due to existing technology and infrastructure, and more importantly, the general public's reluctance to change. Nonetheless, the automotive industry and government are actively promoting vehicle electrification by offering more plugin hybrid electric vehicle (PHEV) and electric vehicle (EV) models combined with government incentives to lower the retail prices in order to attract consumer interest. More technical details about PHEVs and EVs will be given in Section 1.2.1.

Vehicle electrification provides an effective solution for reducing fossil fuel dependency, increasing environmental friendliness due to low tailpipe emissions and higher energy efficiency [8]. Batteries in PHEVs and EVs can also be recharged using renewable sources of energy, such as solar, wind, and geothermal heat. However, vehicle electrification faces some challenges, mostly related to the battery storage system. In general, the driving range for EVs are much lower than those for ICE vehicles, the full recharging time of the

EV battery pack takes significantly longer than refuelling gasoline in an ICE car and the current replacement cost for battery packs is still high. As a result, battery development is one of the determining factors for mainstream market to accept PHEVs and EVs.

1.2 Background Information

1.2.1 Electric Vehicles and Plug-in Hybrid Electric Vehicles

An electric vehicle (EV) is a vehicle that utilizes rechargeable battery packs to power one or more electric propulsion motors. These rechargeable battery packs can be refueled either by directly connecting to the utility grid or by interfacing with a charging station. Development of EVs was dated back in the 1800s; in fact, EVs were among the earliest automobiles. However, due to the limitation of energy storage technology and the cost of production at that time, EVs were being dominated by ICE vehicles. The drivetrain in an EV is similar to that found in a conventional ICE vehicle, with both consisting of transmission elements and propulsion unit. The major difference in their drivetrain configurations lies in the propulsion unit; the ICE in a conventional vehicle is replaced by electric motor(s) in EV drivetrain. Such configuration allows EVs to achieve zero tailpipe emissions. However, similar transmission elements can be found in both types of vehicles, namely the gearbox, differential, half-shafts and wheels. A typical layout of EV drivetrain is shown in [9]. Examples of EVs that are currently in production include Nissan Leaf, Ford Focus Electric and Tesla Roadster.

A plugin hybrid electric vehicles (PHEV) is a hybrid vehicle that shares the characteristic of a conventional hybrid vehicle with an ICE and an electric motor and that of an all-electric vehicle to utilize a plug to recharge the on-board battery pack. PHEVs are intended to act as a catalyst to form a smooth transition from conventional vehicles to all-electric vehicles. Studies have shown that 80% of average Americans drive less than 40 miles per day [10]; thus, PHEVs are primarily designed to meet this daily driving requirement with their on-board battery pack. In situations where extended driving range is required, the reliability of PHEVs is secured through the on-board fuel tank and the ICE to power the drivetrain.

The drivetrain of a PHEV has three possible configurations: parallel, series and series-parallel. In parallel hybrid systems, both the ICE and electric motor are coupled together

to drive the wheels. They are joined together by two axes in parallel, such that the speed at each axis must be identical and their supplied torques are added together. In a series configuration, the vehicle is only driven by an electric motor. The ICE is solely responsible to drive an electric generator to charge the battery pack and is not coupled to the wheels. Therefore, a series hybrid electric vehicle requires a larger battery pack. Currently, the Chevrolet Volt uses this configuration. Lastly, the series-parallel configuration combines the advantages and complications of series and parallel configurations. In this design, both the ICE and electric motor can drive the wheels directly (similar to parallel configuration); however, the ICE can be disconnected from the system so that only the electric motor is coupled to the wheels (like in series configuration) [11]. The Toyota Prius Plug-in Hybrid is an example that uses this design. Figures for he three different PHEV drivetrain configurations are shown in [9].

1.2.2 Battery Chargers

One important component in an EV or PHEV is the battery charger. It acts as an interface between the electrical source and the vehicle's battery pack. Typically, this electrical source is the utility grid for recharging EVs or PHEVs. Its main responsbility is to restore the charge in the battery pack. The design of the battery charger plays a significant role in the charging time of the battery pack and the quality of power that the battery pack receives. It is desireable to minimize the charging time while maintaining the quality of power as well as prolonging the battery pack's lifetime.

1.2.3 Vehicle-to-Grid

Conventional electric power system infrastructure does not have any storage systems; the generated power is transmitted and distributed continuously to meet the demands with minimal idle time. It has been found that conventional vehicles are used for only 4% of the time for daily commute [12]. Revealing this untapped idle time can lead to some potential benefits. The unused energy stored in the on-board battery is excellent spinning reserves for unexpected power peaks when the vehicle is not driven. This concept of feeding power to the grid from the on-board battery pack is known as Vehicle-to-Grid (V2G). Even though V2G power transactions have not been realized to date, the idea has gained much

interest from both academia and industry because the energy stored in the battery packs has the advantages of quick response, low standby cost and low capital cost per kW. Although peak shaving is viewed as the most attractive benefit of V2G, other potential benefits that it can provide include voltage support, harmonic filtering and reactive power compensation [13–15].

The concept for V2G is based on the principle that PHEVs and EVs will be charged overnight when the power demand is low. During the day, particularly in the morning and evening, the vehicles will be driven for their daily commutes, and will be plugged-in during the time the vehicles are not driven. The discharging of the on-board battery pack to the grid will depend on the grid load demand; however, it is predicted that V2G power transfer will not be a day-to-day activity.

Obstacles for Implementing V2G

Despite the fact that of V2G can provide many potential benefits to the power system, it also faces many obstacles and challenges before it can be fully implemented within the current systems. These obstacles and challenges are summarized in this section.

Infrastructure upgrade: Upgrade to existing infrastructure is necessary to deploy V2G, both on the utility grid side and household side. Existing power infrastructure is designed to have unidirectional power flow where power is transmitted from the point of generation to the distribution lines, and finally to the loads. High penetrations of plugin vehicles with V2G power transactions may overload substation equipment, such as transformers, and may cause power quality issues at the point of common coupling. In both cases, infrastructure upgrade is required to secure a stable and reliable system. Auxiliary upgrades in individual household are also required in order to meet the ampere requirement for the battery charger as well as control requirements. However, this leads to the "chicken and egg scenerio". No utility would want to spend millions of dollars to upgrade infrastructure without popular interest from the public. On the other hand, no consumer would want to buy a plugin vehicle if they are responsible to pay for the household infrastructure upgrades in order to support V2G.

User control: Consumers should have the freedom to control their charging and discharging preferences based on their schedules and needs. As a result, a standardized

communication protocol must be established in order for a reliable bidirectional communications to occur between the utility control centre and the vehicles. In this way, consumers can select their willingness to participate in V2G transactions, as well as the time frame and the amount of power they are willing to send back to the grid.

Battery degrades: Adding addition discharging cycles to the battery accelerates its end of lifespan. Each battery is designed to only have a certain number of cycles, where a cycle refers to a sequence in which a charged battery is discharged and then is recharged. Currently, the price of the on-board battery pack still constitutes a significant part of cost of the vehicle. Having V2G power transactions will likely cause the frequency for battery replacement to increase, resulting in the need to replace the battery pack during the lifetime of a PHEV or EV.

Incentives: Consumers' acceptance of transitioning to plugin vehicle and the concept of V2G heavily depends on the amount of incentives the government is providing. For example, the Feed-in Tariff (FIT) program initiated by the Ontario government in 2009 is an incentive-based policy designed to accelerate investment in renewable energy technologies by offering stable prices under long-term contracts. Ever since, it has successfully attracted many solar PV projects of various scales in Ontario. If the government can initiate similar incentive program by offering higher prices for V2G power, it will increase the pace that V2G is being implemented.

Round trip efficiency: The efficiency of V2G power transactions is a crucial concern for its realization. Round trip efficiency refers to the overall energy conversion efficiency of one cycle of charging the battery and discharging the battery. Suppose the battery charger has an efficiency of 85% for charging or discharging, the round trip efficiency would become 72.25% without considering the battery storage efficiency. The multiplication of efficiency for each conversion stage accounts for the low overall round trip efficiency and may not be an attractive factor for implementing V2G power transactions.

Charging stations: For plugin vehicle consumers, it is important to be able to charge their vehicles efficiently and at their convenience. Currently, charging facilities for plugin vehicle are very limited. Plugin vehicles are mainly confined to charging at their households due to long charging time. As such, before V2G can be implemented, charging stations must be made easily accessible and the charging time must be

relatively short. This refueling setup should resemble the current availability of gas stations and refueling time for conventional vehicles.

1.3 Research Objectives

A natural consequence with the introduction of V2G is a sharp increase in the need for high-performance power electronic equipment, including bidirectional battery chargers. In the thesis, the following objectives are going to be made to the advancements of bidirectional battery charger design:

1) A bidirectional on-board battery charger for use in all platforms of plugin vehicles, which minimizes volume, weight and cost with the detailed specifications outlined in Chapter **??**.

2) A comprehensive battery model that aids in the simulation of the battery charger, as well as experiment procedures that can extract battery model parameters for lithium-ion and lead-acid batteries.

3) A complete prototype of a full-bridge DC-DC converter to verify the performance and characteristics with the simulation results

1.4 Thesis Outline

This thesis is organized into eight chapters and two appendices. Chapter 1 has given an introduction to plugin vehicles and V2G power transactions, as well as the motivation for bidirectional battery charger research. Chapter 2 describes the different charging levels and performs a literature review on existing bidirectional battery charger topologies. Chapter 3 outlines the specifications of the bidirectional battery charger, and presents a battery model that can be used to model the transient and steady-state behaviour for these three types of batteries. This chapter also derives the general formulas for calculating the equivalent impedance of a battery pack. Chapter 4 discusses the topology selection for the AC-DC converter in the battery charger. In addition, this chapter formulates, analyzes and

compares three different controllers for the AC-DC converter. Chapter 5 compares six different DC-DC converters that are potential candidates for the battery charger, and presents the simulation results for two completed bidirectional battery charger designs. Chapter 6 presents the experimental results of the full-bridge DC-DC converter lab prototype. Lastly, the conclusions and future work are presented in Chapter 7. Appendix A provides the experimental procedures to extract parameters for the battery model. Appendix B provides implementation details for the lab prototype.

Chapter 2

Charging Levels and Existing Bidirectional Charger Topologies

2.1 Charging Levels

Battery chargers for plugin vehicles are commonly categorized by their level of charging. The charging level is a key factor that determines the time needed to charge a plugin vehicle battery pack and the type of charging interface required. Three levels of charging are standardized, known as Level 1, Level 2 and DC (Level 3) charging. Further explanations for each charging level are provided in this section and their characteristics are summarized in Table 2.1.

2.1.1 Level 1 Charging

Level 1 charging is the lowest charging level out of the three levels. This level of charging uses a standard electrical outlet, i.e., a single-phase, 120V AC supply with 12-16A maximum continuous current. Depending on the battery type and capacity, it can take up to 30 hours to fully recharge a plugin vehicle battery pack. As an example, an EV with a 24kWh battery will require approximately 20 hours to fully charge the battery from zero charge at the rate of 10A. Level 1 charging may not be a preferred means of charging because of its long recharging time, which can reduce performance [16]. However, because level 1

charging only requires standard electrical outlet, this avoids upgrade to current household electrical infrastructure and allows the battery charger to be on-board.

2.1.2 Level 2 Charging

Level 2 charging uses a 240V, single-phase or three-phase AC supply, with up to 80A of continuous current. This charging level requires an EVSE (electric vehicle supply equipment) and is more ideal for overnight charging. Depending on the battery type and capacity, level 2 charging can charge an EV in 4-8 hours. For example, an EV equipped with a 24kWh battery and a 240V/30A EVSE will require approximately 7 hours to fully recharge from zero charge at the rate of 14.5A.

2.1.3 Level 3 Charging (DC Charging)

Level 3 charging, better known as DC charging, is the highest standardized charging level. It uses a 480V DC supply with up to 160A of current. DC charging dramatically reduces the charging time; it is possible to fully charge an EV battery in as little as 10 minutes at the rate of 160A. However, the power level required for DC charging is beyond the capacity of those utility transformers that serve residential areas, and as such, in order to accommodate this level of charging, utility infrastructure upgrades are required. Furthermore, a battery charger using DC charging can only be in an off-board configuration because of the power equipment it demands.

Table 2.1: Charging standards

Charging Level	Level 1	Level 2	Level 3 (DC Charging)
Type	AC	AC	DC
Phase	Single	Single / Three	-
Voltage	120V	208-240V	480VDC
Current	12-16A	80A	100A+
Structure	On-board	On-board	Charging Station
Charging Time	8-30 hours	4-8 hours	as little as 10 minutes

2.2 Literature Review of On-Board Bidirectional Battery Charger Topologies

V2G power transactions cannot be facilitated without a bidirectional battery charger. The characteristics of a battery charger are strongly linked to the charging time and the quality of power [17, 18]. On-board chargers are the preferred configuration for plugin vehicles because of their suitability for household charging. Other than level of charging, on-board battery chargers are also classified by their structures, either as single-stage topology (with an AC-DC converter interfacing the battery pack with the grid) or two-stage topology (with an AC-DC converter on the grid-side, cascaded with a DC-DC converter on the battery-side). Regardless of the charger structure type, any bidirectional charger topology must be able to realize unity power factor at the grid interface and produce a regulated dc voltage. In this section, a review of on-board battery charger topologies reported in literature is presented.

2.2.1 Single-Stage Topologies

Single-stage topology offers the simplest structure for a battery charger with the lowest component count. Figure 2.1 shows the basic block diagram of a single-stage battery charger configuration. When compared with two-stage topology, this configuration is attractive due to to reduced volume and weight of the battery charger and increased efficiency as a result of reduced switching losses. The most common bidirectional topologies used in single-stage chargers are half-bridge, full-bridge and multilevel converters. Different variations of each topology have been developed and extensively reviewed in [19]. Despite variations existing for each topology, the basic concept behind different designs remains the same.

Figure 2.1: Single-stage battery charger configuration

Half-Bridge AC-DC Converter

This topology, shown in Figure 5.3, is the simplest of all bidirectional AC-DC converters. It utilizes two controllable switches to achieve boost conversion from ac side to dc side [20]. It is capable of operating with sinusoidal current of unity power factor and producing a regulated dc voltage. The controllable switches are controlled to generate a two-level PWM waveform varying between $V_{DC}/2$ and $-V_{DC}/2$ between the middle points of the switch leg and capacitor leg. The drawbacks of this topology are high voltage stress on the switches (equal to the dc-side voltage) and the fact that the current rating of the switches has to be equal to the peak value of the sinusoidal current. The two capacitors on the dc-side must also be large enough to allow the regulation of the dc voltage with low ripple contents. However, large size capacitors add weight and increase the size of the charger.

For unity power factor operation, the controller of a half-bridge converter has to produce a sinusoidal current reference waveform that is either in phase or 180° out of phase with the utility voltage depending on the intended direction of power flow. In addition, the output dc voltage must also be maintained at a desired level. In order to achieve this, the error between the dc-side voltage and its reference signal is passed through a PI controller and multiplied by a signal derived from the sinusoidal source voltage to produce the current reference [21]. This current reference is compared with the actual current to produce the PWM signals for controlling the switches.

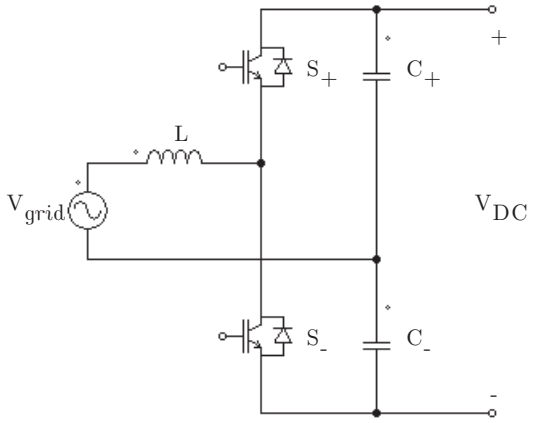

Figure 2.2: Half-bridge AC-DC converter

Full-Bridge AC-DC Converter

From the complexity point of view, a full-bridge AC-DC converter falls between the half-bridge and multilevel converters. With proper control, a three-level PWM waveform can be generated that assumes 0 and $\pm V_{DC}$, i.e., twice that in a half-bridge converter. Consequently, for the same power level, the switch current can be one-half of that in a half-bridge converter, making it more suitable for high power applications. The full-bridge converter is inherently a boost rectifier with power factor correction capability. A large capacitor is generally needed on the dc-side to reduce the ripple contents. Figure 2.3 shows the full-bridge converter topology.

The output dc voltage of the full-bridge converter contains a low frequency harmonic component at twice the grid frequency because of the imbalance between the input ac power and output dc power. Additional filters, such as active filter and notch filter [22], may be needed to filter out this harmonic component since it may create ripples that are too high to apply to the battery.

The controller for the full-bridge converter functions in a manner identical to that described for half-bridge converter. The only difference is that the two legs of the full-bridge converter can be controlled using PWM with either bipolar voltage switching or PWM with unipolar voltage switching.

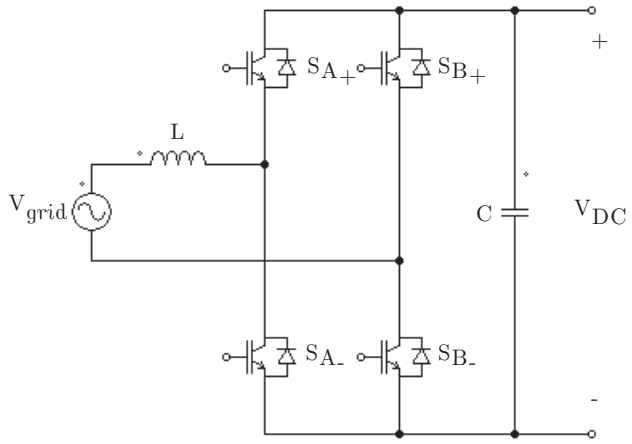

Figure 2.3: Full-bridge AC-DC converter

Multilevel PWM AC-DC Converter

Another type of boost AC-DC converter is the multilevel PWM converter. This topology offers advantages over the previous two topologies in terms of low voltage stresses on the switches, reduced switching losses due to reduced switching frequency, reduced harmonics, higher power factor on ac-side and better regulated, ripple-free dc-side voltage. Multilevel converters are suitable for high-power, high-voltage applications. The drawbacks include control complexity and high power circuit cost, making it difficult to justify for applications where one charging level is desired.

Four different single-phase three-level PWM AC-DC converters based on the half-bridge converter have been reported [23–26]. All of these converters are capable of regulating a dc-side voltage, as well as drawing sinusoidal current and achieving unity power factor on the ac side. These four converter topologies are briefly described in the following.

Diode Clamped Converter The diode clamped topology [23] is shown in Figure 2.4(a). Each switch experiences a voltage stress of $V_{DC}/2$. An outer control loop control regulates the dc voltage and an inner control loop guarantees a high-quality sinusoidal current and a unity power factor at the interface of the utility grid. Experimental results from a lab prototype show that an efficiency of 90% and a power factor of 0.998 at the power level of 900W have been achieved.

Switched Clamped Converter The switched clamped topology [24] is shown in Figure 2.4(b). Two switches in this topology have a voltage rating of $V_{DC}/2$ and the other two switches have a voltage stress of V_{DC}. The control scheme is similar to the one described for the diode clamped topology, except that hysteresis current control is employed in the inner loop to track the reference current. A power factor of 0.999 and an efficiency of 89% have been reported by [24].

Capacitor Clamped Converter A flying capacitor is adopted in the capacitor clamped topology proposed in [25], as shown in Figure 2.4(c). All four switches in this circuit have a voltage rating of $V_{DC}/2$. The overall control scheme for this converter is identical to that presented in [24] for the switched clamped topology. Experimental results from a lab

prototype indicate an efficiency of 86% with close to unity power factor under at 1kW power level [25].

Other Multilevel Converters Figure 2.4(d) shows the novel single-phase three-level topology based on the half-bridge converter proposed in [26]. Similar to the switched clamped topology, two switches have a voltage rating of $V_{DC}/2$ while the other two switches are rated at V_{DC}. This topology uses double boost operation, meaning that the dc voltage produced is greater than twice the peak of the utility voltage. This poses limitation to the voltage level of the battery connected on the dc-side. The two-loop control approach can be applied to this converter. Based on the experimental results, a power factor of 0.994 can be achieved [26].

Other bidirectional three-level converters with higher number of switches as well as a bidirectional cascaded five-level converter are reviewed in [19].

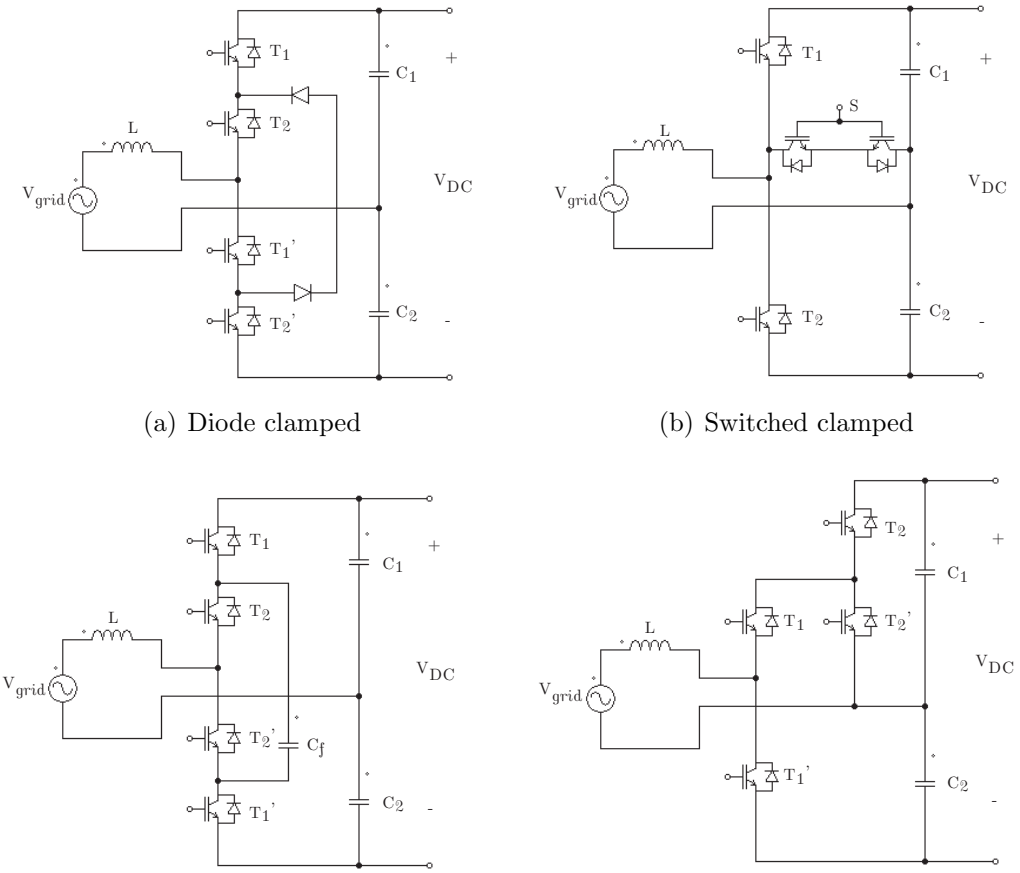

(a) Diode clamped

(b) Switched clamped

(c) Capacitor clamped

(d) 3-level

Figure 2.4: Multilevel AC-DC converters

Isolated AC-DC Converter

Galvanic isolation can be a desirable feature for a plugin vehicle charger due to safety reasons [27]. A single-stage isolated bidirectional charger is introduced in [28]. The proposed converter, illustrated in Figure 2.5, combines two active bridges with an intermediate high-frequency ac link and a series resonant tank. The high-frequency ac link increases power density and the presence of resonant tank results in soft-switching operation. The high frequency transformer provides isolation and voltage level scaling. The capacitor on the grid side acts as an input filter to suppress the current ripples at the switching frequency.

The control technique proposed in [28] uses a square wave modulation on the grid-side active bridge while the modulation signal for battery-side active bridge is phase-shifted by an angle varying between $-90°$ to $90°$ with respect to the first modulation signal to allow bidirectional power flow. Unity power factor can be achieved with this control scheme.

The battery-side dc current has high ripple contents at twice the line frequency. The magnitude of this ripple content is too high for the battery; thus, additional filtering on the battery side is necessary to reduce the ripples. This results in increase in overall volume and weight of the charger.

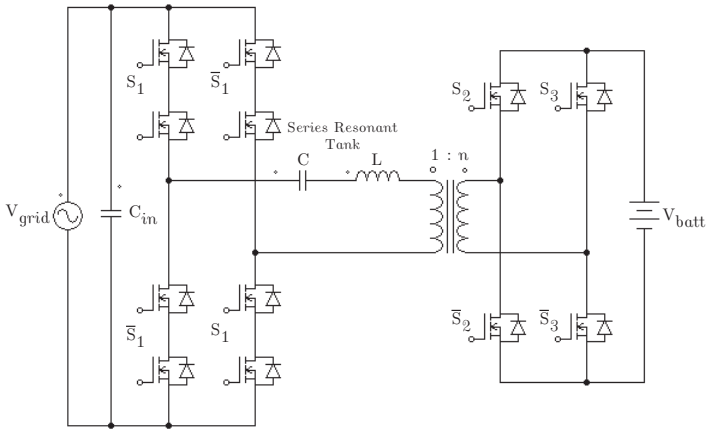

Figure 2.5: Single-stage isolated battery charger

2.2.2 Two-Stage Topologies

Most of the existing bidirectional plugin vehicle battery chargers reported in literature employ a two stages power conversion topology. Such configuration combines a bidirectional AC-DC converter with a bidirectional DC-DC converter. Figure 2.6 shows a simplified block diagram of this scheme. Two-stage topologies can generally support more than one charging level with improved performance in comparison to single-stage topologies. In this section, a review of the major contributions in this area will be presented.

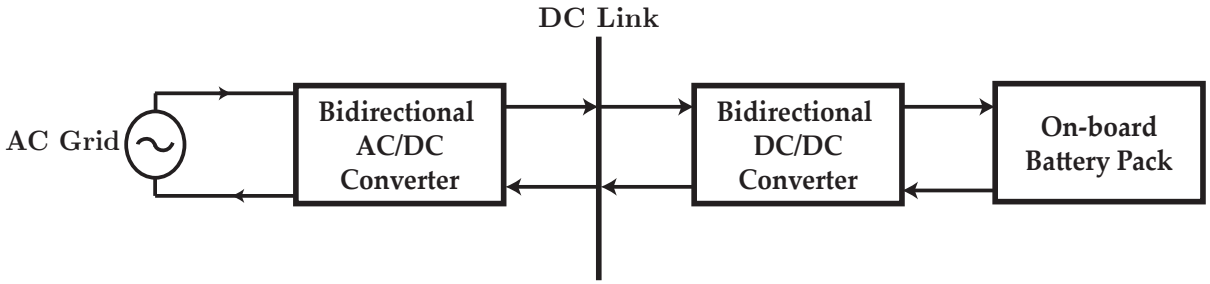

Figure 2.6: Two-stage charger configuration

Full-Bridge AC-DC and Two-Quadrant Buck-Boost

A single-phase full-bridge AC-DC converter combined with a two-quadrant buck-boost DC-DC converter (Figure 2.7) is a popular topology for the bidirectional on-board charger [13–15,29–31]. Extensive research has been performed to understand the characteristics of these converters, leading to many sophisticated control techniques have been developed [32–35], making this two-stage topology a favourable choice.

The AC-DC converter is responsible for ac-side current waveshaping, power factor correction and regulating the dc-link voltage, while the DC-DC converter controls the charging and discharging current of the battery through buck and boost operations. These chargers, even though relatively easy to design and implement, are challenged by the dc-link voltage ripple content at twice the grid frequency.

The control schemes discussed in [29, 30] are very similar. A rather slow outer loop is used to control the dc-link voltage and generate the amplitude of the ac-side current reference.

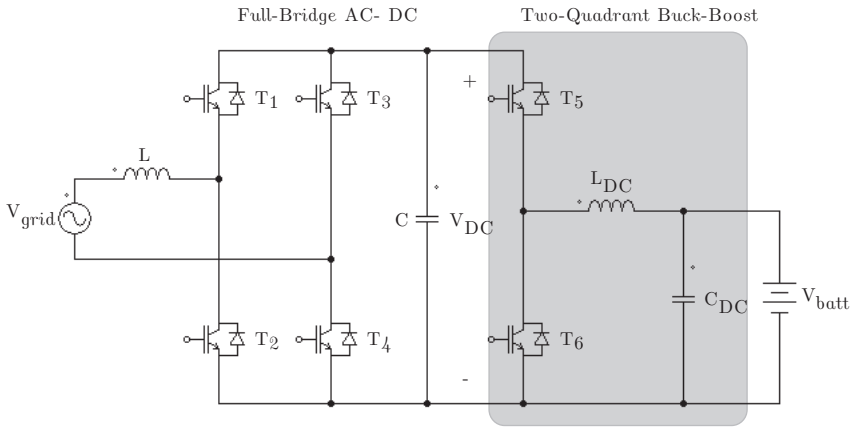

Figure 2.7: Two-stage charger: full-bridge AC-DC + two-quadrant buck-boost

Split-Phase Three-Leg AC-DC Converter and Two-Quadrant Buck-Boost

Figure 2.8 illustrates a two-stage charger designed specifically for an American household [36, 37]. A split-phase three-leg AC-DC converter is connected to the split-phase transformer at the main input panel on the grid-side and a two-quadrant buck-boost converter is used on the battery-side. Similar to the full-bridge converter, a harmonic component at twice the line frequency appears in the dc-link voltage.

The controller for the three-leg converter operates based on the same principle as the controller for the full-bridge converter. However, [36] proposes using a 2^{nd} order notch filer tuned at 120Hz in the voltage feedback loop to remove the low-frequency harmonics in the reference current. Moreover, a Proportional + Resonant (PR) controller is utilized in the current control loop for better tracking.

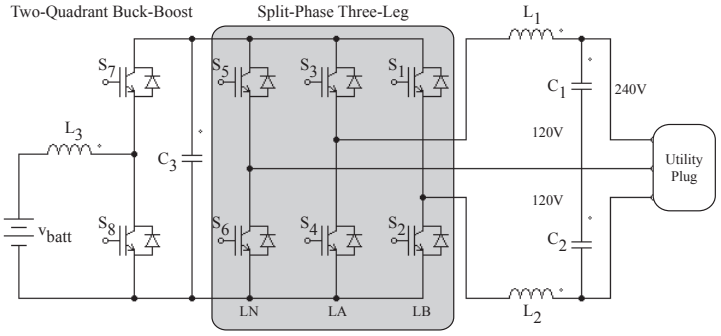

Figure 2.8: Two-stage charger: split-phase three-leg AC-DC + two-quadrant buck-boost

Full-Bridge AC-DC Converter and Dual Active Bridge DC-DC Converter

Conventional two-stage topologies connect the two converters via a high-voltage electrolytic capacitor to filter out dc-link voltage and to provide the necessary buffering. High-voltage electrolytic capacitors are not suitable for on-board chargers because of their bulkiness and their short lifetime. Newer charger designs aim to reduce the size of the dc-link capacitor through implementing novel control strategies [38]. The topology shown in Figure 2.9 incorporates two existing converter topologies: full-bridge AC-DC converter and a dual-active bridge (DAB) DC-DC converter. The DAB converter is chosen for its extra galvanic isolation for higher power applications.

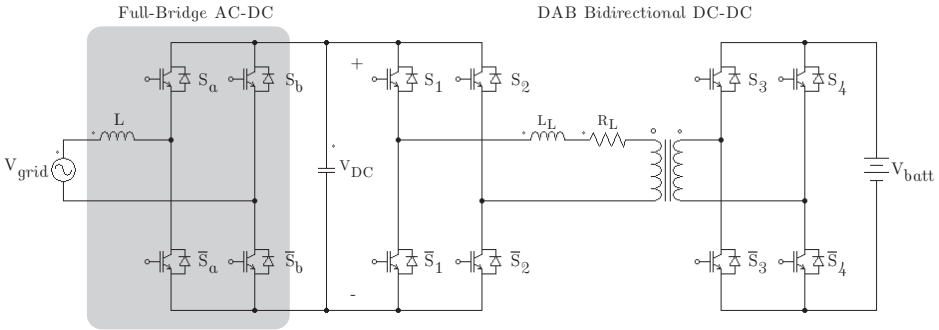

Figure 2.9: Two-stage charger: full-bridge AC-DC and DAB DC-DC

Commonly, the AC-DC converter regulates the dc voltage and provides power factor

correction, while the DC-DC converter controls the charging and discharging of the battery. Since the current reference is difficult to define in the DAB, novel control strategies propose that the roles of the controllers be switched. Consequently, the controller for the DAB is now responsible for regulating the dc-link voltage, whereas the controller of the full-bridge becomes a current regulator. This eliminates low-frequency ripple content in the dc link and considerably reduces the capacitor size. However, this advantage is achieved at the price of added cost and weight of the switches in the DAB.

2.2.3 Integrated Topologies

In classical plugin vehicle configurations, the inverter used for traction is separate from the battery charger. However, it can be observed in Figure 2.10 that both the battery charger and the traction require a bidirectional AC-DC converter, and since plugin vehicles cannot be driven and charged at the same time, it may be possible to satisfy these two functionalities by using only one AC-DC converter. Similarly, since the battery charger and the auxiliary power unit both require a DC-DC converter, it may be also worthwhile to combine these into one bidirectional DC-DC converter. With this vision in mind, integrated battery chargers aim to take advantage of the existing power electronics in a plugin vehicle to reduce the component count, and thus the volume, weight and cost. A review of the integrated topologies will be presented in this section.

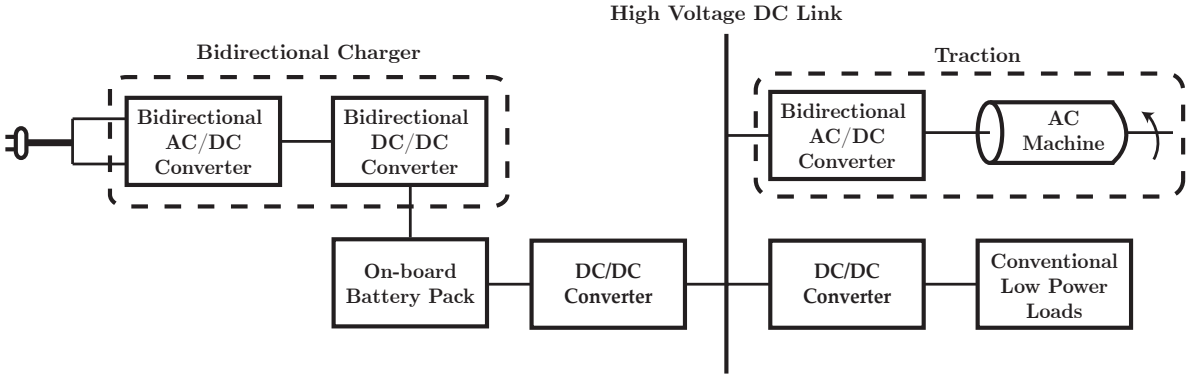

Figure 2.10: Classical plugin vehicle configuration

Integrated AC-DC and DC-DC Converter

The idea of integrating the battery charger with the high voltage (HV) bus of plugin vehicle was first proposed in [39] in 2009. The original design cascades a diode rectifier with a modified buck-boost converter. Much of the pioneer work was dedicated to the modified buck-boost converter design, which supports three modes of operation: plug-in charging, battery discharge to high-voltage dc bus and regenerative braking charging from the HV bus. However, the use of a diode rectifier prevents V2G power flow. A more comprehensive solution to support bidirectionality is presented in [40]. As shown in Figure 2.11, a three-level PWM AC-DC converter is adopted on the grid-side for its ability to achieve close-to-zero current harmonics and unity power factor. This integrated charger reduces the number of high-current inductors.

Current mode PWM control is adopted for controlling the charger. The details of operation are explained in [41]. The charger does not utilize any switching devices to configure the circuitry for different operating mode; therefore, careful coordination of the controllable switches is needed for the safe operation of this charger.

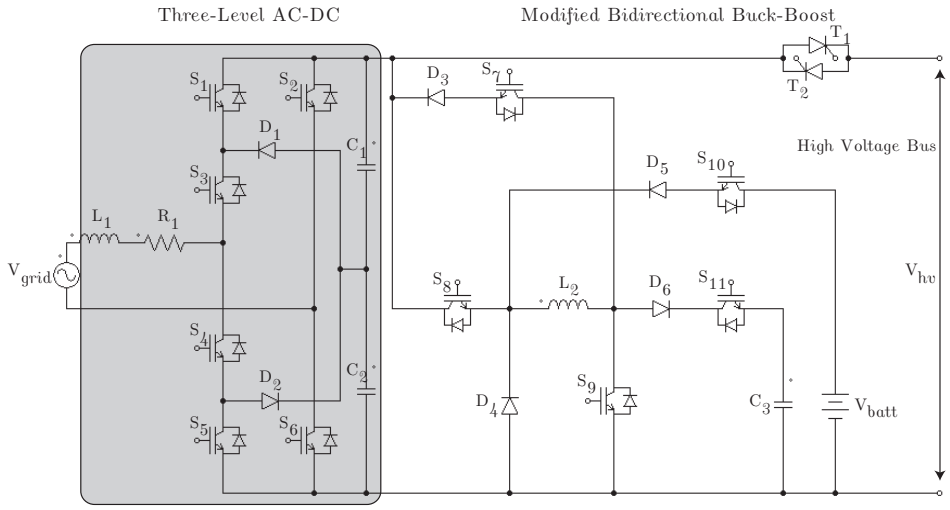

Figure 2.11: Integrated charger: three-level AC-DC + modified buck-boost DC-DC

Integrated Charger using AC Motor Windings

An integrated topology reported in [42] utilizes the AC motor windings in a plugin vehicle to realize the AC-DC part of the charger. The integrated topology is composed of three full-bridge PWM converters for grid-side connection and traction control, and a two quadrant buck-boost converter for dc-side management. Figure 2.12 shows the proposed integrated charger. It is possible to interface this integrated charger with both single-phase and three-phase utility grids. Most of the size reduction is realized through the use of the inductances in the motor windings for filtering purpose. This integrated charger can achieve unity power factor.

The proposed integrated charger is a non-isolated solution. Although the hardware and control implementation are relatively simple, this solution requires high number of switches.

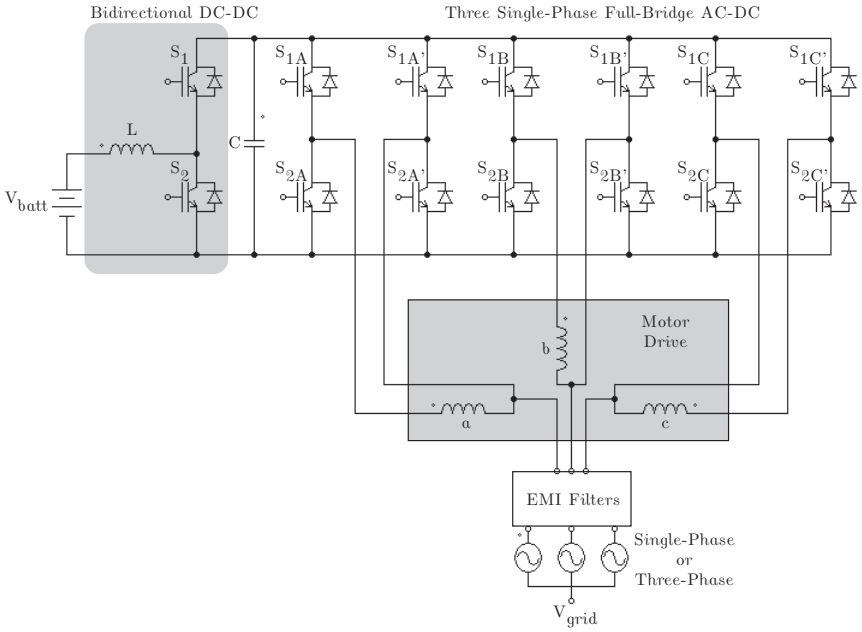

Figure 2.12: Integrated charger using AC motor windings

Integrated Charger Based on Permanent Magnet Synchronous Machine

Permanent-magnet synchronous motors (PMSM) are a favourable choice as a traction motor for electric vehicles owing to their high efficiency and ruggedness [43–45]. An integrated charger system including a PMSM is reported in [46]. Figure 2.13 displays a simple block diagram of the proposed system. This topology contains a three-phase full-bridge AC-DC converter and a bidirectional DC-DC converter. It supports five operating modes: (a) boost power transfer from battery to high voltage bus, (b) regenerative braking charging of battery, (c) plug-in charging of battery, (d) standalone inverter, and (e) power delivery from battery to grid.

This charger reduces the number of inductors and eliminates current transformers. However, the efficiency of the proposed charger is slightly lower than its unidirectional version due to extra conduction losses. Simulation results show that sinusoidal currents with unity power factor can be obtained at the unity grid interface in both directions of power flow.

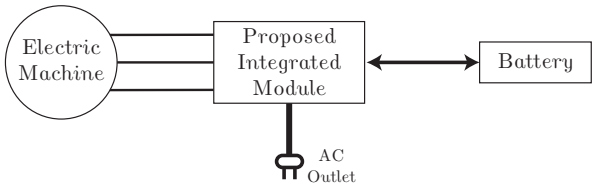

Figure 2.13: System diagram of proposed integrated charger based on PMSM

Integrated Charger Based on Induction Motor

An integrated charger based on an induction machine is reported in [47]. This integrated charger uses a novel Eight-Switch Inverter (ESI) and an interleaved DC-DC converter. Figure 2.14 illustrates this integrated charger. The ESI has four operating modes: (a) DC-AC converter, (b) three-phase PWM AC-DC rectifier for transferring power from induction motor to dc link, (c) single-phase PWM DC-AC inverter for delivering power from the battery back to the grid, and (d) single-phase DC-AC inverter for delivering power from the battery pack to the grid.

Four control strategies are analyzed with this integrated charger: (a) indirect field-oriented controller (IFOC) to decouple the torque and flux currents and effectively control

each current component independently, (b) indirect field-oriented control (IFOC) based on particle swarm optimization (PSO) to optimize the flux level in the induction motor, (c) dual-loop control for DC-DC converter, and (d) Proportional-Resonant control (PRC) for battery charging and discharging to the grid. Simulation results show that the integrated charger is capable of unity power factor operation.

The proposed integrated charger implements a complex controller. However, it fully utilizes the induction machine leakage inductances in the charger circuit. No switching devices, such as relays, are used to separate the circuitry in different operating modes.

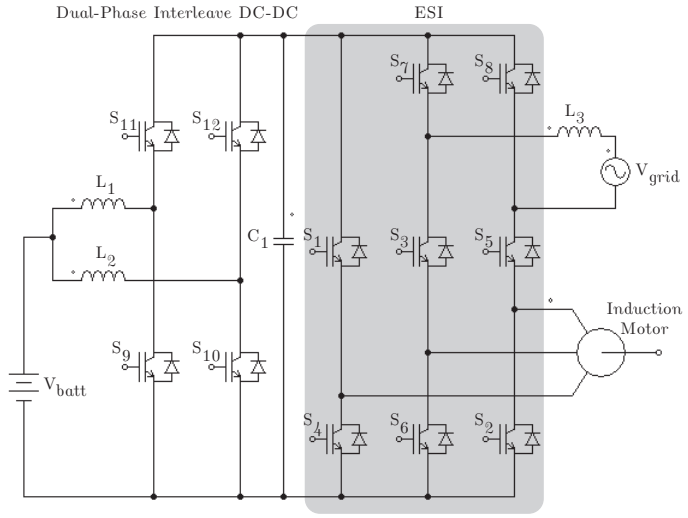

Figure 2.14: Integrated charger using a novel ESI AC-DC and a dual-phase interleaved DC-DC

Integrated Charger Based Different Winding Arrangements

Different motor configurations and winding arrangements can constitute novel integrated charger topologies. One isolated solution using an interior permanent magnet synchronous motor (IPMSM) was initially reported in [48]. The novel idea is to introduce a device called the motor/generator set, which acts as a motor in traction mode and as an isolated generator/transformer in charging mode. The practical implementation of the proposed integrated charger using a 6 pole, 1kW, split-phase permanent magnet synchronous motor (PMSM) is described in [49]. Due the motor windings, this charger is only suitable for

three-phase utility voltage. However, single-phase solution is possible depending on the machine type and winding configuration [50].

2.2.4 Summary

An on-board bidirectional battery charger is an important component for plugin vehicles when supporting V2G is intended. In summary, battery chargers are generally classified under two main categories: single-stage and two-stage. Single-stage topologies are simple, but are limited to level 1 charging. Two-stage topologies are more suitable for high-voltage charging and achieve better performance with a tradeoff in size and weight. Integrated topologies are a special type of two-stage topologies, which aim to reduce component count by taking existing power electronics in motor drives and electric machine windings in the plugin vehicle for constructing the charging system.

Chapter 3

Design Criteria and Battery Model

3.1 Design Criteria

The proposed bidirectional battery charger will be designed to meet all the design criteria outlined in this chapter. The criteria were drafted to improve the user experience for plugin vehicle consumers, to enhance the performance of plugin vehicles, and to satisfy V2G power transactions.

1) On-board configuration

The bidirectional battery charger under study is meant for on-board applications. On-board charger offers more flexibility in terms of charging locations, since the vehicle owner is not restricted to charge the battery pack at charging stations only. Many regions and/or countries currently do not have established charging station networks. As a result, having an on-board charger for plugin vehicles is a more favourable solution as it allows household charging. However, with on-board chargers, the size and weight should be minimized. Larger size and greater weight cause detrimental effect on the fuel efficiency and driving range of the plugin vehicle. One of the objectives of the novel design is to employ an on-board charger configuration, while keeping size and weight at a minimum.

2) Level 2 charging

The novel battery charger is to be designed for level 2 charging. Even though consumers are able to recharge their plugin vehicles at their households using an on-board charger configuration, the consumers should also be able to fully recharge the battery packs from zero charge overnight and be able to drive their vehicles in the morning. Due to the lengthy charging time associated with level 1 charging, this level of charging is not suitable for charging a battery pack intended for overnight charging and being ready for daily commute. On the other hand, although DC charging provides a solution for fast charging, its charging power level is too high for safe operation in a household. Even if DC charging is safe in a residential environment, expensive infrastructure upgrade is needed for household adoption. In compromising the advantages and shortfalls of level 1 and DC charging, a charger with level 2 charging capability provides the most suitable alternative. Level 2 charging is capable of refueling an empty battery pack in 4-8 hours, which is acceptable for overnight charging. In addition, adopting level 2 charging in a household requires less equipment upgrades than that of DC charging and the upgrade expenses fall in an affordable range for a general household.

3) Two-stage topology structure

The intended battery charger has a two-stage topology. Although single-stage topologies feature smaller size and weight, their inadequacy to support level 2 or DC charging poses a limitation. This makes the two-stage topologies the better option. Although integrated topologies are categorized under two-stage topologies, they are not considered here. Integrated topologies are highly dependent on the vehicle drivetrain configuration and the electric motor type, and are generally designed exclusively for a particular vehicle model. This design restriction violates the objective of an all-platform bidirectional battery charger.

4) 300V battery pack

The battery charger is designed for a plugin vehicle that carries a battery pack with a nominal voltage of 300V. This nominal voltage is selected based on observing different popular PHEVs and EVs currently in the market. Table 3.1 shows the battery pack's

nominal voltages and total capacities for Nissan Leaf, Chevrolet Volt and Toyota Prius Plug-In Hybrid. The nominal voltage and capacitor of the battery pack under consideration is taken to be equal to those of Chevrolet Volt, i.e. 300V and 16kWh, respectively.

Table 3.1: Battery pack characteristic of selected electric vehicles

Vehicle	**Battery Type**	**Nominal Voltage (V)**	**Capacity (kWh)**
Nissan Leaf [51]	Laminated lithium-ion	360	24
Chevrolet Volt [52]	Lithium-ion	300	16
Toyoto Prius Plug-In Hybrid [53]	Lithium-ion	207.2	4.4

5) Power factor control capability

The battery charger must be able to send power back to the grid with unity power factor as required by IEEE Standard 1547 - IEEE Standard for Interconnecting Distributed Resources with Electric Power Systems [54]. In addition, the charger should also have the capability to realize reactive power compensation as this is one of the most attractive benefits of V2G. In order to satisfy these two requirements, the controller of the battery charger should be able to control the desired power factor at the interface of the charger with the utility grid.

3.2 Design Process Overview

The design of the bidirectional battery charger will begin with developing a battery model that can form a good representation of the transient and steady-state characteristics applicable to most popular plugin vehicle battery chemistries. A well-developed battery model is a critical milestone in the design process because it not only provides dynamics characteristics of the battery pack, but also provides feedback on the performance of the battery charger. This feedback can be used to evaluate the efficiency of the charger as well as the power quality at its interface with the grid. Although the battery model's ability to accurately predict the behaviour of the battery is an important asset, the battery model should also be simulation-friendly. Most of the initial development of the battery charger

will be done in a simulation environment; therefore, the model should be easily adapted to a variety of power electronic simulation programs.

The design of battery charger will be split into two stages. First, the AC-DC converter on the grid-side will be developed. This will include choosing an appropriate topology along with developing appropriate an control technique for the selected topology. Second, the DC-DC converter on the battery-side will be designed. Similar to the previous design stage, some bidirectional DC-DC converter topologies will be examined, and one or more topologies that are most suitable options for this application will be identified. Control technique for the DC-DC converter will also be investigated. Once the initial design work for the two stages is completed, they will be combined to validate their functionalities as a single unit in simulation.

If the designed battery charger satisfies all the specifications and simulation results reveal acceptable performance, the final step is to implement a lab prototype of the charger for proof of concept as well as to verify the performance of the charger.

3.3 Battery Types

A sophisticated energy storage system is essential for a plugin vehicle. It plays a significant role in the vehicle's driving range and price. When evaluating energy storage systems for automotive applications, there are several performance metrics that need to be considered: storage capacity, charge/discharge rate, specific energy and power, operating voltage, self-discharge rate, cycle life, state-of-charge and state-of-health [16]. Capacity refers to the amount of charge a battery can store. Charge/discharge rate is the power acceptance/delivery capability of a battery. Specific energy and power are the battery's capacity and discharge rate divided by the per unit mass, respectively. A higher value means better performance per unit kilogram. Self-discharge rate refers the rate of capacity loss when the battery is idle. Cycle life is the number of times the battery can be charged and depleted. State-of-charge (SOC) denotes the amount of charge remaining in the battery, usually given as a percentage of the total capacity. Lastly, state-of-health is the present storage capacity as a percentage of the capacity at the beginning of life. This is strongly affected by aging and the manner in which the battery is operated in an application.

There are three types of energy storage systems that are commonly used in plug-in hybrid electric vehicles and all-electric vehicles; they are lead-acid batteries, nickel-metal

hydride batteries (NiMH) and lithium-ion (Li-ion)batteries. An overview of performance and estimated cost of each chemistry is provided in Table 3.2 [55]. In this section, the characteristics of each of the three battery chemistries will be briefly described and their suitability for use in plugin vehicles will be discussed.

Table 3.2: Performance and cost overview of different battery chemistries [55]

Battery Chemistry	**Specific Energy [Wh/kg]**	**Specific Power [W/kg]**	**Cell Voltage** [V]	**Self-discharge [%/Month]**	**Cycle Life [@80% DoD*]**	**Cost Estimation**	
						[$/kWh]	**[$/kW]**
Lead-Acid	20-40	300	2.1	4-8	200	150	10
NiMH	40-60	500-1300	1.2	20	>2500	500	20
Li-ion	100-200	800-3000	3.6	1-5	<2500	800	50-75

*DoD (Depth-of-Discharge) is the SOC level to which the battery is discharged.

3.3.1 Lead-Acid Batteries

Lead-acid batteries are the oldest type of rechargeable battery and are currently used in all internal combustion engine vehicles for ancillary loads. They are a type of wet cell battery and usually contain a mild solution of sulfuric acid in an open container [56]. The name, lead-acid, originates from using lead electrodes and acid electrolyte to generate electricity.

Due to their mature technology, high availability and low cost, lead-acid batteries have dominated the automotive industry in the past few decades. However, plugin vehicles demand a much larger energy storage system than conventional vehicles, but the low energy density found in lead-acid batteries would result in a heavy and bulky battery pack. Therefore, lead-acid batteries are not an ideal choice for use in plugin vehicle energy storage systems. Furthermore, lead-acid batteries produce dangerous gases while being used and a risk of explosion when overcharged; this poses a safety hazard for the consumers. Therefore, newer models of plugin vehicles have stopped using lead-acid batteries in their form of energy storage systems.

3.3.2 Nickel Metal Hydride Batteries

Nickel-metal hydride (NiMH) batteries have a much longer life cycle than lead-acid batteries, with a reasonable specific energy, and contain no toxic metals. These combined positive characteristics had made them widely use in hybrid electric vehicles.

Nonetheless, NiMH batteries are challenged by their high cost, high self-discharge rate and the need to control hydrogen loss [57]. Owing to the nature of chemistry, it is unlikely that there will be any great increase in specific energy or power with future research. Consequently, NiMH batteries appear not to be the perfect candidate for use in plugin vehicles where high energy storage capacity is necessary.

3.3.3 Lithium-Ion Batteries

Lithium-ion (Li-ion) batteries are widely considered as the best candidate for energy storage systems in plugin vehicles. These batteries have high specific energy, high specific power, high energy efficiency and low self-discharge [57], making them a great promise in use for plugin vehicles.

The theory behind Li-ion batteries is simple; during discharge, lithium ions in the battery cell move from the negative electrodes to the positive electrodes, and these ions travel in the reverse direction when charging. Many variations of Li-ion batteries are available, such as lithium-ion polymer, lithium vanadium oxide, lithium iron phosphate, and Nanophosphate, which is proprietary to A123 Systems [58].

The most common charging method for Li-ion batteries is the constant-current constant voltage (CC-CV) charging scheme. The battery cells are first charged in CC scheme where a constant charging current is applied to the cells until a rated terminal voltage per cell is reached. Then a CV charging scheme is adopted by applying a manufacturer rated cell voltage multiplied by the number of series cells across the terminals. The charging procedure halts when the current reaches to a very small value, indicating 100% SOC.

Regardless of the many technologies found in Li-ion batteries, there are several challenges that these batteries are facing in automotive applications. Li-ion batteries are expensive in comparison with other types of batteries. They have shorter life span compared to NiMH batteries owing to their lower number of life cycles in their life time. This is the reason why research has been ongoing in attempt to reduce the cost and extend

their useful life. There are also safety concerns when using Li-ion batteries since they can experience thermal runaway without proper control schemes. An aggressive thermal management system is required to keep this risk to a minimum.

3.4 Battery Model

It is important when simulating the battery charger to have a battery model to represent the non-linear behaviour of the battery chemistry. For this reason, it is wise to choose a battery model that is friendly to simulate with other electrical circuits and systems, but also provides sufficient behavioural information about the battery. Consequently, the electrical circuit model has been chosen as the battery model to be used for all three vehicular battery chemistries (lead-acid, NiMH and Li-ion) due to its ability to provide a good balance of complexity and accuracy for power electronic designs.

Figure 3.1 shows the equivalent electrical circuit battery model. It is a modified version based of the model proposed in [59]. The main differences are in that the modified model disregards the battery self-discharge rate and also directly relates thate open-circuit voltage (V_{OC}) to the %SOC using coulomb counting through the current feedback, which are important in understanding the characteristic of a battery. However, both the equivalent electrical circuit battery model and the model proposed in [59] are capable of capturing the I-V characteristics of the battery cells.

The electrical network in the modified battery model, which consists of a series resistor and two parallel RC networks, is responsible for the transient response of the battery cell. The series resistor, R_{series}, characterizes the instantaneous voltage drop in the step response. The two RC networks, i.e., $R_{transient_S}$ - $C_{transient_S}$ and $R_{transient_L}$ - $C_{transient_L}$ represent the short and long time constants of the step response respectively. Lastly, I_{batt} refers to the battery terminal current, which is taken to be positive for discharging and negative for charging.

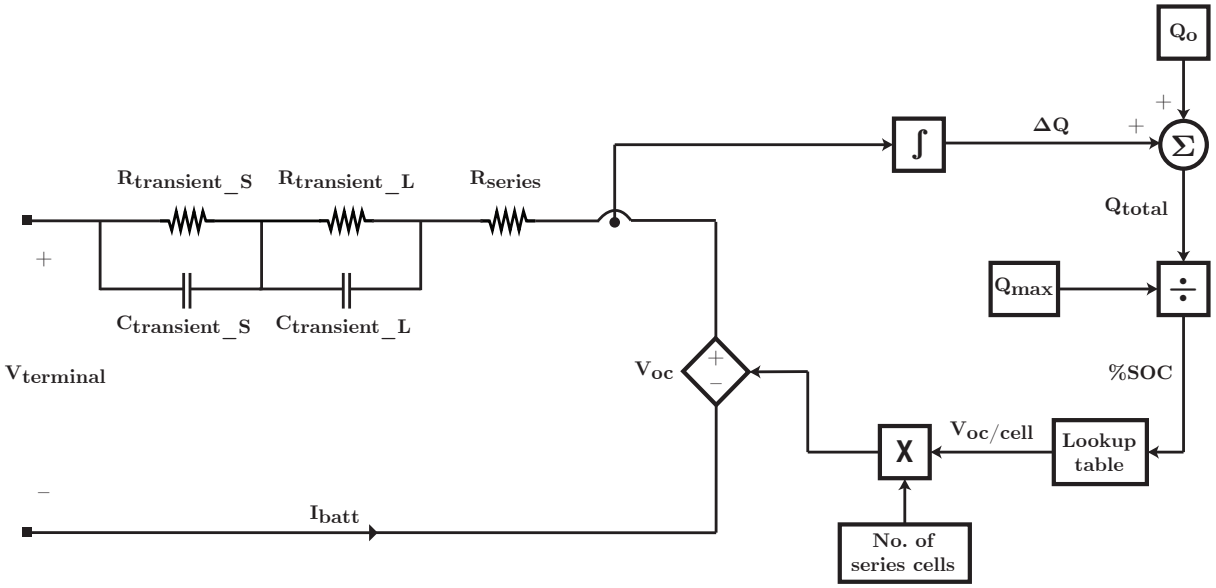

Figure 3.1: Equivalent electrical circuit battery model

The remaining part of the model calculates the V_{OC} of the battery cell or pack based on the %SOC at any instance of time. The battery current is measured and integrated to find the change in electric charge in coulombs. This change in electric charge is added to the initial charge, which is equivalent to the final charge value from previous use, to obtain the present amount of electric charge in the battery. This value is then divided by the maximum amount of charge that the battery can store to get the battery %SOC. The lookup table converts the %SOC to the V_{OC} of a single battery cell based on the charging/discharge current for the battery as well as based on the assumption that battery cells are balanced from %SOC point of view. The V_{OC} per cell is multiplied by the number cells in series in order to get the overall V_{OC}.

3.4.1 Model Parameters

Model parameters, i.e., R_{series} and resistances and capacitances of the two RC networks, are all functions of SOC. These functions can be extracted experimentally. The purpose of such experiment is to collect datapoints of terminal voltage at various %SOC levels

in order to extract a single-variable function for each model parameter. The theoretical concepts behind battery model extraction and the role of each parameter will be explained in this section. This explanation assumes that the battery temperature is controlled and maintained at a certain value by the battery management system. The actual experiment procedures are described in Appendix A.

Transient Response Parameters

Series resistor, R_{series}, is responsible for the instantaneous rise or drop of the terminal voltage in the step response. When a battery begins to recover from being discharged, it would experience an instantaneous voltage rise. On the contrary, when the battery begins to recover from being charged, it would experience an instantaneous voltage drop. R_{series} at a particular %SOC level can be calculated using equation (3.1). Variable V_0 is the initial terminal voltage before the battery undergoes any interruption. Variable V_1 is the terminal voltage after the instantaneous rise or drop of terminal voltage and I_{batt} is the charging/discharging current measured at the battery terminal.

$$R_{series} = \frac{|V_1 - V_0|}{|I_{batt}|} \tag{3.1}$$

The behaviour of the two RC network is characterized by the battery terminal voltage when the battery is recovering from an interruption. The typical transient responses of a battery during charging and discharging are shown in Figure 3.2. The recovery periods are enclosed by the double head arrows. During this period the battery should be undisturbed so that it can recover its unavailable capacity. While the battery is recovering from being discharged, the battery terminal voltage would rise exponentially, similar to a charging capacitor, and its behavior is defined by equation (3.2a) [60]. In the case where the battery is recovering from being charged, its voltage profile is similar to that of a discharging capacitor and this decaying behaviour is described by equation (3.2b) [60].

$$V_{terminal} = \begin{cases} a \cdot (1 - \exp^{-b \cdot t}) + c \cdot (1 - \exp^{-d \cdot t}) + e & \text{, discharging} \quad (3.2a) \\ a \cdot (\exp^{-b \cdot t}) + c \cdot (\exp^{-d \cdot t}) + e & \text{, charging} \quad (3.2b) \end{cases}$$

In equations 3.2a) and (3.2b), variable e is the battery terminal voltage at the beginning of the resting phase after the instantaneous rise or drop of voltage, which is labeled as

V_1 in Figure 3.2. Variables b and d represent the short- and long-term time constants, respectively. These variables, along with variables a and c are determined from least-square curve fitting. Variable I is the charging or discharging current measured at the battery cell's terminal. The procedures for curve fitting are outlined in Appendix A. At a given %SOC, R_{series} and the RC networks' resistances and capacitances can be derived using equations (3.3)-(3.6) with the curve fitting variables.

$$R_{transient_S} = \frac{a}{I} \tag{3.3}$$

$$C_{transient_S} = \frac{1}{R_{transient_S} \cdot b} \tag{3.4}$$

$$R_{transient_L} = \frac{c}{I} \tag{3.5}$$

$$C_{transient_L} = \frac{1}{R_{transient_L} \cdot d} \tag{3.6}$$

Once there are enough known values collected for the transient parameters at various % SOC levels, their single-variable functions can be generated. These functions are of the form shown in equations (3.7)-(3.11).

$$R_{series}[SOC] = a_0 \cdot exp(-a_1 \cdot SOC) + a_2 \tag{3.7}$$

$$R_{transient_S}[SOC] = b_0 \cdot exp(-b_1 \cdot SOC) + b_2 \tag{3.8}$$

$$C_{transient_S}[SOC] = c_0 \cdot exp(-c_1 \cdot SOC) + c_2 \tag{3.9}$$

$$R_{transient_L}[SOC] = d_0 \cdot exp(-d_1 \cdot SOC) + d_2 \tag{3.10}$$

$$C_{transient_L}[SOC] = e_0 \cdot exp(-e_1 \cdot SOC) + e_2 \tag{3.11}$$

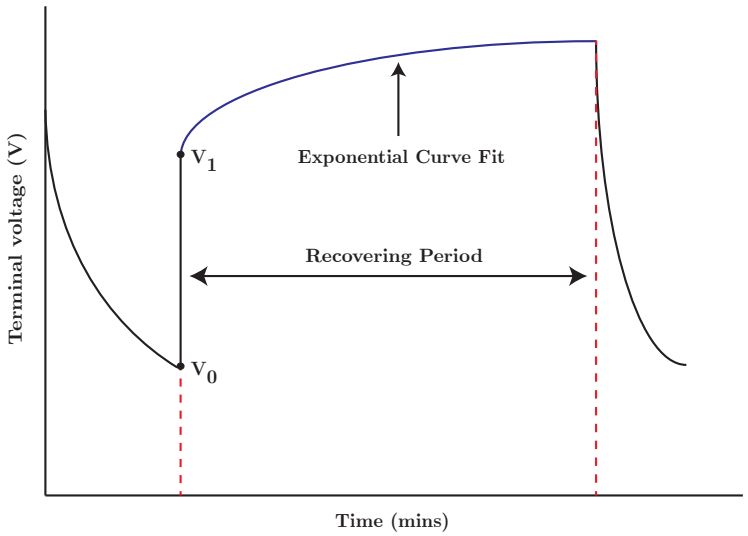

(a) Discharging

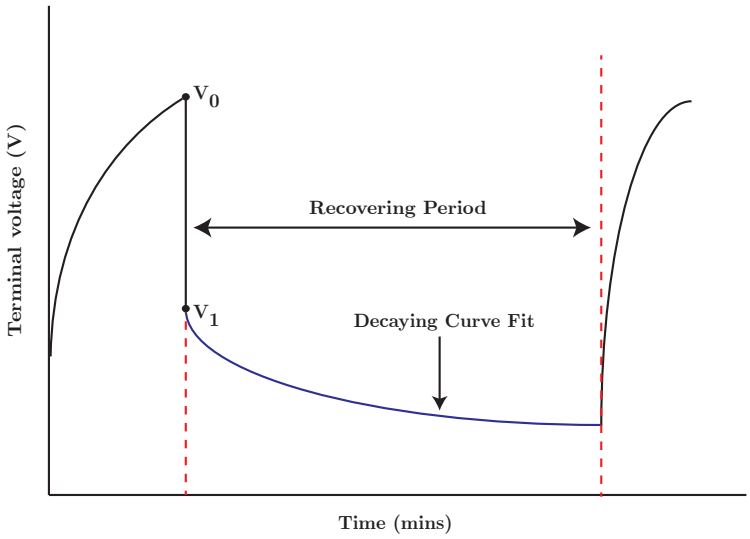

(b) Charging

Figure 3.2: Typical battery terminal voltage transient responses

Open Circuit Voltage

The open circuit voltage (V_{OC}) of the battery as a function of %SOC is also important in understanding the behaviour of a battery. It is expected that the V_{OC} of a battery cell would be different during charging and discharging at a specific current level and %SOC, complicating the use of the battery model.

A rapid and simple method to determine V_{OC} takes advantage of terminal voltage variations after an instantaneous rise or drop. At a certain %SOC and current level, there exist two values of V_1 theoretically: one for charging and one for discharging. Therefore, with sufficient number of V_1 values collected at various %SOC levels for both cases, there would be two curves that form the boundaries of the V_{OC} region, as illustrated by the dashed lines in Figure 3.3. The solid line in Figure 3.3 represents the average of V_{OC} region and is known as the V_{OC} curve.

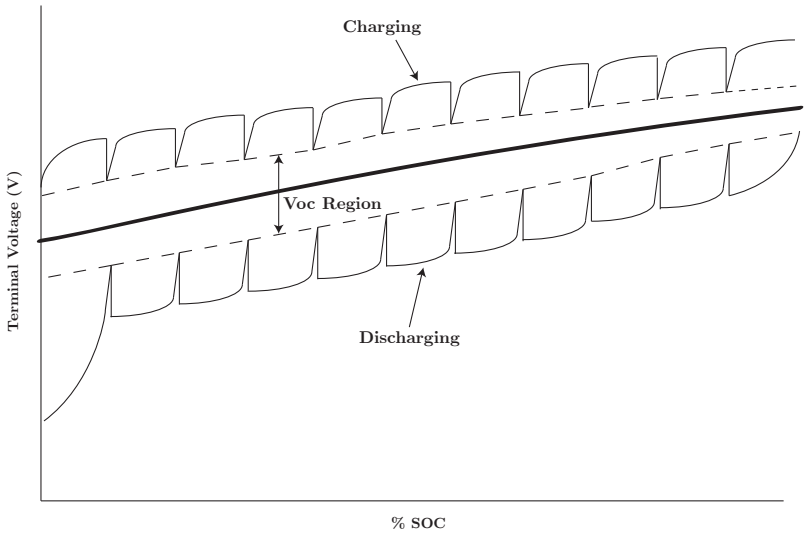

Figure 3.3: Terminal voltage vs. %SOC during charging and discharging

Another method to determine V_{OC} is to utilize the steady-state terminal voltage of the battery. The effects of the two RC transient networks and the series resistor diminish after

the battery has sufficient time to recover. As a result, the V_{OC} of the battery becomes equivalent to the steady-state terminal voltage at a specific %SOC.

3.4.2 Equation-Based Battery Model for Simulation

The initial design of the bidirectional battery charger will be done in simulation using the simulation tool PSIM. Because passive elements in PSIM cannot be simulated as a function of some variable, the representation of the battery model's parameters will need to be slightly modified before simulating in PSIM. As a result, the resistors will be realized as non-linear elements with a voltage drop based on the passing current and the resistance, where the resistance is a function of %SOC. The representation of each capacitance will be done in two parts. First, the constant terms in $C_{transient_S}$ and $C_{transient_L}$ will be realized using a capacitance element in PSIM. Second, the SOC-depended part will be realized based on the relation $i_C = C(dv/dt)$. These two parts will be paralleled in order to sum up the capacitances. This modified battery model for simulation purposes is known as the equation-based equivalent battery model. The construction of the equation- based battery model is shown in Figure 3.4.

The single-variable functions for the model parameters and V_{OC} (equations (3.12)-(3.17)) used in Figure 3.4 are taken from [59]. These functions will be used in the design process to represent one individual polymer Li-ion battery cell with an 850mAh capacity and an assumed nominal voltage of 3.3V. Also, these functions have an operating from 0.5% to 90% SOC.

$$V_{OC}(SOC) = -1.031 \cdot e^{-35 \cdot SOC} + 3.685 + 0.2156 \cdot SOC - 0.1178 \cdot SOC^2 + 0.3201 \cdot SOC^3 \tag{3.12}$$

$$R_{series}(SOC) = 0.1563 \cdot e^{-24.37 \cdot SOC} + 0.07446 \tag{3.13}$$

$$R_{transient_S}(SOC) = 0.3208 \cdot e^{-29.14 \cdot SOC} + 0.04669 \tag{3.14}$$

$$C_{transient_S}(SOC) = -752.9 \cdot e^{-13.51 \cdot SOC} + 703.6 \tag{3.15}$$

$$R_{transient_L}(SOC) = 6.603 \cdot e^{-155.2 \cdot SOC} + 0.04984 \tag{3.16}$$

$$C_{transient_L}(SOC) = -6056 \cdot e^{-27.12 \cdot SOC} + 4475 \tag{3.17}$$

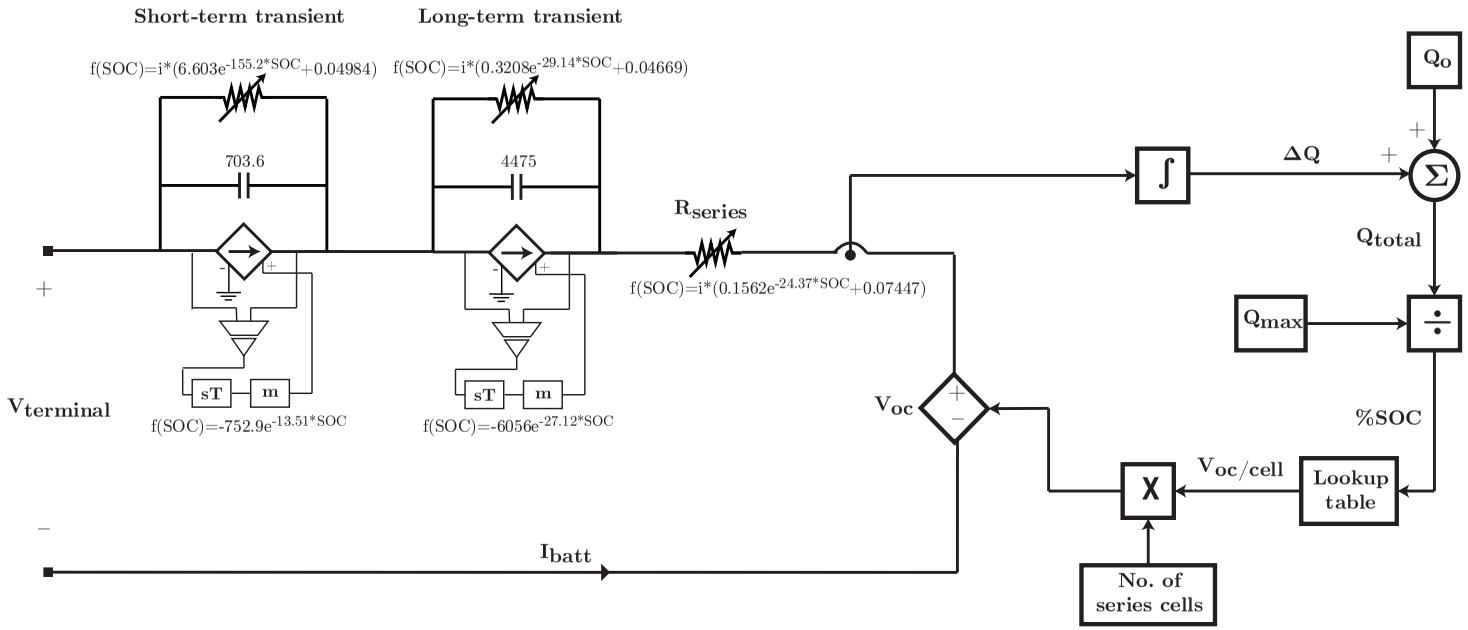

Figure 3.4: Equation-based electrical circuit battery model

3.4.3 Forming a Battery Pack

The battery pack in a plugin vehicle is made up of hundreds of individual battery cells connected together in both series and parallel configurations. The number of series cells determines the terminal voltage of the battery pack, whereas, the number of series cells connected in parallel branches defines the capacity of the battery pack.

With the high number of individual battery cells contained in each battery pack and the number of parameters defining the components of each cell, it will be memory-expensive and time-consuming to simulate each and every parameter in a battery pack. Therefore, it is of interest to use only one resistor and two RC networks to represent the behaviour of a battery pack by finding the equivalent impedance of each model parameter based on the cell configuration of the battery pack. Since determining the equivalent resistance for identical resistors connected in series and parallel is straightforward, the focus here will be deriving equivalent impedance for parallel RC networks.

Equivalent Series RC Networks Impedance

Suppose there is a string of n parallel RC networks connected in series, each with a resistance R and a capacitance C, as shown in Figure 3.5. The equivalent impedance for series-connected RC networks can be deducted by first calculating the equivalent impedance of one RC network.

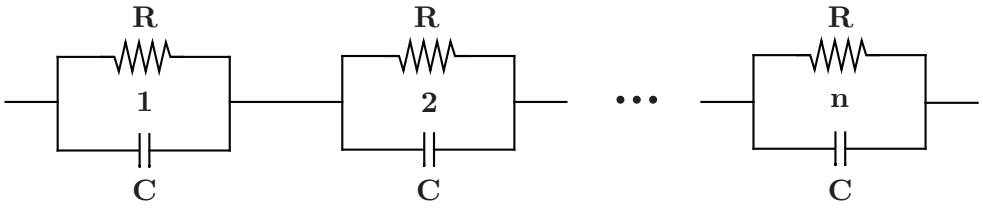

Figure 3.5: A string of series RC networks

Using Laplace Transform, the equivalent impedance of one RC network is,

$$Z_{eq_{s1}} = \frac{R \cdot \frac{1}{sC}}{R + \frac{1}{sC}} = \frac{R}{sCR + 1} \tag{3.18}$$

Following that, the equivalent impedance of two identical RC networks connected in series is,

$$Z_{eq_{s2}} = \frac{2R}{sCR+1} \tag{3.19}$$

Therefore, by induction, the equivalent impedance of n RC networks can be derived as,

$$Z_{eq_{sn}} = \frac{nR}{sCR+1} \tag{3.20}$$

The goal is to use a single RC network to realize all n series-connected RC networks. This can be achieved by comparing both sides of equation (3.21), where the left side of the equation is the equivalent impedance of n series-connected RC networks, and the right side of the equation represents the impedance of the RC network representing the n identical RC networks connected in series.

$$\frac{nR}{sCR+1} = \frac{R_t}{sC_tR_t+1} \tag{3.21}$$

It can be seen from equation (3.21) that the single RC network has a resistance value equals to n times that of the individual resistors and a capacitance value equal to that of the individual capacitors divided by n, as illustrated by equations (3.28) and (3.23).

$$R_t = nR \tag{3.22}$$

$$C_t = \frac{C}{n} \tag{3.23}$$

Equivalent Parallel RC Networks Impedance

By applying a similar induction-based proof procedure, the equivalent impedance of paralleled RC networks can also be derived. Suppose that there are m identical RC networks connected in parallel, as shown in Figure 3.6, and as in the previous case, each RC network has a resistance value of R and a capacitance value of C.

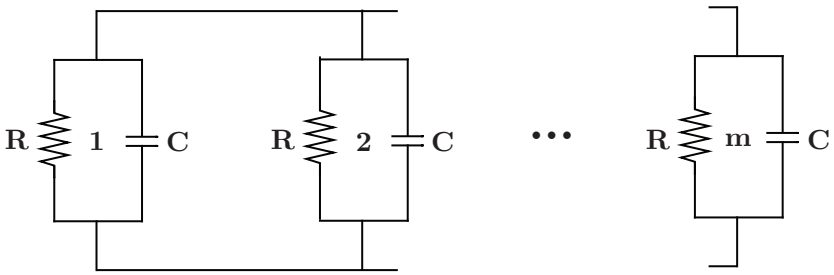

Figure 3.6: A string of parallel RC networks

The equivalent impedance of one RC network is the same as calculated in equation (3.18). However, when two RC networks are connected in parallel, the overall impedance becomes,

$$Z_{eq_{p2}} = \frac{R}{sCR+1} || \frac{R}{sCR+1} = \frac{R}{2(sCR+1)} \tag{3.24}$$

By induction, the overall impedance of m RC networks connected in parallel is shown in equation (3.25).

$$Z_{eq_{pm}} = \frac{R}{m(sCR+1)} \tag{3.25}$$

Following a similar derivation procedure, the left side of equation (3.26) represents the impedance of m parallel RC networks and the right side of equation (3.26) is the impedance of one single RC network representing m parallel RC networks.

$$\frac{R}{m(sCR+1)} = \frac{R_t}{sC_tR_t+1} \tag{3.26}$$

By comparing both sides of equation (3.26), one can observe that the resistance and capacitance of the single RC network are equivalent to having m identical resistors and m identical capacitors connected in parallel, as illustrated by equations (3.27) and (3.28).

$$R_t = \frac{R}{m} \tag{3.27}$$

$$C_t = mC \tag{3.28}$$

Equivalent Impedance of a Battery Pack

Suppose the battery pack contains n x m battery cells, then there are n x m of identical RC networks connected in a configuration like the one shown in Figure 3.7.

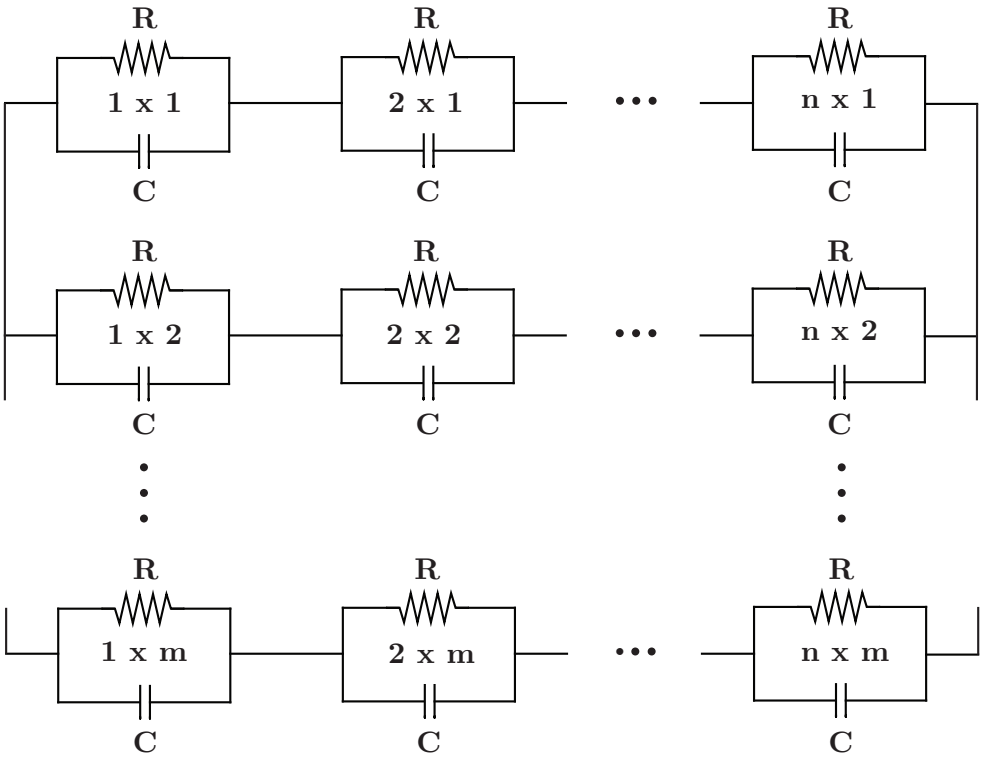

Figure 3.7: Parallel RC networks in nxm configuration

Using the equivalent impedances derived for series and parallel connections, a single RC network representing the n x m RC networks of Figure 3.7 has an equivalent impedance givenby equation (3.29).

$$Z_{eq_{nxm}} = \frac{nR}{m(sCR+1)} \tag{3.29}$$

Consequently, the resultant RC network for realizing n x m identical RC networks has resistance and capacitance of values that can be calculated using equations (3.30)

and (3.31).

$$R_t = \frac{nR}{m} \tag{3.30}$$

$$C_t = \frac{mC}{n} \tag{3.31}$$

The equivalent impedance of the series resistance in the battery model can be taken as an RC network with $C = 0$. As a result, if there are n x m identical resistance in a battery pack, as shown in Figure 3.8, the equivalent impedance is equal to equation (3.30).

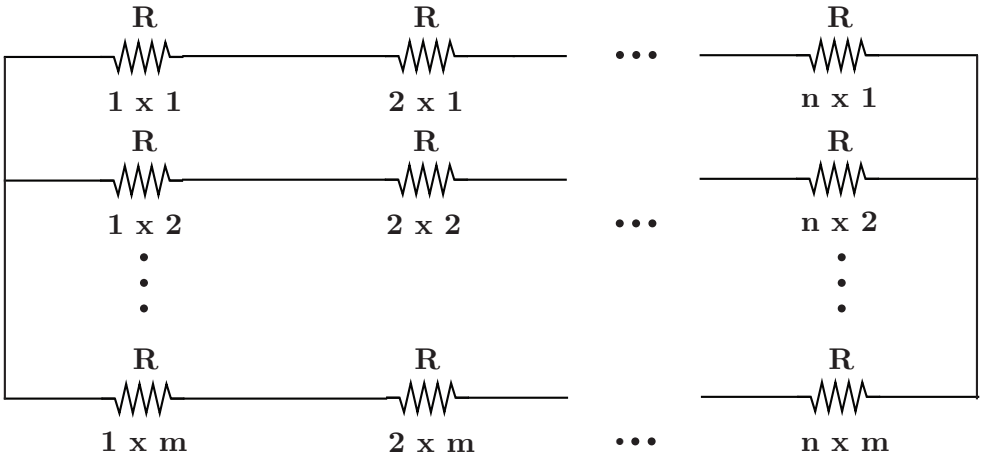

Figure 3.8: Series resistance in n x m configuration

Lastly, the equivalent open circuit voltage of a battery pack can also be derived. Suppose there are n x m individual battery cells with an open circuit voltage equivalent to V_{oc} connected in the battery pack configuration shown in Figure 3.9. It can be observed that the voltage at each parallel branch is identical. This implies that the equivalent open circuit voltage of battery pack is equivalent to the number of battery cells connected in series multiplied by the open circuit voltage of an individual battery cell, as described by equation (3.32).

$$V_{oc_{eq}} = nV_{oc} \tag{3.32}$$

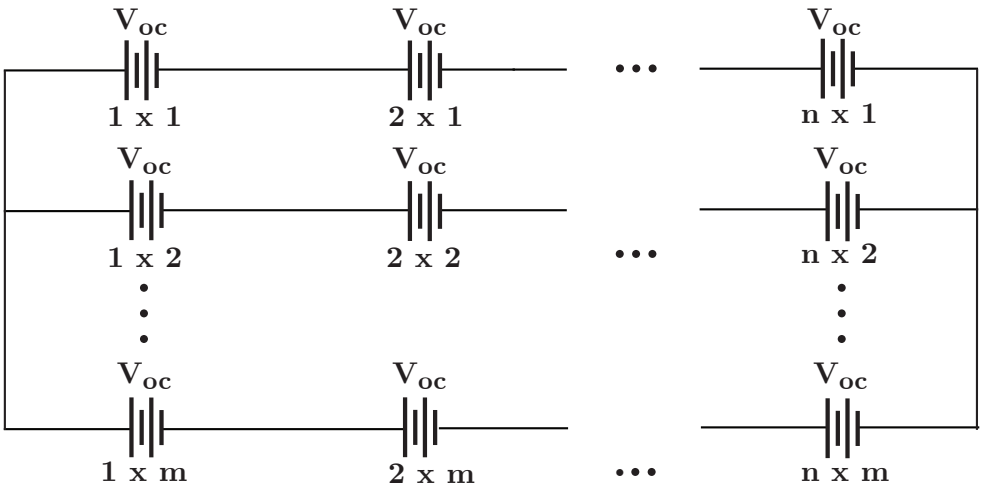

Figure 3.9: Open circuit voltage in n x m conifguration

Up to this point, the equivalent impedance of each parameter in a battery pack has been derived individually. To generalize how they can be combined to form the equivalent impedance for a battery pack, Figure 3.10 will be used to illustrate this concept.

Figure 3.10 shows a six-cell battery pack connected in a 2 x 3 configuration. Since the series resistance can be considered as a special case of a parallel RC network with $C = 0$, and a voltage source connected in series can also be considered as a resistor connected in series, the derived equations ((3.30) to (3.32)) can be applied separately to the battery cell's parameters to determine the equivalent impedance of a battery pack. Therefore, using equations (3.30) to (3.32) for the battery pack shown in Figure 3.10, the reduced battery model and its equivalent impedances are found, as shown in Figure 3.11.

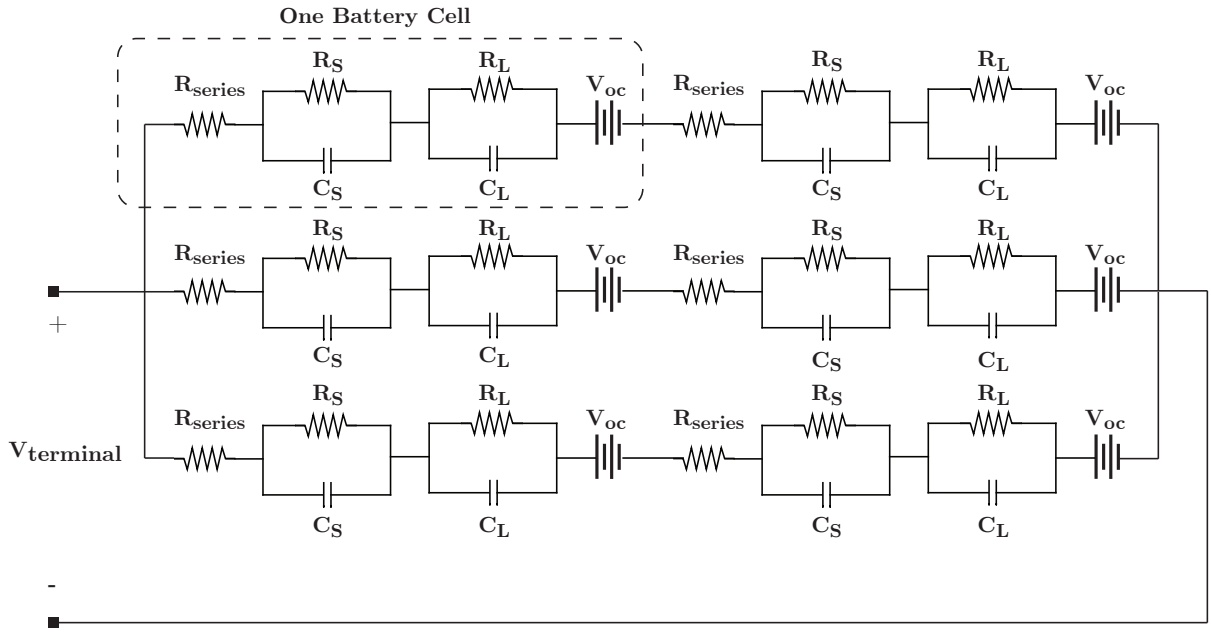

Figure 3.10: Battery pack with 2 x 3 battery cells configuration

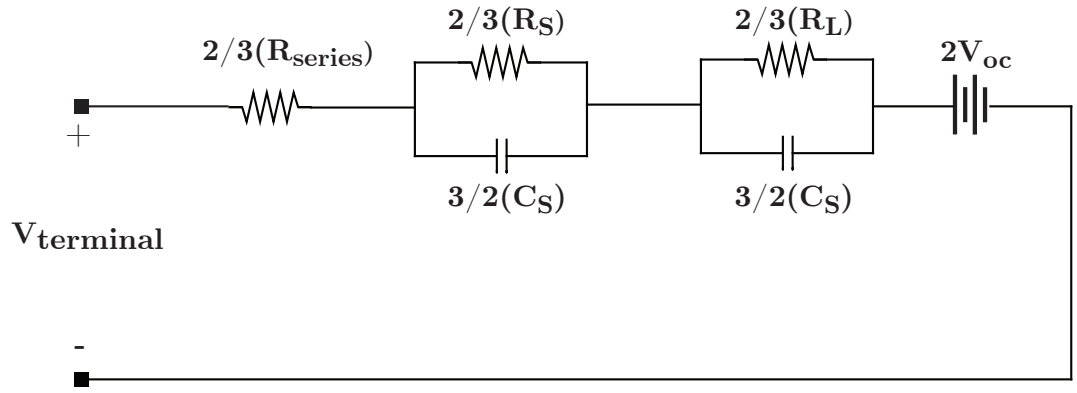

Figure 3.11: Equivalent impedance for a battery pack with 2 x 3 battery cells configuration

3.5 Summary

In summary, the electrical circuit battery model is chosen to represent the transient and steady-state behaviour of three major types of battery chemistries used in plugin vehicles. Slight modifications to the model parameter representations are needed in order to incorporate them in PSIM simulations. Lastly, one can take advantage of equations (3.30) to (3.32) to model the equivalent impedances of a battery pack in order to reduce simulation time and computational power.

Chapter 4

Design of AC-DC Converter

The design of a bidirectional battery charger for plugin vehicle is a major objective for this thesis. In Chapter **??**, the specifications and criteria of the battery charger were described, and the development of the battery model for representing the dynamic behaviour of three different types of batteries was discussed in Chapter **??**. The pre-design milestones in the design process have now been completed, and the next stage will be the actual design of the battery charger.

In a level-two, two-stage configured bidirectional battery charger, the single-phase AC-DC converter interfaces with utility grid, and is responsible for power factor control, dc-link voltage regulation and sinusoidal current waveshaping. This chapter describes the design process of the AC-DC converter to be integrated in the battery charger. It begins with a discussion of converter topology selection, followed by a study of three different AC-DC converter control methods, and concludes by identifying an appropriate control method that can satisfy the recognized responsibilities for the selected AC-DC topology based on the study findings.

4.1 Topology Selection

Single-phase voltage-source converters (VSCs) are widely used in many grid-interfaced systems, such as photovoltaic power applications [61], wind power applications [62] and power factor correction [63]. Within the family of single-phase VSCs, one of the most well-known

topologies is the single-phase full-bridge converter. Some of the notable characteristics of the full-bridge converter have already been reviewed in Chapter 2.

The single-phase full-bridge topology has been selected as the battery charger's AC-DC converter. There are several reasons why this converter is a good candidate for grid-side management in the application of bidirectional battery charger. First, the full-bridge converter can be operated to generate a three-level voltage waveform on the ac side and offers high power processing capability, reduced harmonic distortion and increased control capability [64], which are desirable for a level-two battery charger. Second, the full-bridge converter has bidirectional power flow capability and can also achieve unity power factor using proper control techniques, which satisfy the basic criteria of bidirectional battery charger. The third reason is that the full-bridge converter is a well-known topology with extensively research has been conducted in its control techniques that can be taken into advantage in the design process. The last motivation behind choosing full-bridge converter is that most two-stage topologies reviewed in Chapter 2 use this topology for grid-side management, and there is enough evidence in the literature to prove the converter's suitability in battery charger applications.

Even though there are numerous control techniques proposed for the single-phase full-bridge converter, but they need to be customized for controlling a bidirectional battery charger intended for V2G transactions. Therefore, part of the thesis' objective in designing a bidirectional battery charger is to develop a reliable controller for the AC-DC converter. The evaluation of the developed controllers is based on their ability to regulate the dc-link voltage and their ability to provide the desired power factor (not necessarily unity) in order to realize reactive power compensation.

Figure 4.1 shows the simulation model of single-phase full-bridge converter to be used during the development of the controller. IGBTs are chosen as the converter's controllable switches for their low gate power consumption and low ON-state voltage drop. The capacitance value at dc-link was chosen based on the knowledge that a large capacitor is needed for voltage filtering.

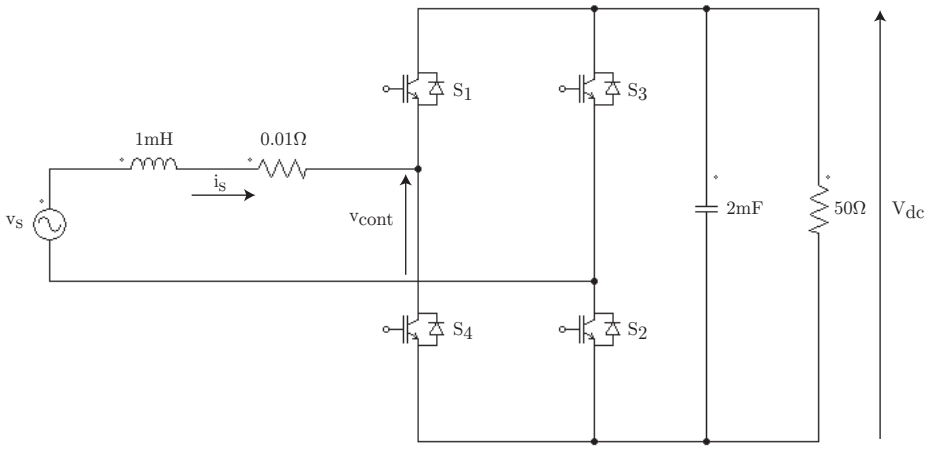

Figure 4.1: Single-phase full-bridge converter

To facilitate current control on the full-bridge converter, equation (4.1) governs the relationship between the peak value of the sinusoidal voltage on the ac side and the dc-link voltage. The modulating index, m_a, assumes values in the range $0 \leq m_a \leq 1$. This means that the full-bridge converter behaves as a boost converter, where dc-link voltage must be greater than the peak value of the sinusoidal voltage across the converter's ac terminals. For preliminary simulation, the dc-link voltage is assumed to be 350V, so that it is greater than the peak value of level 2 charging (i.e. $240V_{rms}$), but not too large to impose large voltage stress of the IGBTs.

$$\hat{V}_{cont} = m_a V_{dc} \tag{4.1}$$

The rest of the chapter steps through the design of three different AC-DC converter controllers, and discusses their advantages and drawbacks.

4.2 PI Controller

Current mode control of single-phase full-bridge converter is traditionally based on a fast control loop for controlling the sinusoidal current while regulating the dc-link voltage is done by a relatively slower control loop compared with that of the current loop. This is

a simple approach utilizing PI controllers, and is commonly referred to as the two-loop control method. Two current controllers based on the two-loop control method will be developed and their simulation results will be presented to show their performance meets the requirements.

4.2.1 Method 1 - Closed-Loop Control for Power Factor

The block diagram of method 1 controller is shown in Figure 4.2. The phase angle by which the sinusoidal current lags the grid voltage is determined first. This phase angle is the compared with the phase angle corresponding to the desired power factor to create an error term that is passed by a PI controller. The output of this PI controller forms the phase component of the reference current waveform, while the output of the PI controller tracking the dc-link voltage constitutes to the amplitude of the reference current waveform. The modulating signals for PWM, leading to switching signals of IGBTs, is generated by comparing the reference current with the actual sinusoidal current.

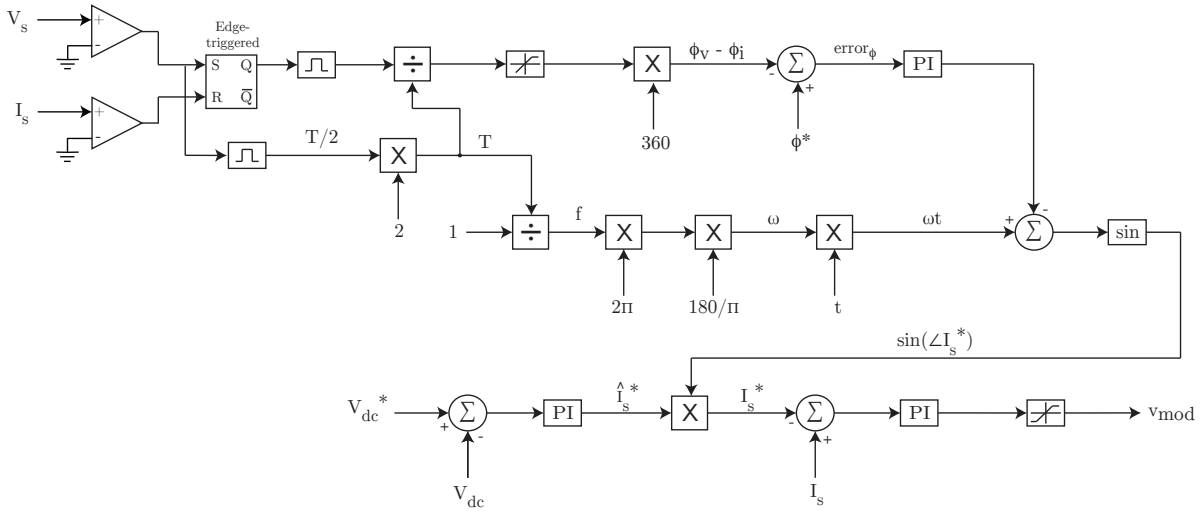

Figure 4.2: Block diagram of method 1 controller

Simulation results for the closed loop controller are shown in Figures 4.3 and 4.4. In both diagrams, the top plot displays the grid voltage and sinusoidal current waveforms,

and the bottom plot shows the dc-link voltage waveform. The simulation results shown in Figure 4.3 demonstrate the controller's capability to operate at unity power factor, but the dc-link voltage waveform contains some noticeable irregular voltage fluctuations. The simulation results shown in Figure 4.4 reveal that the controller cannot operate at other power factors without retuning the PI controllers. In this example, the desired power factor was set to 0.866 lagging, but the results showed an actual power factor close to 50° lagging. Furthermore, the dc-link voltage waveform shows the dc-link suffers from low-frequency harmonic at $20Hz$ in addition to the nominal $120Hz$. Since this controller is incapable of controlling the power factor to values other than unity, this controller is deemed inappropriate for the battery charger.

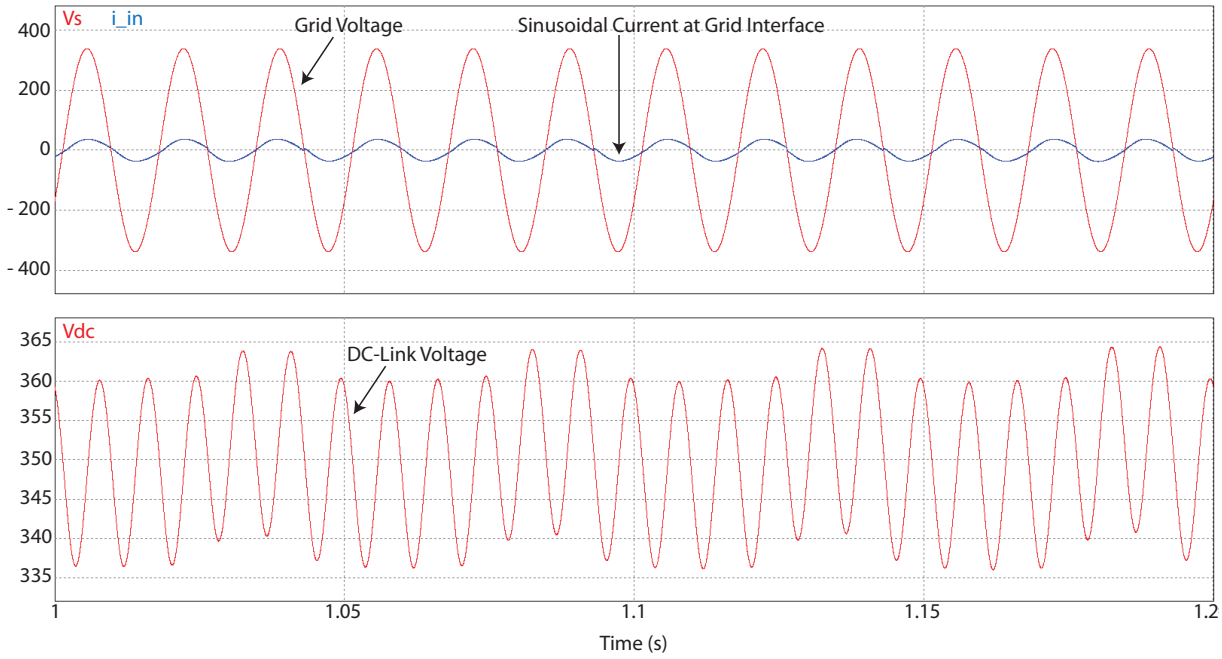

Figure 4.3: Simulation results for method 1 controller at unity power factor

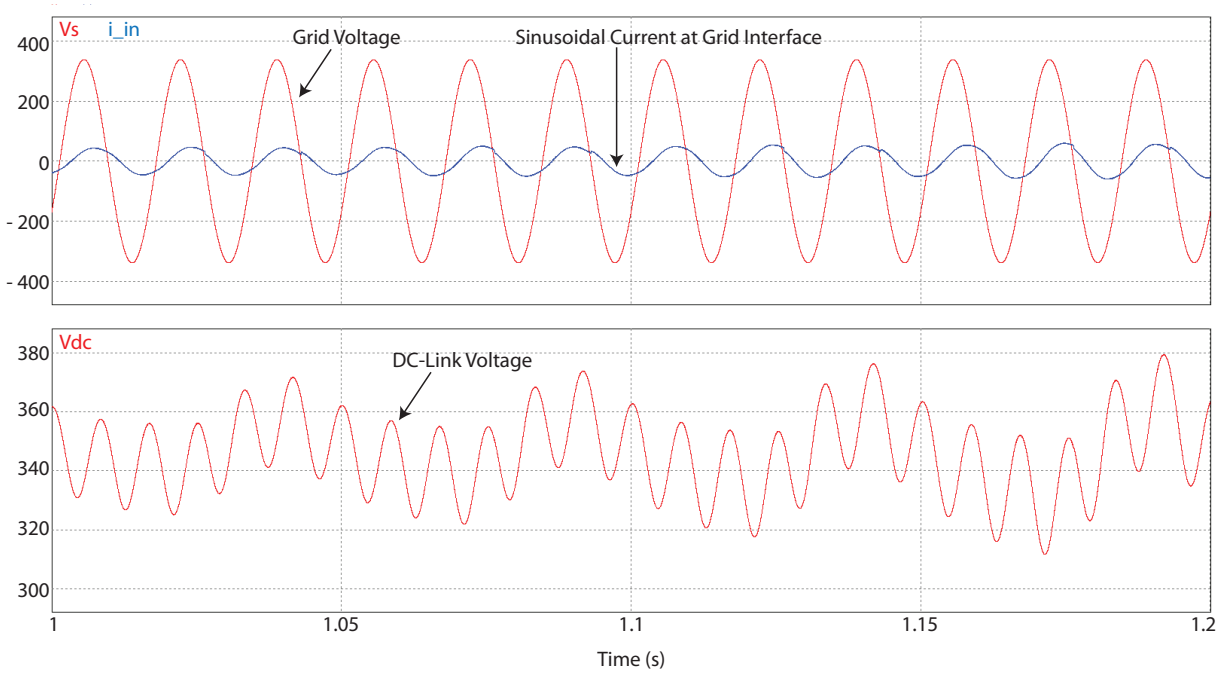

Figure 4.4: Simulation results for method 1 controller at 30° lagging

The poor performance of this controller can be attributed to the use of PI controller for tracking the power factor. For a set of tuned PI values, the controller can only provide accurate results for a small range of power factor. Retuning the PI controller is necessary whenever a new power factor is desired. This is a significant drawback of the closed-loop controller. Other drawbacks of this controller include the difficulty in tuning the PI controller for time-varying quantities, and the fact that PI control methods are known to have nonzero steady-state error in both the amplitude and phase.

4.2.2 Method 2 - Open-Loop Control for Power Factor

The incapability of PI controllers for power factor control motivated using another current-based controller to eliminate the use of PI controller to correct the power factor error. The block diagram of this controller is shown in Figure 4.5.

This controller is referred to as a controller that uses open-loop control for power factor because it does not require the sinusoidal current feedback. This method utilizes an ac

voltage reference waveform with identical frequency and amplitude as the utility grid. This voltage reference begins at 0° phase when the controller is activated. The phase angle corresponding to the desired power factor is added to or subtracted from the calculated phase difference based on whether a lagging or a leading power factor is desired. This results in an overall phase difference between the desired sinusoidal current and the ac voltage reference. The overall phase difference is fed back as the phase component of the reference current waveform. Similar to the closed-loop controller, the output of the PI controller used for dc-link voltage tracking constructs the amplitude of the reference current waveform. Finally, the modulating signal is generated by comparing the reference current with the grid-side sinusoidal current.

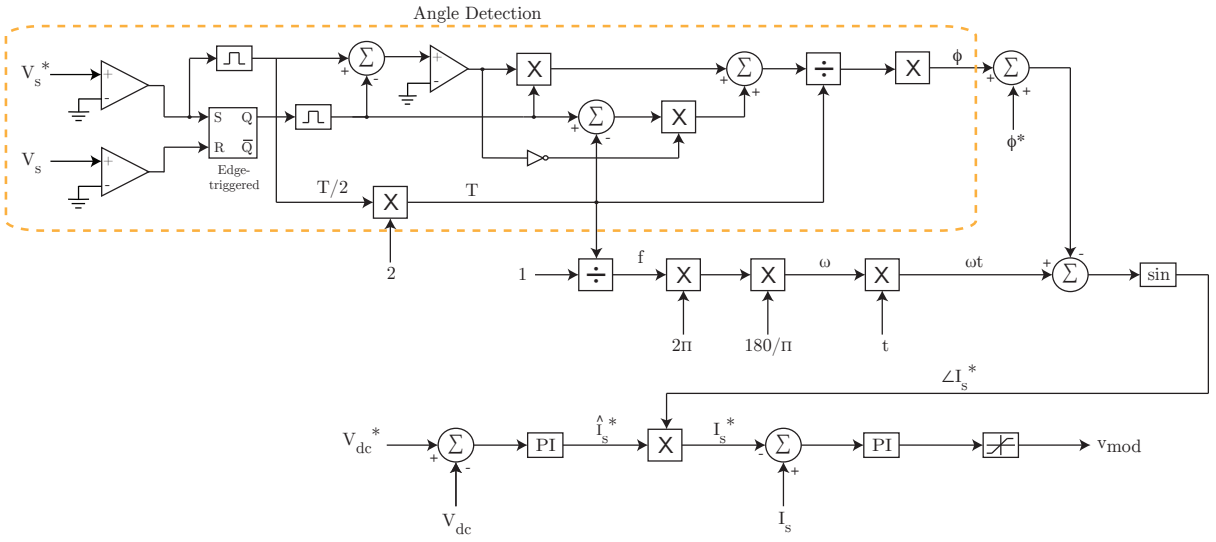

Figure 4.5: Block diagram of method 2 controller

Simulation results for method 2 controller are shown in Figures 4.6 to 4.8. Similar to previous results, the top plot shows the grid voltage and sinusoidal current waveforms, and the bottom plot shows the dc-link voltage waveform. The method 2 controller produces less voltage ripples in all cases, i.e. unity power factor and 30° lagging, in comparison to the method 1 controller. Futhermore, the method 2 achieves better power factor control since the phase angle error at the ac current is less than what was observed in method 1 controller. Therefore, these results prove the open-loop controller's ability to achieve unity power factor, and also demonstrate its ability to control the desired power factor with

higher accuracy compared to that of the closed-loop controller. In addition, these results show the open-loop controller can better regulate the dc-link voltage.

Although the open-loop controller can easily be implemented and can attain better results in comparison with the closed-loop controller, it does not reduce the difficulty in PI tuning and does not result in a nonzero steady-state error.

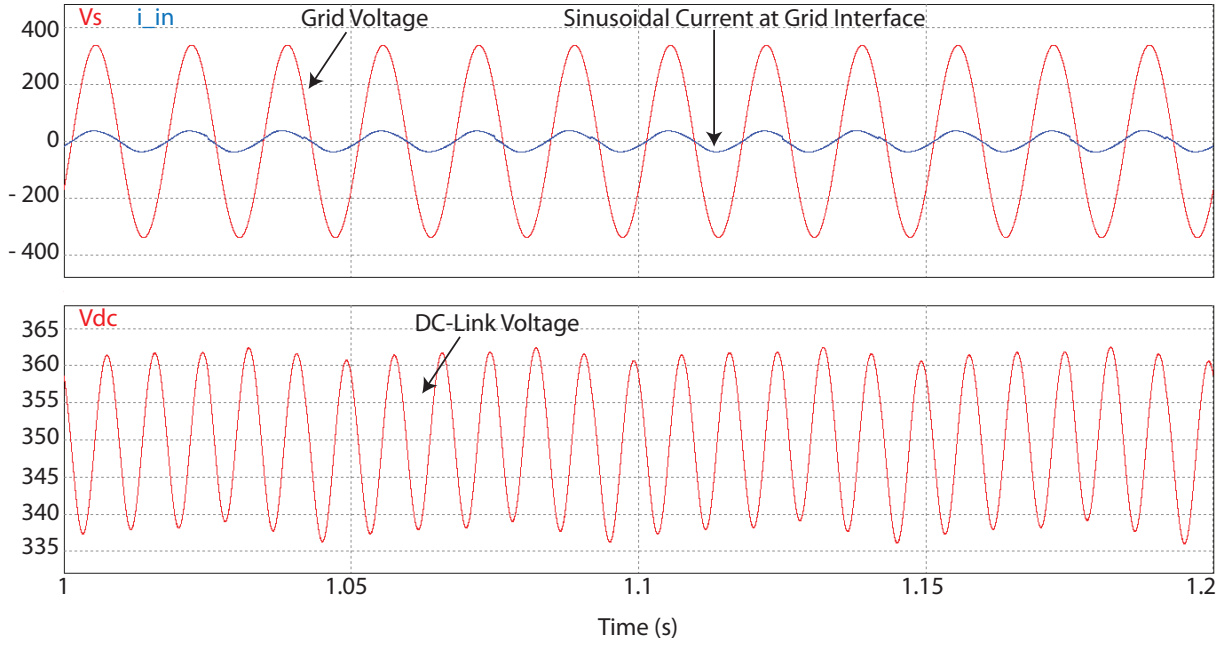

Figure 4.6: Simulation results for method 2 controller at unity power factor

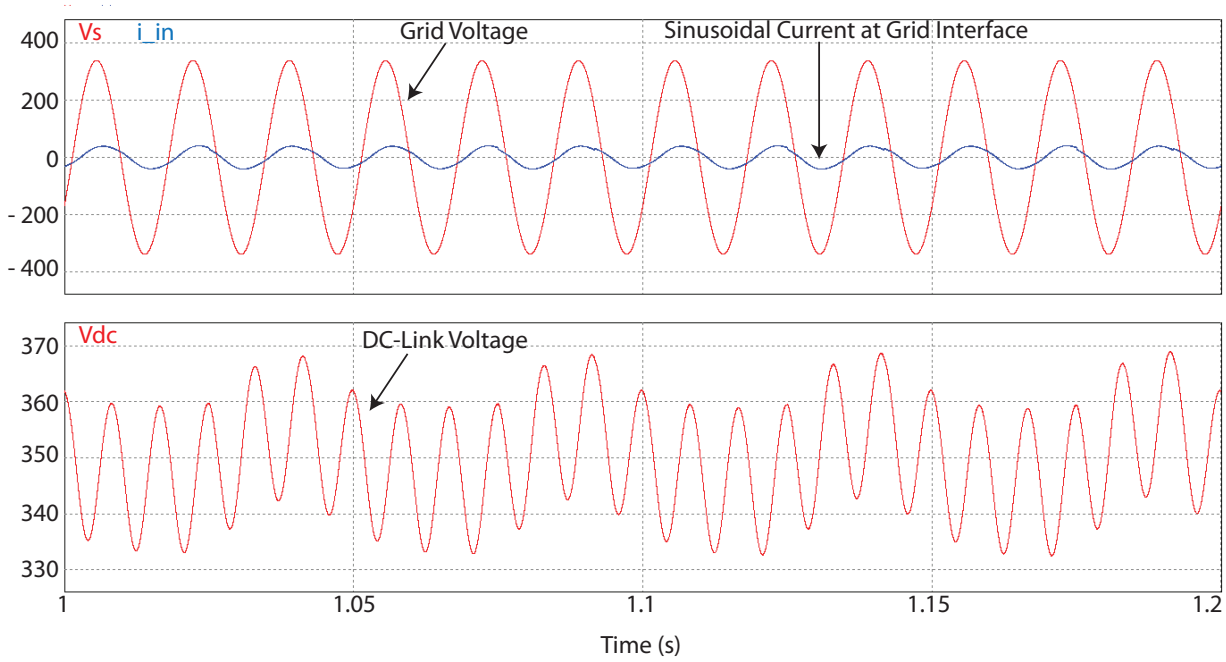

Figure 4.7: Simulation results for method 2 controller at 30° lagging

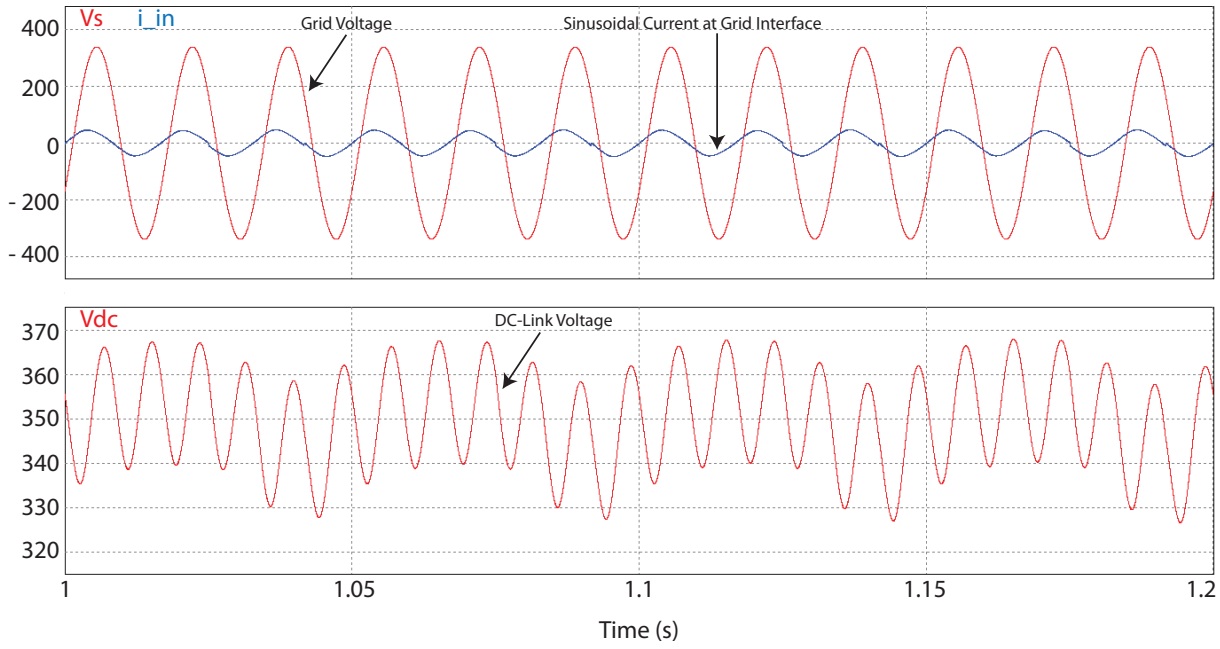

Figure 4.8: Simulation results for method 2 controller at 30° leading

4.3 DQ Synchronous Frame Control

Traditional PI control methods are known for their drawbacks in the form of nonzero steady-state error in both amplitude and phase caused by time variant current and voltage quantities, and the difficulty in accurate PI controller tuning. These drawbacks were observed from the development of the two PI controllers. This promotes the idea of using a synchronous reference frame controller, where time varying quantities are transformed to time invariant quantities so that an AC-DC converter controller can be designed in the same way as a that for a DC-DC converter.

Direct-quadrature (DQ) synchronous reference frame is extensively used in controlling three-phase converter systems. This control technique first transforms the ABC components of a three-phase system into the $\alpha\beta$ stationary reference frame, and from the $\alpha\beta$ frame the quantities are transformed to the DQ synchronous reference frame. The main advantage for such control method is that control manipulations are carried out on the

imaginary dc signals before recovering the three ac modulating signals using inverse transformation.

Performing control calculations using dc quantities simplifies the control process and achieves zero steady-state error. Because of this advantage, control using DQ synchronous frame seems attractive for single-phase converters as well. DQ synchronous frame controller for single-phase grid-connected converters have been discussed in literature [62,65–67], but this type of controller has not been adopted in the application of battery charger. As a result, this thesis attempts to derive a DQ synchronous frame controller for the single-phase full-bridge converter shown in Figure 4.1.

4.3.1 Source Voltage

The nature of DQ transformation requires at least two ac signals, where single-phase converters are connected to only one signal on their ac side. Therefore, in order to implement DQ synchronous frame for a single-phase system, a second fictitious orthogonal signal is required. Suppose the source voltage is defined as $v_s = \hat{V}\cos(\omega t + \alpha)$. It is assumed that v_s is the α-component for the $\alpha\beta$ stationary frame. The orthogonal β-component, also known as the fictitious component, is defined to have a 90° phase delay with respect to α. Equations (4.2) and (4.3) describe the projection of voltage vector $\overrightarrow{V}$ onto the α- and β-axis respectively.

$$V_\alpha = \hat{V}\cos(\omega t + \alpha) \tag{4.2}$$

$$V_\beta = \hat{V}\sin(\omega t + \alpha) \tag{4.3}$$

where $\overrightarrow{V}$ is the peak value of the sinusoidal functions and α is an arbitrary phase angle.

The transformation from $\alpha\beta$ stationary frame to DQ synchronous frame is done by rotating the $\alpha\beta$ frame through angle $\theta = \omega t + \alpha$ in counterclockwise direction so that the resultant d-axis is align with vector $\overrightarrow{V}$. Therefore, DQ frame will rotate at the fundamental frequency ω. The resulting d- and q-axis components will have constant magnitudes rotating at steady-state, rotating at the fundamental frequency. $\alpha\beta$ to DQ transformation ensures that vector $\overrightarrow{V}$ has only a d-axis component and no q-component. Figure 4.9 illustrates this concept.

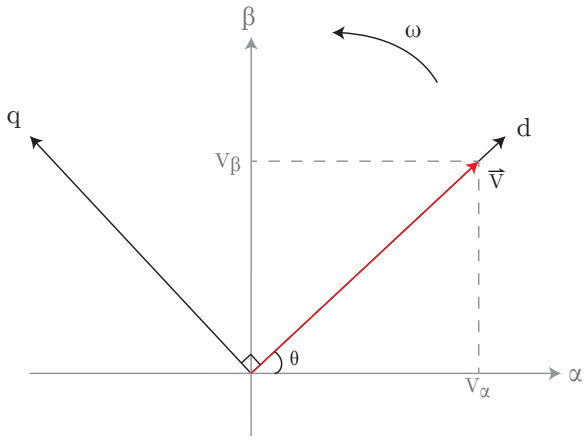

Figure 4.9: $\alpha\beta$ and DQ reference frames

The $\alpha\beta$ to DQ transformation is defined by equation (4.4), and the inverse transformation is given by equation (4.5).

$$\begin{bmatrix} d \\ q \end{bmatrix} = \begin{bmatrix} \cos\theta & \sin\theta \\ -\sin\theta & \cos\theta \end{bmatrix} \begin{bmatrix} \alpha \\ \beta \end{bmatrix} \tag{4.4}$$

$$\implies \begin{bmatrix} V_d \\ V_q \end{bmatrix} = \begin{bmatrix} \cos\theta & \sin\theta \\ -\sin\theta & \cos\theta \end{bmatrix} \begin{bmatrix} V_\alpha \\ V_\beta \end{bmatrix} = \hat{V} \begin{bmatrix} 1 \\ 0 \end{bmatrix}$$

$$\begin{bmatrix} \alpha \\ \beta \end{bmatrix} = \begin{bmatrix} \cos\theta & -\sin\theta \\ \sin\theta & \cos\theta \end{bmatrix} \begin{bmatrix} d \\ q \end{bmatrix} \tag{4.5}$$

4.3.2 PLL Circuit

The objective of the PLL circuit is to determine the fundamental frequency of the source voltage as well as to produce the phase angle θ that synchronizes the control circuit. The block diagram of the PLL circuit in the controller is shown in Figure 4.10. The fundamental frequency ω is calculated by feeding V_q into a PI controller. Then, the phase angle θ is obtained by integrating the calculated frequency ω and resetting the integrator at every 2π radians (i.e., at the end of each cycle).

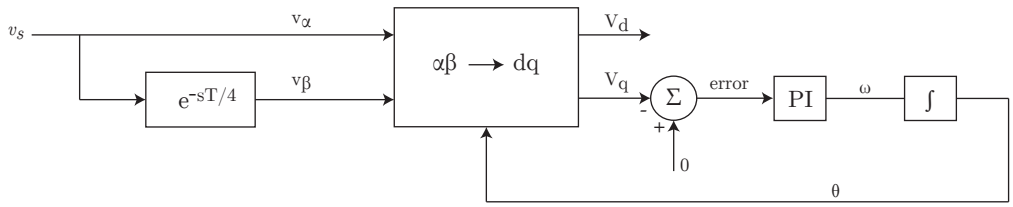

Figure 4.10: PLL circuit

4.3.3 Source Current

The sinusoidal current must also go through the transformation in order to convert the waveform into a time invariant quantity. A transformation procedure similar to that applied previously to the grid voltage should applied to the sinusoidal current as well. Suppose the sinusoidal current carries the form of equation (4.6), and it is assumed that this is the α-component in $\alpha\beta$ frame. Therefore, the β-component, which is defined to be a 90° delayed with respect to the waveform of i_α, has the form of equation (4.7).

$$i_s = i_\alpha = \hat{I}\cos(\omega t + \alpha + \phi) \tag{4.6}$$

$$i_\beta = \hat{I}\sin(\omega t + \alpha + \phi) \tag{4.7}$$

After performing the DQ transformation, the resulting dq-components are given by equations (4.8) and (4.9).

$$I_d = \hat{I}\cos(\phi) \tag{4.8}$$

$$I_q = \hat{I}\sin(\phi) \tag{4.9}$$

4.3.4 Current Reference

A reference current waveform is mandatory for current waveshaping. In the time-varying frame, the reference current is defined to be $i_s^* = \hat{I}^*\cos(\omega t + \alpha + \phi^*)$, which has frequency ω and phase angle α identical to the grid voltage waveform but with an additional angle ϕ^* corresponding to the desired power factor. In $\alpha\beta$ frame, the α-component is equivalent to

i_s^*, as given in equation (4.10), and the orthogonal β-component is given by equation (4.11).

$$i_s^* = i_\alpha^* = \hat{I}^* \cos(\omega t + \alpha + \phi^*) \tag{4.10}$$

$$i_\beta^* = \hat{I}^* \sin(\omega t + \alpha + \phi^*) \tag{4.11}$$

After the DQ transformation, this results in time invariant quantities of the reference current described by equations (4.12) and (4.13) will result.

$$I_d^* = \hat{I}^* \cos(\phi^*) \tag{4.12}$$

$$I_q^* = \hat{I}^* \sin(\phi^*) \tag{4.13}$$

4.3.5 Complex Power Representation

Each vector in DQ frame can be considered to be composed of a real part and an imaginary part, where the d-axis component forms the real coordinate and the q-axis component constructs the imaginary coordinate. An example of a voltage vector and a current vector in DQ frame are given in equations (4.14) and (4.15).

$$\vec{V} = V_d + jV_q \tag{4.14}$$

$$\vec{I} = I_d + jI_q \tag{4.15}$$

One advantage of transforming into the DQ frame is that the active and reactive power processed by the converter can be easily represented by utilizing the voltage and current vectors. By substituting equations (4.14) and (4.15) into the complex power relation $S = \vec{V}\vec{I}^*$, the active and reactive power relationships can be derived.

$$\begin{aligned} S = \vec{V}\vec{I}^* &= P + jQ \\ &= (V_d + jV_q)(I_d - jI_q) \\ &= (V_d I_d + V_q I_q) + j(V_q I_d - V_d I_q) \\ &= (V_d I_d) - j(V_d I_q) \quad \text{since } V_q = 0 \end{aligned} \tag{4.16}$$

Note that active and reactive powers can be controlled by d- and q-axis components of current. The desired power factor of the sinusoidal current can be translated into I_q^* by

taking advantage of equation (4.16). The relationship between desired power factor ϕ^* and I_q^* is derived as follow:

$$\begin{aligned} PF &= \cos\left(\tan^{-1}\frac{Q}{P}\right) \\ &= \cos\left(\tan^{-1}\frac{-I_q^*}{I_d}\right) \\ Iq^* &= -I_d \cdot \tan(cos^{-1}PF) \end{aligned} \tag{4.17}$$

4.3.6 Steady-State Control Signals

The relationship between $\alpha\beta$ frame and DQ frame in phasor notation is given in equations (4.18) and (4.19) for voltage and current respectively.

$$v_{\alpha\beta} = v_\alpha + jv_\beta = (V_d + jV_q)e^{j\theta} \tag{4.18}$$

$$i_{\alpha\beta} = i_\alpha + ji_\beta = (I_d + jI_q)e^{j\theta} \tag{4.19}$$

The backward proof for equation (4.19) is provided below. The proof for equation (4.18) is not provided since it follows an identical procedure as used for (4.19).

$$\begin{aligned} &(I_d + jI_q)e^{j\theta} \\ &= \hat{I}(\cos\phi + j\sin\phi)(\cos\theta + j\sin\theta) \\ &= \hat{I}\left[(\cos\phi\cos\theta - \sin\phi\sin\theta) + j(\sin\phi\cos\theta + \cos\phi\sin\theta)\right] \\ &= \frac{1}{2}\hat{I}\big[\left[\cos(\phi-\theta) + \cos(\phi+\theta) - \cos(\phi-\theta) + \cos(\phi+\theta)\right] \\ &\qquad + j\left[\sin(\phi+\theta) + \sin(\phi-\theta) + \sin(\phi+\theta) - \sin(\phi-\theta)\right]\big] \\ &= \hat{I}\left[\cos(\phi+\theta) + j\sin(\phi+\theta))\right] \\ &= i_\alpha + ji_\beta \end{aligned}$$

Assuming that the full-bridge converter is lossless, equation (4.20) describes the sinusoidal current at the grid interface.

$$v_{\alpha\beta} - v_{cont_{\alpha\beta}} = L\frac{di_{\alpha\beta}}{dt} + Ri_{\alpha\beta} \tag{4.20}$$

The steady-state control signals for the controllable switches can be derived by substituting $v_{cont_{\alpha\beta}} = (V_{cont_d} + jV_{cont_q})e^{j\theta}$ and equations (4.18) and (4.19) into equation (4.20).

$$L\frac{di_{\alpha\beta}}{dt} + Ri_{\alpha\beta} = v_{\alpha\beta} - v_{cont_{\alpha\beta}}$$

$$L\frac{d}{dt}\left[(I_d + jI_q)e^{j\theta}\right] + R(I_d + jI_q)e^{j\theta} = (V_d)e^{j\theta} - (V_{cont_d} + jV_{cont_q})e^{j\theta}$$

$$L\left[e^{j\theta}\frac{d}{dt}(I_d + jI_q) + (I_d + jI_q)\frac{d}{dt}e^{j\theta}\right] + R(I_d + jI_q)e^{j\theta} = (V_d)e^{j\theta} - (V_{cont_d} + jV_{cont_q})e^{j\theta}$$

$$L\left[e^{j\theta}\left(\frac{d}{dt}I_d + j\frac{d}{dt}I_q\right) + je^{j\theta}\left(I_d + jI_q\right)\frac{d\theta}{dt}\right] + R(I_d + jI_q)e^{j\theta} = (V_d)e^{j\theta} - (V_{cont_d} + jV_{cont_q})e^{j\theta}$$

$$L\left[\frac{dI_d}{dt} + j\frac{dI_q}{dt} + j\omega I_d - \omega I_q\right] + R(I_d + jI_q) = V_d - (V_{cont_d} + jV_{cont_q})$$

Separating the real and imaginary terms leads to equations (4.21) and (4.22).

$$L\frac{dI_d}{dt} - \omega LI_q + RI_d = V_d - V_{cont_d} \Longrightarrow V_{cont_d} = -L\frac{dI_d}{dt} + \omega LI_q - RI_d + V_d \tag{4.21}$$

$$L\frac{dI_q}{dt} + \omega LI_d + RI_q = -V_{cont_q} \Longrightarrow V_{cont_q} = -L\frac{dI_q}{dt} - \omega LI_d - RI_q \tag{4.22}$$

By putting the derivative terms equal to zero, the steady-state control signals in DQ frame are given in equations (4.23) and (4.24).

$$V_{cont_d} = \omega LI_q - RI_d + V_d \tag{4.23}$$

$$V_{cont_q} = -\omega LI_d - RI_q \tag{4.24}$$

The block diagram of the DQ synchronous frame controller is shown in Figure 4.11. The output of the PI controller for dc-link voltage produces the value for I_d^* with the main duty of controlling the active power transfer. On the other hand, the value of I_q^*, determined by the desired power factor, controls the amount of reactive power transfer. For example, unity power factor can be achieved by letting $I_q^* = 0$. DC quantities, I_d and I_q, are compared with their respective reference values (i.e. I_d^* & I_q^*). The two PI controllers ensure zero steady-state errors. Up to this point, the transient portion of the controller, responsible for tracking the instantaneous value of the dc-link voltage and sinusoidal current has been covered.

The remaining part of the controller is known as the steady-state portion of the controller. This part of the controller implements the derived steady-state control signals (equations (4.23) & (4.24)). The gains ωL and R decouple V_d and V_q, and improve the dynamic response of the controller. A feedforwared of the peak value of the grid voltage V_d is also applied to minimize the effect of its perturbations. The dc control signals V_{cont_d} and V_{cont_v} represent the components of converter's ac side voltage in DQ frame, and thus they need to be scaled down by the instantaneous value of the dc-link voltage V_{dc} in order to find the components of the modulating signal v_{mod} in DQ frame. The scaled DQ frame control signals are then transformed back to $\alpha\beta$ frame. After transformation, the β-component (v_β) is discarded and the α-component (v_α) is v_{mod}. Using unipolar PWM switching method, v_{mod} is applied to the controllable switches.

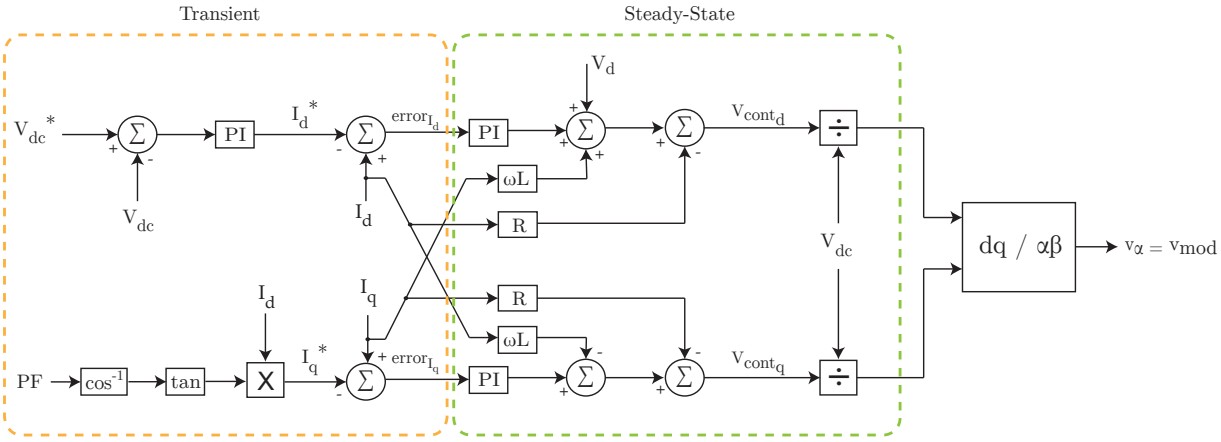

Figure 4.11: Block diagram of DQ synchronous frame controller

4.3.7 Simulation Results

Waveforms shown in Figures 4.12 to 4.16 are the simulation results of the DQ synchronous frame controller. In Figure 4.12, the top plot shows the grid voltage and the fictitious orthogonal signal; the middle plot shows the d-component of the transformed grid voltage (equivalent to the peak value of grid voltage) and the q-component of the transformed grid voltage (equals to 0); and the bottom plot shows the phase angle that synchronizes the control circuit.

Figure 4.13 shows the frequency of the grid voltage in radian per second, the dc quantities of the modulating signal before DQ to $\alpha\beta$ transformation, and the ac quantity of the modulating signal in $\alpha\beta$ frame.

Figure 4.14 demonstrates unity power factor correction and the regulation of the dc-link voltage. Figures 4.15 and 4.16 illustrate the power factor controllability at 30° lagging and leading respectively, and the stability of the dc-link voltage.

The simulation results verified the correctness of the mathematical derivations for the DQ controller. The results reveal that, of the three controller examined, the DQ controller offers the highest accuracy in power factor control since there are less errors between the actual phase angle of ac current with respect to the ac voltage and the desired power factor in the three studied cases. The results also reveal that the DQ controller provides better voltage regulation in comparison to the two PI controllers. The dc-link voltage in the DQ controller has less voltage fluctuation, which is especially noticeable at 30° leading compared with PI controllers. This is important when the battery charger provides reactive power compensation to the utility grid.

Due to the use of synchronous frame, all the time varying quantities are transformed in time invariant quantities at steady-state, allowing the controller to be designed in a similar fashion as for a DC-DC converter and achieving zero steady-state error. Furthermore, tuning PI controllers for dc quantities is much easier than tuning for ac quantities. All these benefits combined make the DQ controller an ideal controller for the full-bridge converter in the battery charger. The slight drawback for the DQ controller is the increased complexity in implementation.

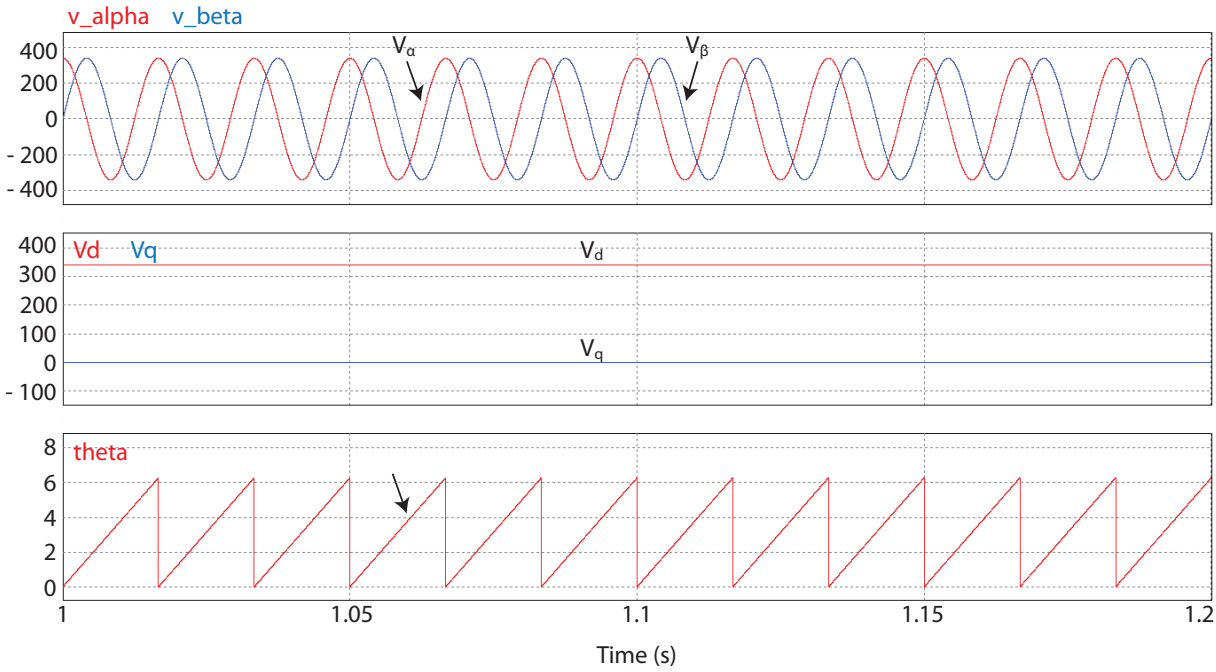

Figure 4.12: Simulation results for DQ synchronous frame controller. Top: grid voltage and fictitious orthogonal signal. Middle: d- and q-component of grid voltage. Bottom: synchronizing phase angle produced by PLL.

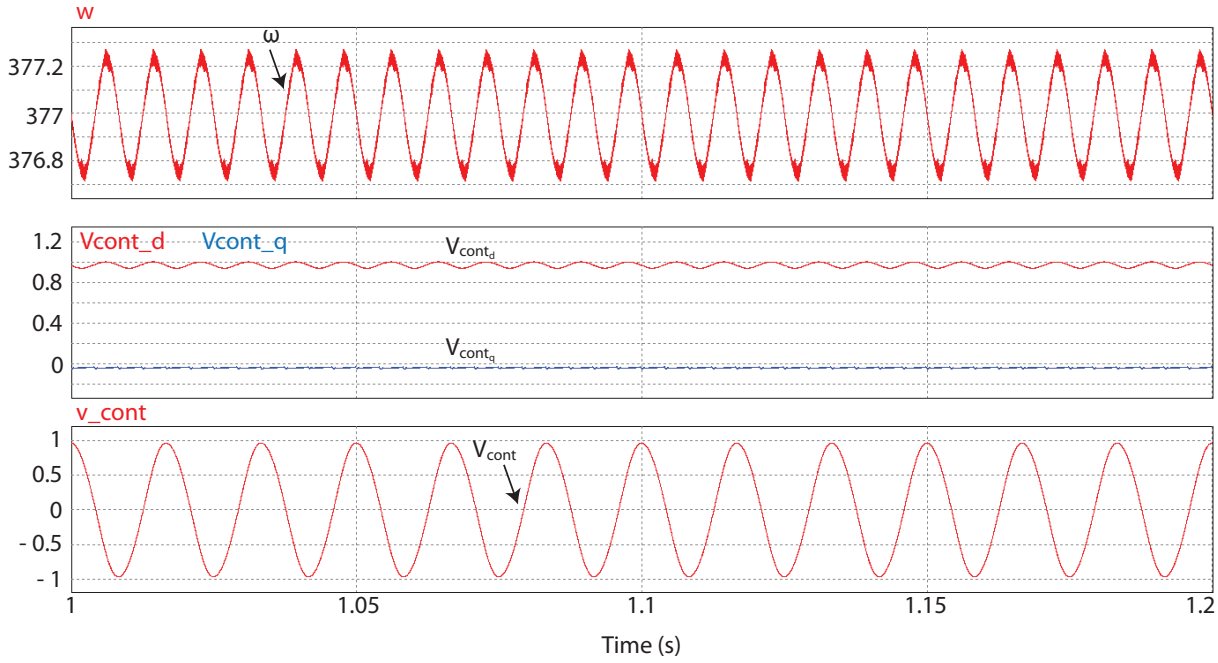

Figure 4.13: Simulation results for DQ synchronous frame controller. Top: utility grid frequency in rad/sec. Middle: controllable switch modulating signal in DQ frame. Bottom: controllable switch modulating signal in $\alpha\beta$ frame.

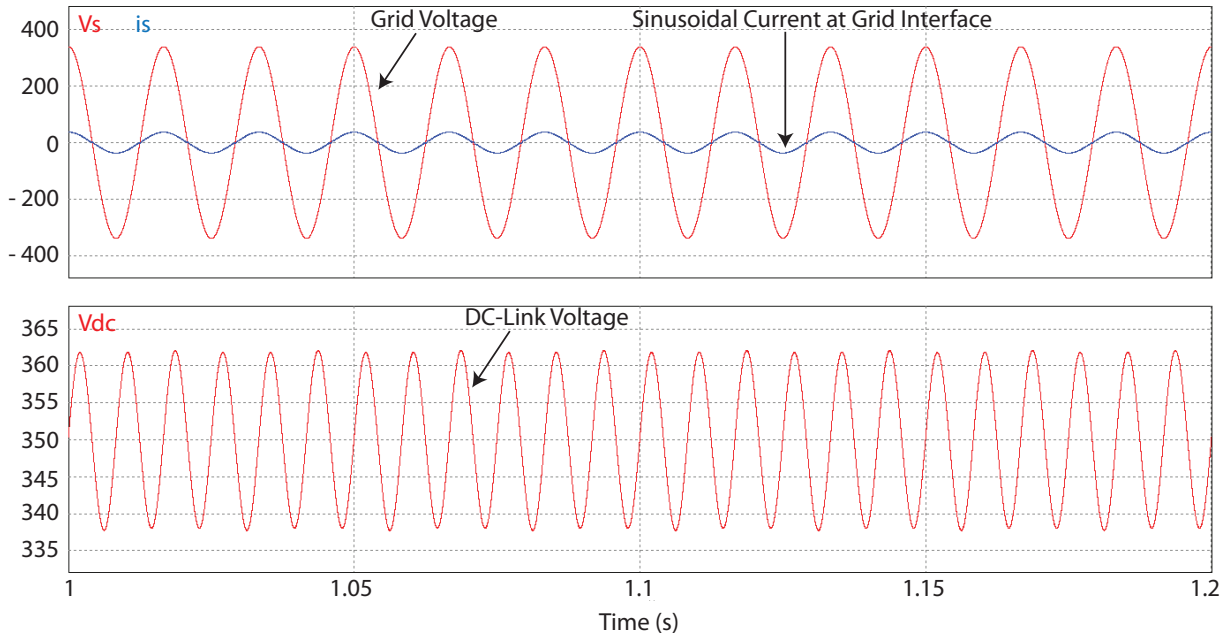

Figure 4.14: Simulation results for the DQ synchronous frame controller at unity power factor

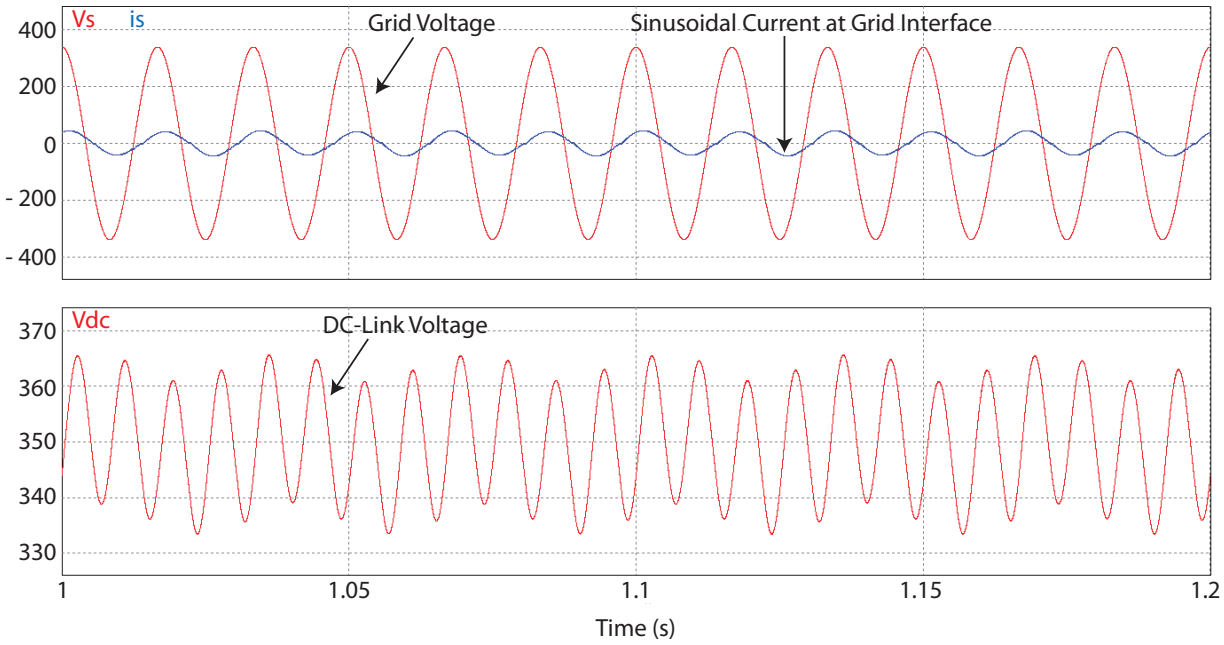

Figure 4.15: Simulation results for the DQ synchronous frame controller at 30° lagging

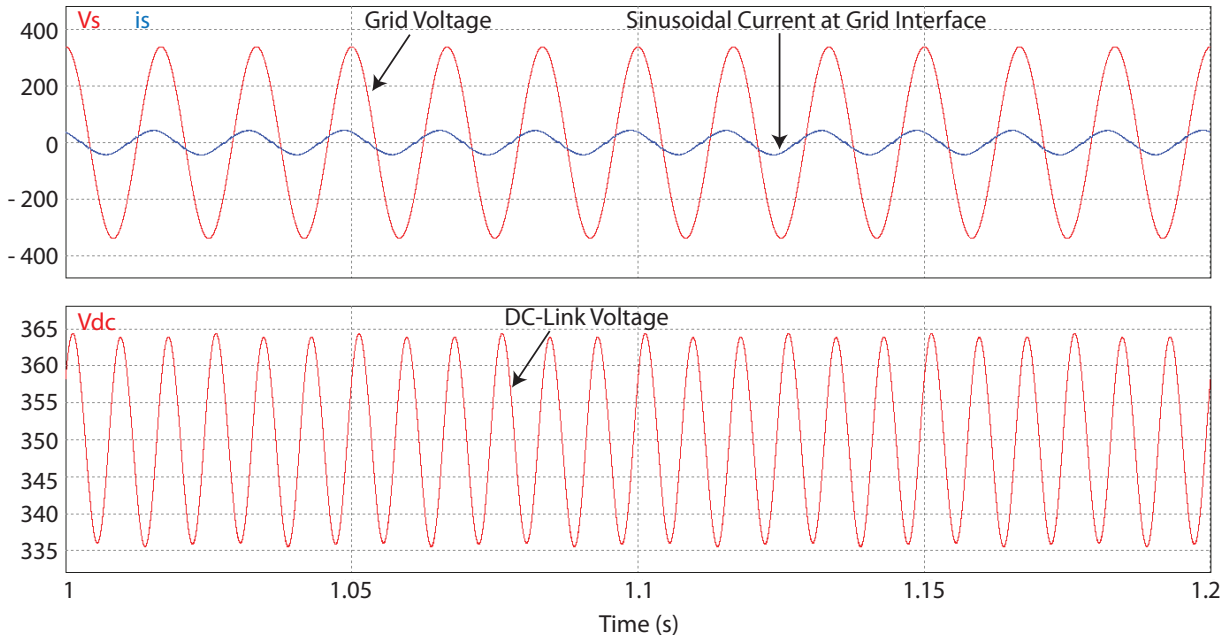

Figure 4.16: Simulation results for the DQ synchronous frame controller at 30° leading

4.4 Summary

Single-phase full-bridge topology was selected as the AC-DCconverter for grid-side management in the battery charger. The full-bridge converter has many attractive features that are well-suited for the level 2 charger, including high power capability, power factor correction and reduced harmonics. Traditional controllers and DQ synchronous frame controller were simulated to examine their capabilities in dc-link voltage regulation, ac current waveshaping and power factor control. PI controllers have nonzero steady-state errors caused by time varying quantities, and are difficult to tune. DQ synchronous frame controller provides benefit of achieving zero steady-state error by transforming time varying quantities into dc quantities at steady-state. Simulation results also revealed that the DQ controller had better dynamic characteristics in control. Although the simulations presented in this chapter only demonstrated ac to dc power transfer, it can still be concluded the DQ controller offers a better performance for the battery charger. As results, it is chosen as the controller for the full-bridge converter which makes the grid interface of

the charger. The effectiveness of the DQ controller in V2G power transaactions (dc to ac power transfer) will be demonstrated in Chapter 6 when the design of bidirectional battery charger design is completed.

Chapter 5

Design of DC-DC Converter and Simulation Results of Battery Charger

5.1 Design of DC-DC Converter

In addition to a bidirectional AC-DC converter, a bidirectional DC-DC converter is an essential building block for a two-stage bidirectional battery charger. It interfaces the plugin vehicle's battery pack with the dc-link of the charger. Its primary purpose is to control the charging/discharging current or the terminal voltage of the battery pack depending on the mode of operation.

Bidirectional DC-DC converters with low cost, high power capability, high efficiency, low weight and small volume are important for an on-board battery charger. At this state, only non-isolated bidirectional DC-DC converters are considered for the battery charger and incorporating isolation is left for future work..

Six non-isolated bidirectional DC-DC converters are selected as potential candidates for the battery charger. The performance of these topologies are compared in this chapter. The control technique for the bidirectional DC-DC converter is also discussed.

5.1.1 Comparison of DC-DC Converters Topologies

The six selected non-isolated bidirectional DC-DC converters are bidirectional buck-boost converter, bidirectional Ćuk converter, bidirectional SEPIC/Luo converter, half-bridge converter, full-bridge converter and neutral point clamped three-level converter.

The specifications for the DC-DC converter are listed in Table 5.1. The power rating of the converter is 15kW; this value is based on a maximum 50A charging current measured at the dc inductor. The dc-link voltage is maintained at 350V and the battery pack voltage is at 300V. The switching frequency of the DC-DC converter is 20kHz, which is identical to that of the AC-DC converter (discussed in Chapter 4) for synchronization purposes. The size of the battery-side inductor is calculated based on a 10% peak-to-peak inductor current ripple.

One important factor in choosing a DC-DC converter for an on-board battery charger is the size of the inductors. While inductors are needed for current filtering, they lead to very heavy, bulky and expensive converters. Thus, it is of interest to minimize the inductor ratings to have a compact and cost-effective DC-DC converter.

Table 5.1: Specifications of bidirectional DC-DC converter

Rated Power	15kW
DC-link Voltage	350V
Battery Pack Voltage	300V
Switching Frequency	20kHz
Maximum Inductor Current Ripple	10% (Peak to Peak)

Bidirectional Ćuk Converter, Bidirectional SEPIC/Luo Converter and Half-Bridge Converter

The bidirectional Ćuk converter is shown in Figure 5.1. When power flows from the dc-link to the battery pack (charging mode), switch S_2 is active and switch S_1 in inactive. The opposite switch configuration is true when power flows from the battery pack to the dc-link (discharging mode). Unlike buck or boost converter, the energy transfer takes place through the capacitor and not the inductor. The Ćuk converter has low-pass filters on

both input and output sides. There are two inductors and three capacitors in total. Each switch has a voltage rating of at least $V_1 + V_2$.

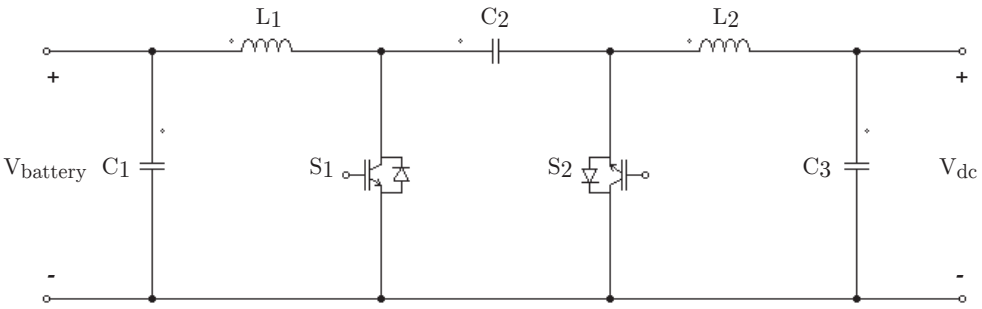

Figure 5.1: Bidirectional Ćuk converter

Figure 5.2 presents the SEPIC/Luo converter. The SEPIC/Luo converter's characteristics are very simiar to those of Ćuk converter. Both converters convert power using two active switches. Also, switch S_2 is active and switch S_1 is inactive when the converter is in charging mode of operation, whereas switch S_1 is active and switch S_2 is inactive when the converter is in discharging mode of operation (i.e., transferring power from the battery pack to the dc-link). The component count in a SEPIC/Luo converter is identical to that of a Ćuk converter. Each switch in this converter also has a voltage rating of at least $V_1 + V_2$.

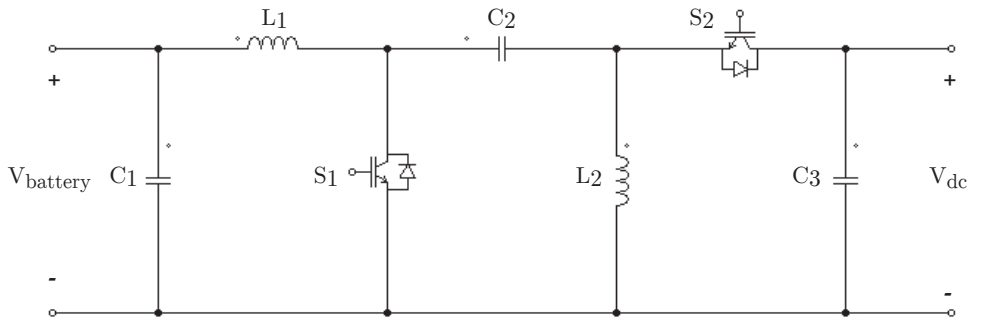

Figure 5.2: SEPIC/Luo converter

The half-bridge converter is shown in Figure 5.3. It can be seen that the half-bridge

converter uses one less inductor and one less capacitor compared with Ćuk and SEPIC/Luo converters. When the half-bridge converter operates as a buck converter, switch S_2 is active, and when it operates as a boost converter, switch S_1 in active. The two switches receive complimentary switching signals. The voltage rating of each switch in this converter should be at least equal to V_2.

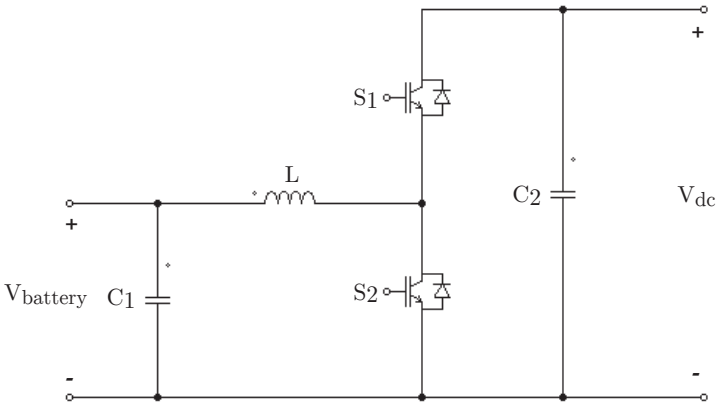

Figure 5.3: Half-bridge converter

The performance of the Ćuk converter, SEPIC/Luo converter and half-bridge converter for hybrid electric vehicle application have been thoroughly analyzed and compared in [68].

The results of comparison show that half-bridge converter has the following advantages over Ćuk converter and SEPIC/Luo converter.

- The inductor size is reduced to half;
- The component count if lower;
- The switch voltage stress is lower; and
- It can achieve potentially higher efficiencies because of lower inductor conduction losses, and lower switching and conduction losses in active components.

From the above-identified advantages, the half-bridge converter appears to be a better power electronic interface for the battery charger in comparison with the Ćuk and SEPIC/Luo converter.

The inductor size for the half-bridge based on the specifications can be calculated using the design equation below.

$$L = \frac{V_{battery} \cdot (1-d)}{\Delta I_L \cdot f_s} \qquad \text{where } d = \frac{V_{battery}}{V_{dc}} \tag{5.1}$$
$$L = \frac{300 \cdot (1-0.8571)}{5 \cdot 20000} = 0.429mH$$

Bidirectional Buck-Boost Converter

Figure 5.4 presents the bidirectional buck-boost converter. It converts power using two active switches. The voltage at V_1 must be greater than the voltage at V_2. The two switches receive complimentary signal when they are operating simultaneously.

The topology shown in Figure 5.4 has an extra inductor in comparison with the half-bridge converter, but this inductor can be eliminated since current filtering may not be necessary at the dc-link. Consequently, only inductor L_2 is needed if this topology is chosen for the battery charger.

The inductor size for L_2 is first derived and then calculated in equation 5.2 based on the specifications.

$$L_2 = \frac{V_{battery} \cdot (1-d)}{\Delta I_{L_2} \cdot f_s} \qquad \text{where } d = \frac{V_{battery}}{V_{dc}} \tag{5.2}$$
$$L_2 = \frac{300 \cdot (1-0.8571)}{5 \cdot 20000} = 0.429mH$$

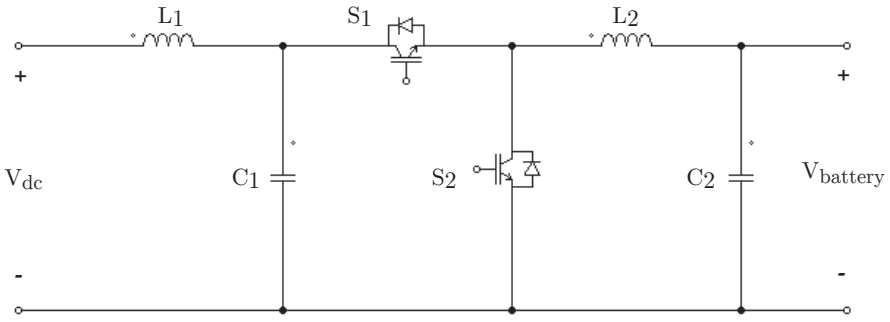

Figure 5.4: Bidirectional buck-boost converter

Full-Bridge Converter

The full-bridge converter is shown in Figure 5.5. This is a four-quadrant converter that uses four controllable switches to perform bidirectional power flow. If unipolar PWM switching method is employed, the effective switching frequency sensed at the output frequency will be double of the actual switching frequency. Potentially, this allows the filtering components to be smaller. Full-bridge converter uses two controllable switches more than what is used in the half-bridge converter, and for this reason it is more capable for handling higher power levels. Although the voltage stress for the switches is the same as that in the half-bridge converter, the switch current rating can be half of that in a half-bridge coverter for the same power.

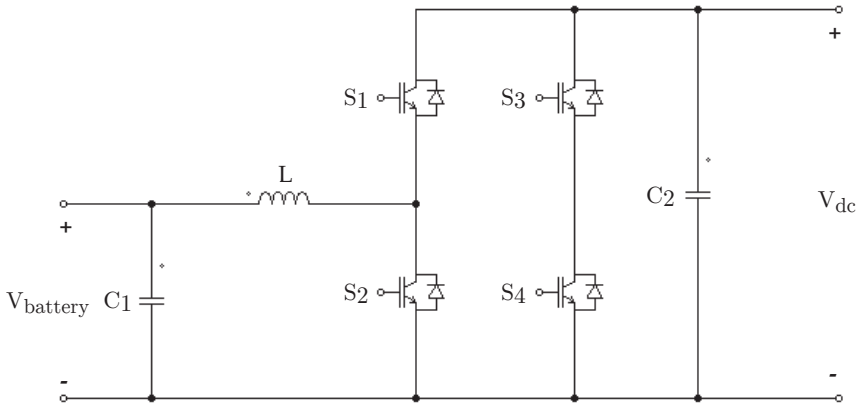

Figure 5.5: Full-bridge converter

Three-Level Converter

A neutral point clamped three-level converter proposed in [69] is shown in Figure 5.6. This topology has been characterized by [69] to have low switch voltage stress and smaller inductor rating.

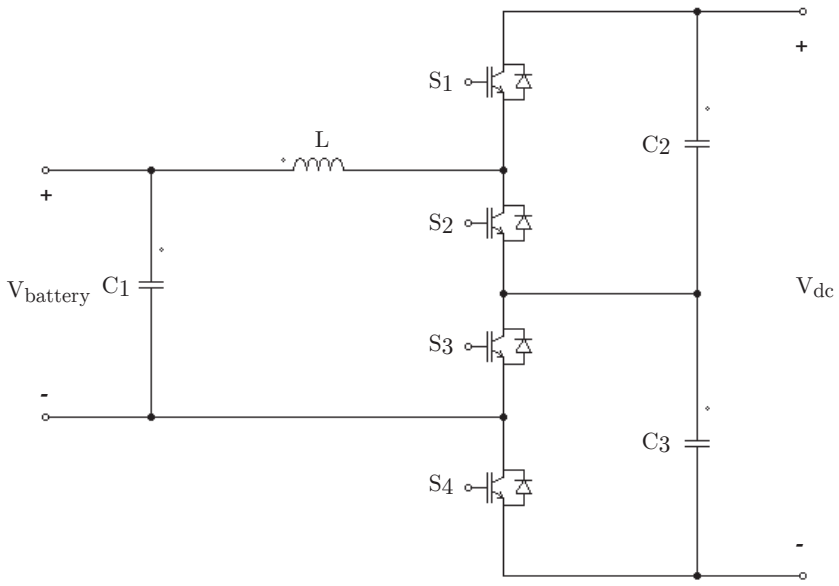

Figure 5.6: Neutral point clamped three-level DC-DC converter

The effective duty ratio in buck mode for this three-level converter is given as [69]:

$$d_{eff} = \frac{2 \cdot V_1}{V_2} \tag{5.3}$$

The inductor size for the three-level converter based on the specifications is calculated using the following design equation [69].

$$L = \frac{V_2 \cdot d \cdot (1 - 2d)}{\Delta I_L \cdot (2 f_s)} \qquad \text{where } d = \frac{V_{battery}}{V_{dc}} \tag{5.4}$$

$$L = \frac{700 \cdot 0.4286 \cdot (1 - (2 \cdot 0.4286)}{5 \cdot 2 \cdot 20000} = 0.214mH$$

The inductor rating required for the three-level converter is half the size needed for the half-bridge, bidirectional buck-boost or the full-bridge converter. However, this topology restricts that the dc-link voltage must be at least twice the battery pack voltage. Also, the voltage stress of each switch is $\frac{1}{2}V_2$.

5.1.2 Topology Analysis

The half-bridge converter has been found by [68] to have more advantages over bidirectional Ćuk and SEPIC/Luo convertesr as a power management interface in vehicular applications. Therefore, the Ćuk and SEPIC/Luo converter can be taken out of consideration for the battery charger.

The neutral point clamped three-level converter has an inductor size that is one-half of that in the half-bridge and bidirectional buck-boost converters. This is a very attractive benefit for an on-board battery charger, but this topology has a constraint that the dc-link voltage must be at least twice the battery pack voltage. This implies that if the three-level converter is chosen, then the dc-link voltage in the charger must be at least 600V. This potentially poses a serious safety hazard for the plugin vehicle, and also increases the voltage rating of switches in the AC-DC converter. For these reasons, the neutral point clamped three-level converter is not an ideal candidate for the battery charger.

The half-bridge converter and the bidirectional buck-boost converter have very similar characteristics in terms of their inductor sizes, voltage stress for the switches and component counts, since the bidirectional buck-boost converter topology is based on the half-bridge converter. Although the bidirectional buck-boost converter is not as widely used compared to the half-bridge converter, its simple structure and a performance almost identical to that of the half-bridge converter make it worth investigating for battery charger applications.

In comparison with half-bridge converter and bidirectional buck-boost converter, the full-bridge converter can handle higher power transactions and has higher controllability due to the increase in the number of controllable switches. Because the full-bridge converter can produce an effective switching frequency twice of the actual switching frequency if unipolar PWM switching method is employed, the ratings of the inductor and capacitor can be potentially less than the inductor and capacitor size used in other two converters. The full-bridge converter can be a suitable DC-DC converter for an on-board battery charger if the weight reduction from the inductor and capacitor is greater than the weight increase introduced by the two additional IGBTs.

5.1.3 Control Technique

The bidirectional DC-DC converter is controlled by two separate control loops. One control loop is dedicated for current control during constant-current (CC) charging and discharging. The other control loop is responsible for voltage control during constant-voltage (CV) charging. Since all control quantities for a DC-DC converter are time invariant at steady-state, using a linear PI controller is an ideal way for keeping the controller design simple.

The structures of the current and voltage controllers are identical. The desired quantity is subtracted by the actual quantity to obtain an error difference. This error is amplified by a PI controller, which is then compared with a triangular waveform. The intersections of the control signal and the triangular waveform produce the modulating signals for the controllable switches. A block diagram of the described controller is shown in Figure 5.7.

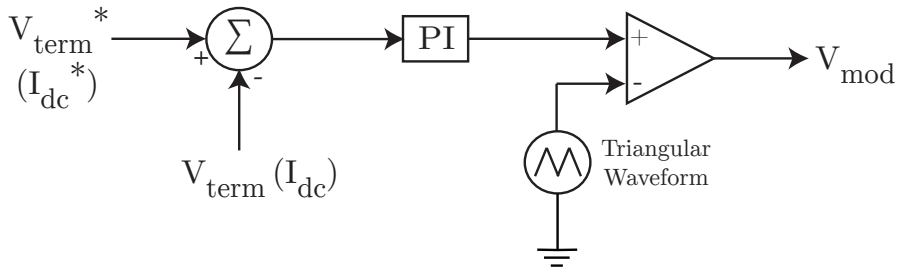

Figure 5.7: Block diagram of DC-DC converter voltage/current controller

5.2 Simulation Results of Battery Charger

In this section, the simulation results of the two proposed battery charger designs are provided. The two proposed battery charger designs are: 1) full-bridge AC-DC converter + bidirectional buck-boost DC-DC converter, and 2) full-bridge AC-DC converter + full-bridge DC-DC converter. The performance of each battery charger design is evaluated for three modes of operation, i.e., CC charging, CV charging and CC discharging. The transition from CC charging scheme to CV charging scheme is dependent on the %SOC of the battery pack. Since the single-variable functions for the extracted battery cell's parameters are defined up to 90% SOC only, the triggering point for transitioning from CC charging to CV charging is set at 85% SOC. When the %SOC of the battery pack is

below 85% and the battery charger is operating in charging mode, the default charging scheme is CC charging. When the %SOC of the battery pack is above 85% and the battery charger is also operating in charging mode, CV charging scheme is used. In both battery charger designs, a $0.5mH$ dc inductor is used on the battery-side; this inductance size is based on the values calculated in this chapter. Furthermore, a $1mF$ capacitor is used across the battery pack's terminals to provide sufficient filtering. The 300V, 16kWH battery pack is formulated using equations (3.12) to (3.17), and the equation-based electrical circuit battery model, shown in Figure 3.4, is used to model the behaviour of the battery pack.

5.2.1 Bidirectional Battery Charger: Full-bridge AC-DC + Bidirectional Buck-Boost DC-DC

In the first simulation case, the bidirectional battery charger is constructed based on a full-bridge AC-DC converter and a bidirectional buck-boost DC-DC converter. Simulation results for this battery charger configuration are shown in Figures 5.8 and 5.12.

In Figure 5.8, the top plot shows the grid voltage at $240V_{rms}$ and the sinusoidal current at the grid interface at unity power factor. The bottom plot shows the dc-link voltage, fluctuating between $320V$ to $380V$.

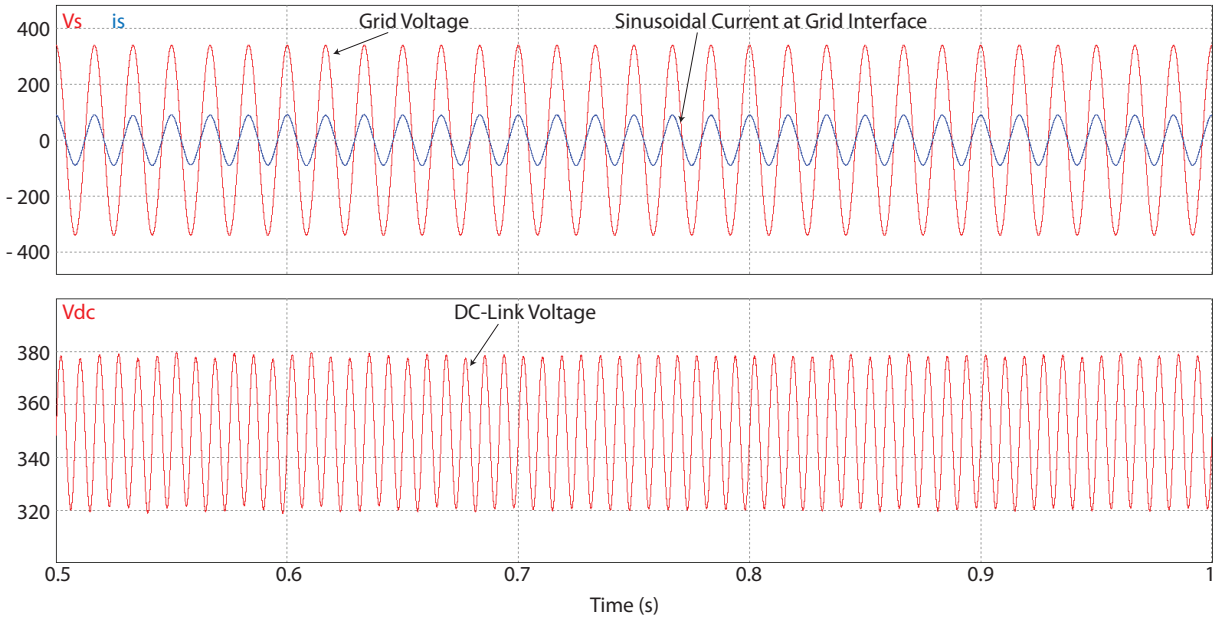

Figure 5.8: Simulation results for full-bridge AC-DC + bidirectional buck-boost DC-DC at unity power factor. Top: grid voltage and sinusoidal current (THD=4%). Bottom: dc-link voltage.

In Figure 5.9, V2G power transactions are realized. The sinusoidal current is 180° out of phase with the grid voltage, indicating the reverse flow of active power. The dc-link voltage is also fluctuating between $320V$ to $380V$.

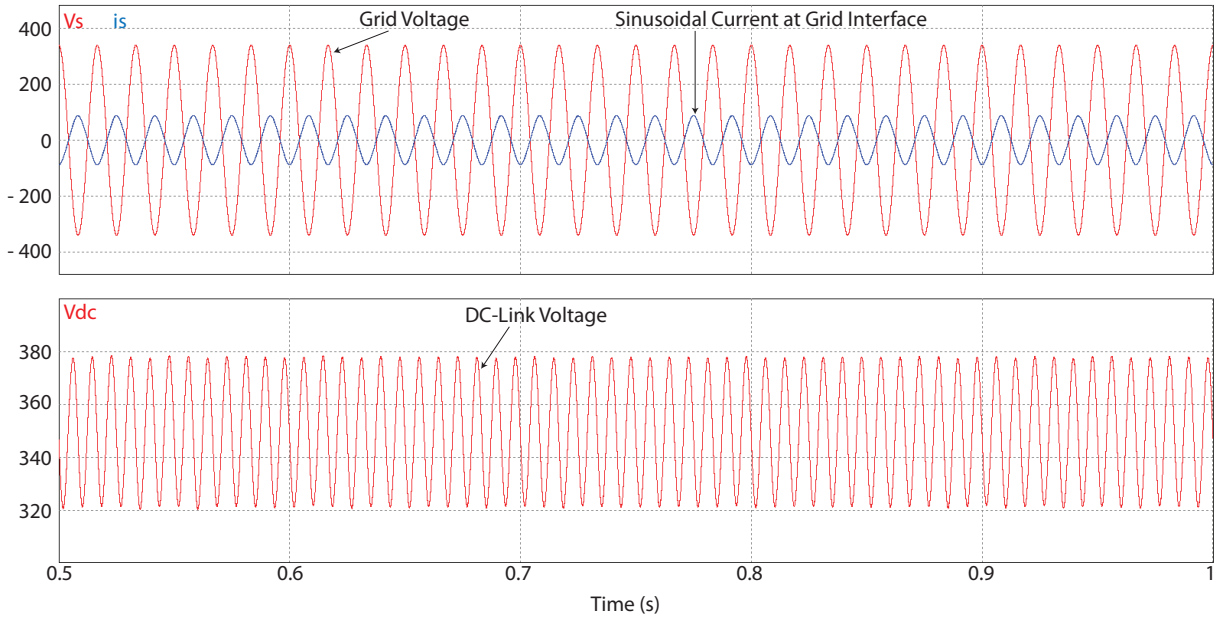

Figure 5.9: Simulation results for full-bridge AC-DC + bidirectional buck-boost DC-DC at CC discharging. Top: grid voltage and sinusoidal current (THD=3.3%). Bottom: dc-link voltage.

Figures 5.10 to 5.12 shows waveforms for three different operating modes. The first segments in these waveforms display results for CC charging, the middle segment show results for CV charging, and the last segment is when the battery charger operates in CC discharging mode.

The top plot in Figure 5.10 displays the grid voltage and the sinusoidal current at the grid interface. In CC charging mode, the battery pack is charged at $50A$. In CC discharging mode, the battery pack is sending power back grid at a current level of $50A$. It can be observed that the charging current has decreased when the battery charger is operating in CV charging mode. The bottom plot shows the dc-link voltage. In CC charging and CC discharging, the voltage ripple at the dc-link is 17%, and in CV charging, the voltage ripple is 5.7%. This is due to the fact that there is a larger amount of current flowing through the dc-link in CC charging and CC discharging modes, and it is reflected on the dc-link.

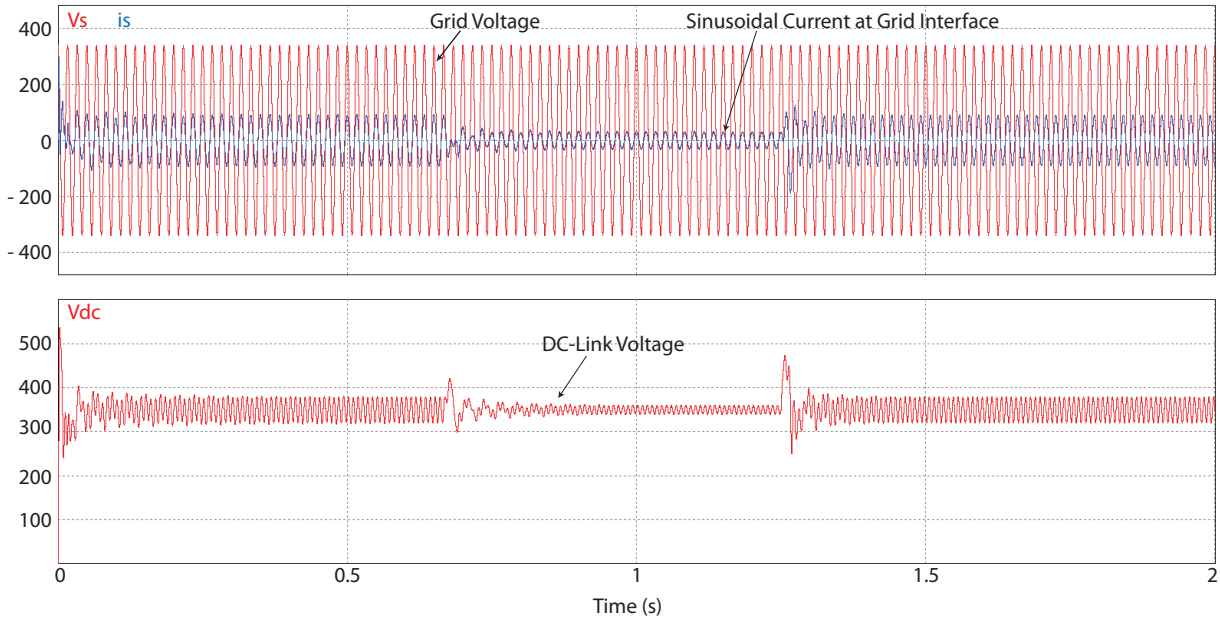

Figure 5.10: Simulation results for full-bridge AC-DC + bidirectional buck-boost DC-DC. Top: grid voltage and sinusoidal current. Bottom: dc-link voltage.

In Figure 5.11, the dc inductor current is shown in the top plot. A maximum 14% peak-to-peak current ripple can be observed in CC charging and CC discharging. The peak-to-peak current ripple observed in CV charging is 69%. This large current ripple can be attributed to the small charging current. The battery's terminal voltage and open circuit voltage are shown in the bottom plot. During CV charging, the desired terminal voltage of the battery pack is set at $301V$, and thus it can be observed that the voltage difference between the terminal voltage and the open circuit voltage becomes smaller, causing a smaller amount of current to flow into the battery pack.

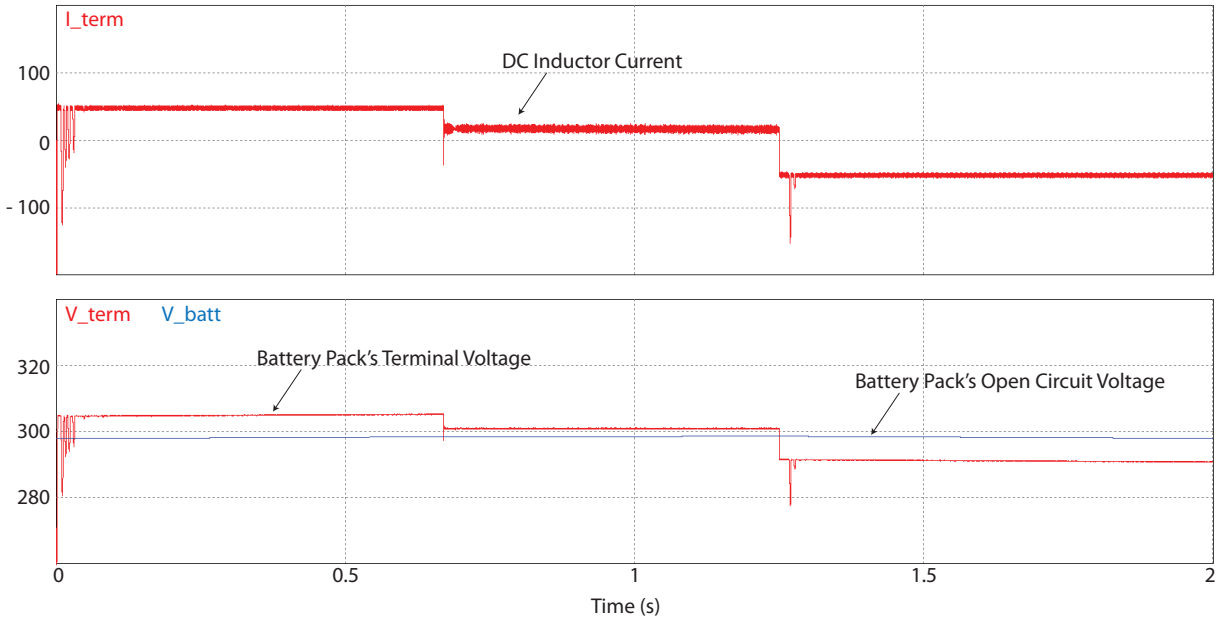

Figure 5.11: Simulation results for full-bridge AC-DC + bidirectional buck-boost DC-DC. Top: dc current measured at the inductor on battery-side. Bottom: battery pack's terminal voltage and open circuit voltage.

In Figure 5.12, the top plot displays the %SOC of the battery pack. Due to the smaller amount of charging current in CV charging scheme, the rate of change of %SOC in the battery pack is smaller in CV charging than in CC charging. Lastly, the bottom plots shows the grid voltage and the orthogonal fictitious signal needed for DQ transformation.

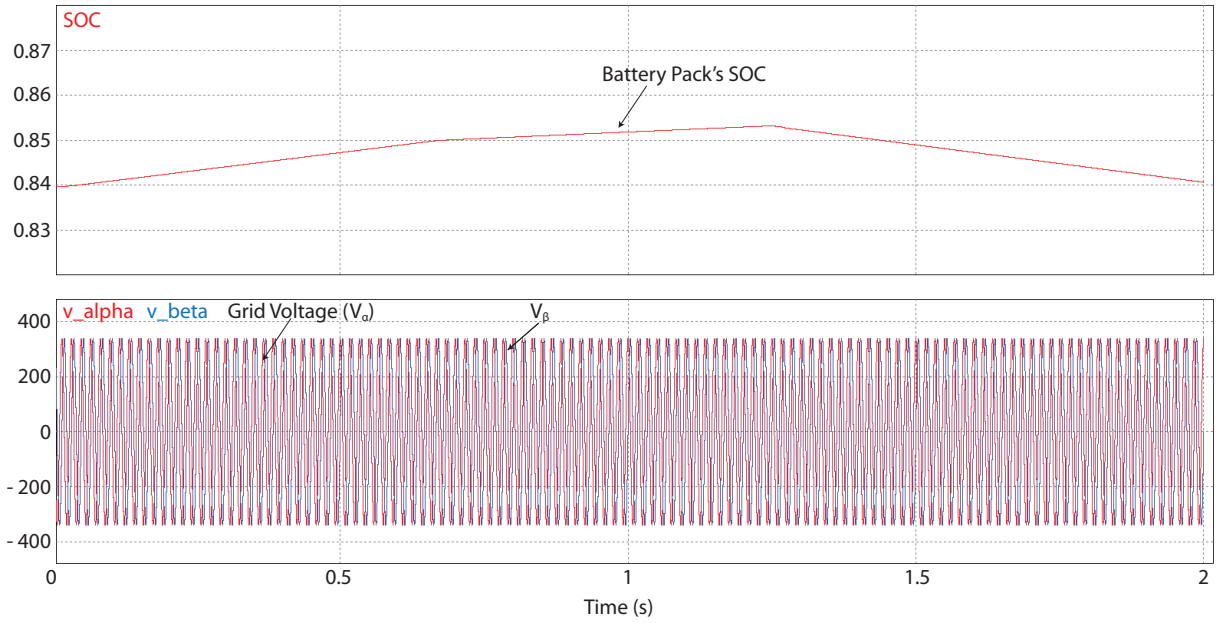

Figure 5.12: Simulation results for full-bridge AC-DC + bidirectional buck-boost DC-DC. Top: battery pack's SOC. Bottom: V_α and V_β.

5.2.2 Bidirectional Battery Charger: Full-Bridge AC-DC + Full-Bridge DC-DC

A second bidirectional battery charger configuration using a full-bridge AC-DC converter and a full-bridge DC-DC converter is simulated. Simulation results for this charger configuration are shown in Figures 5.13 and 5.17.

Similar to the previous case, the top plot of Figure 5.13 shows the grid voltage at $240V_{rms}$ and the sinusoidal current at the grid interface at unity power factor. The bottom plot shows the dc-link voltage fluctuating between $320V$ and $380V$.

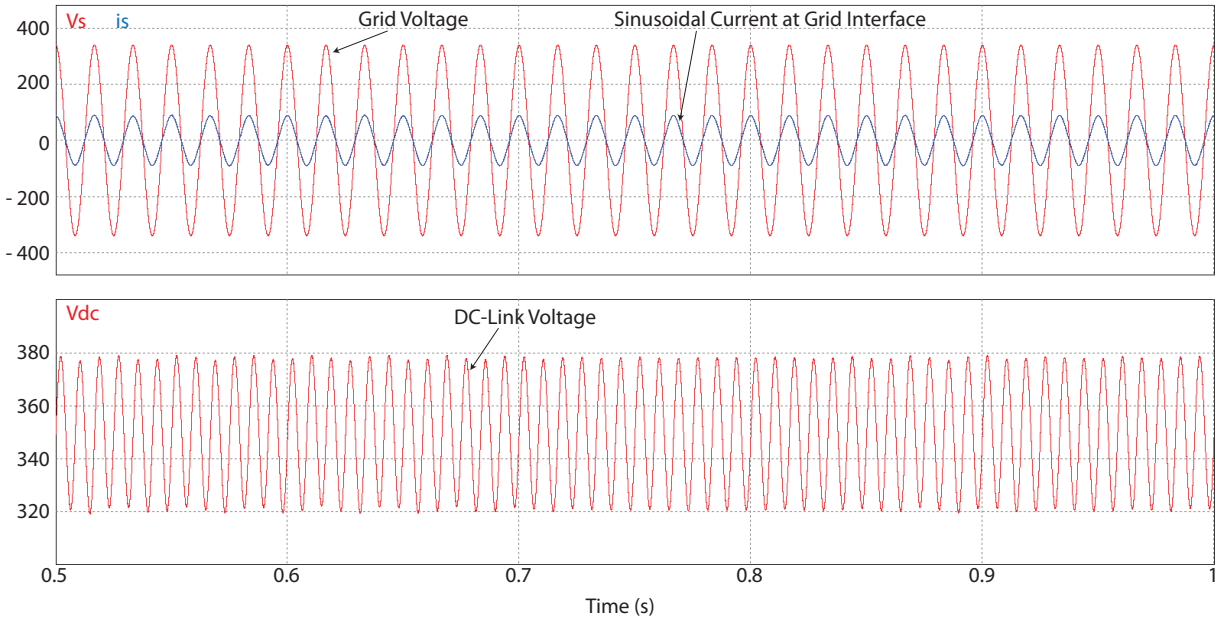

Figure 5.13: Simulation results for full-bridge AC-DC + full-bridge DC-DC at unity power factor. Top: grid voltage and sinusoidal current (THD=4.1%). Bottom: dc-link voltage.

V2G power transfer is realized in Figure 5.9. The sinusoidal current is 180° out of phase with the grid voltage, indicating that the active power flows from the battery pack towards the utility grid. The dc-link voltage is shown in the bottom plot, fluctuating between $320V$ and $380V$.

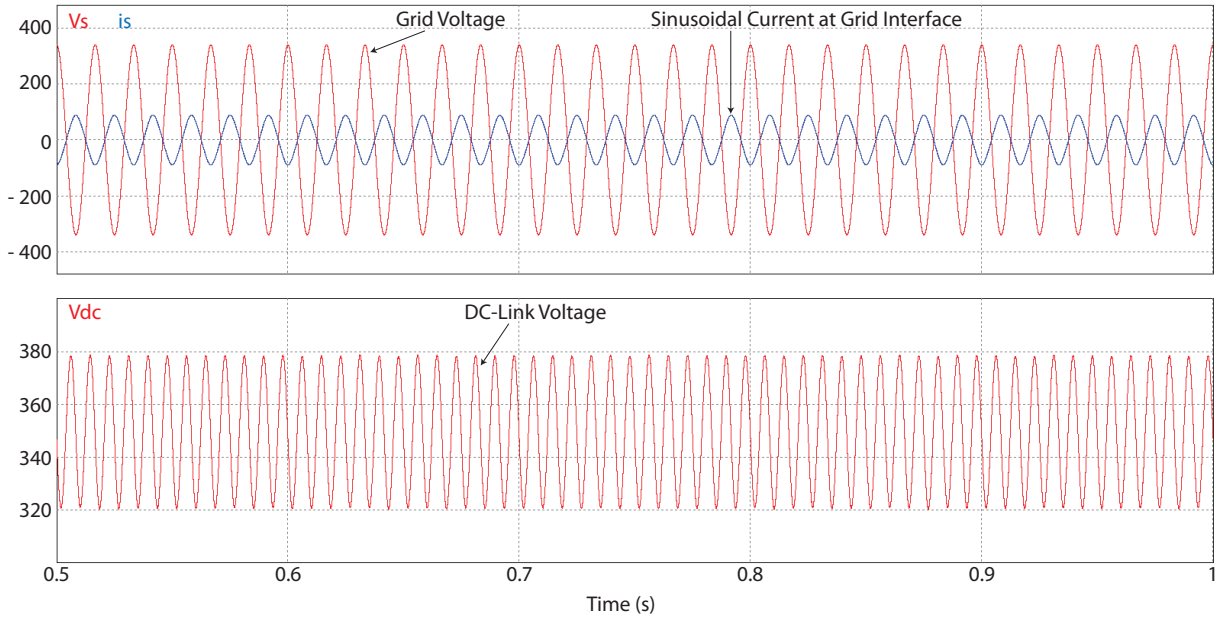

Figure 5.14: Simulation results for full-bridge AC-DC + full-bridge DC-DC at CC discharging. Top: grid voltage and sinusoidal current (THD=3.2%). Bottom: dc-link voltage.

Figures 5.15 to 5.17 shows waveforms for three different operating modes. Similar to previous figures, the first segment shows results for CC charging. The middle segment is when the battery charger operates in CV charging. The last segments in these waveforms show results for CC discharging.

The top plot in Figure 5.15 displays the grid voltage and the sinusoidal current at the grid interface. The battery pack is charging at $50A$ in CC charging mode, while in CC discharging mode, the battery pack is sending power back grid at a current level of $50A$. The bottom plot shows the dc-link voltage. In CC charging and CC discharging, the voltage ripple at the dc-link is 17%, and in CV charging, the voltage ripple is 8.6%, which is slightly higher than previous charger configuration. However, there is less overshoot in the dc-link voltage when transiting from CC charging to CV charging.

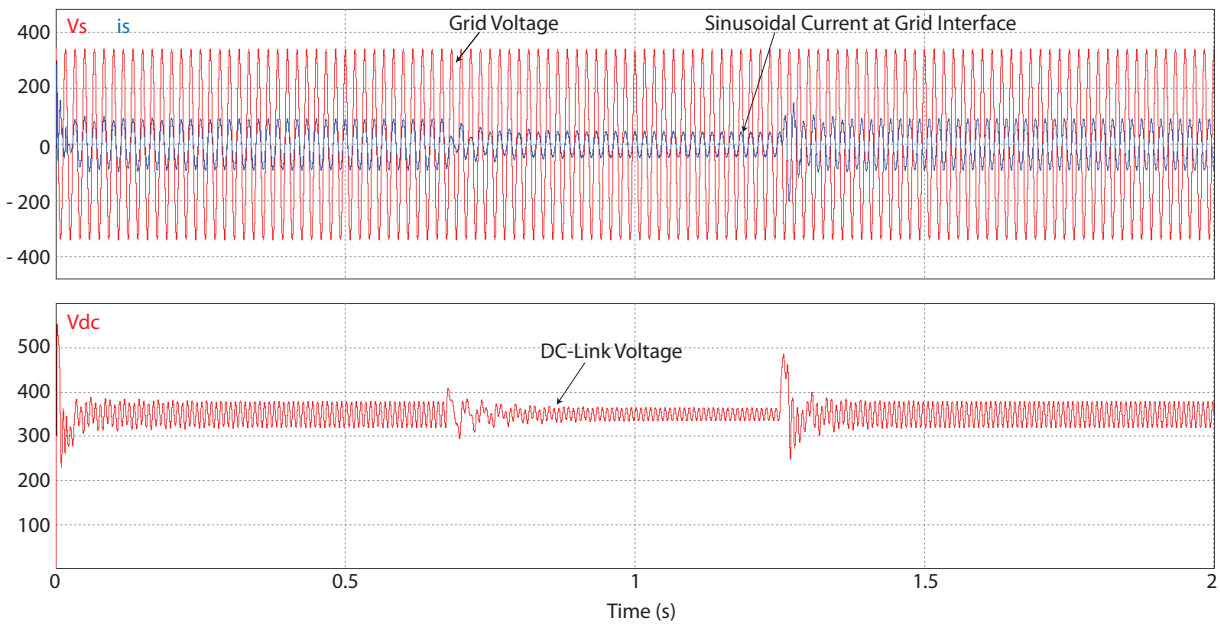

Figure 5.15: Simulation results for full-bridge AC-DC + full-bridge DC-DC. Top: grid voltage and sinusoidal current. Bottom: dc-link voltage.

Figure 5.11 displays the dc inductor current in the top plot. The maximum peak-to-peak current ripple observed in CC charging, CV charging and CC discharging are 12%, 23% and 8%, respectively. In comparison to previous charger configuration which uses a bidirectional buck-boost DC-DC converter, this charger configuration can achieve lower current ripple, and most noticeably observed in CV charging. The bottom plot shows the battery pack's terminal voltage and open circuit voltage.

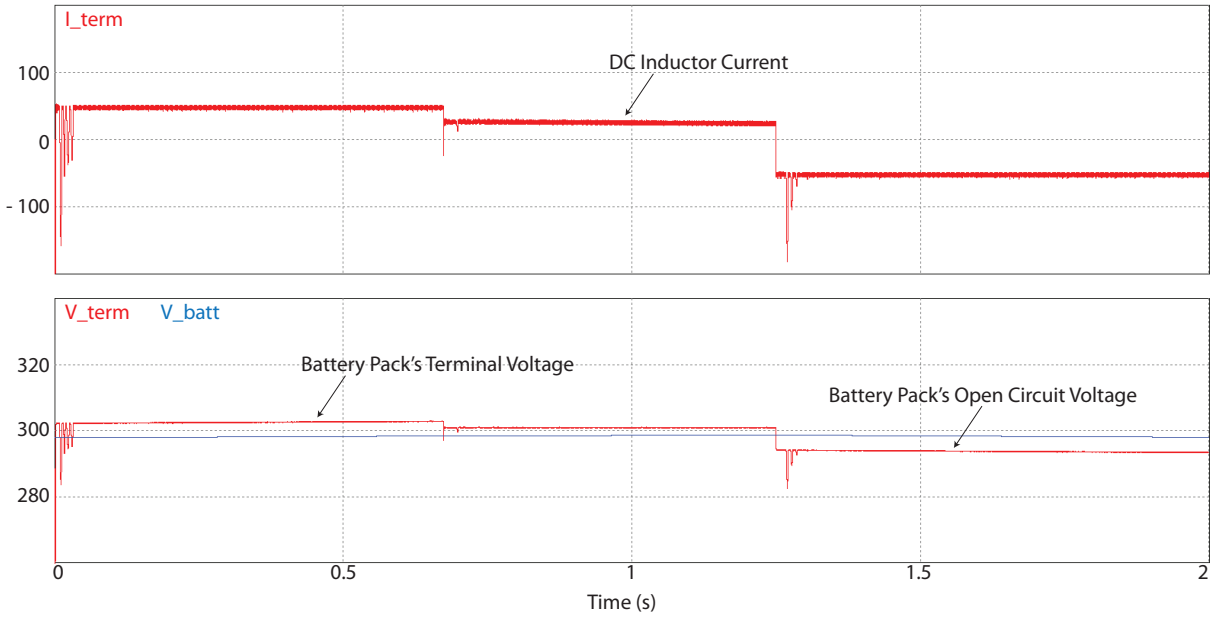

Figure 5.16: Simulation results for full-bridge AC-DC + full-bridge DC-DC. Top: dc current measured at the inductor on battery-side. Bottom: battery pack's terminal voltage and open circuit voltage.

Lastly, the %SOC of the battery pack, and the grid voltage and its orthogonal fictitious signal are shown in Figure 5.12.

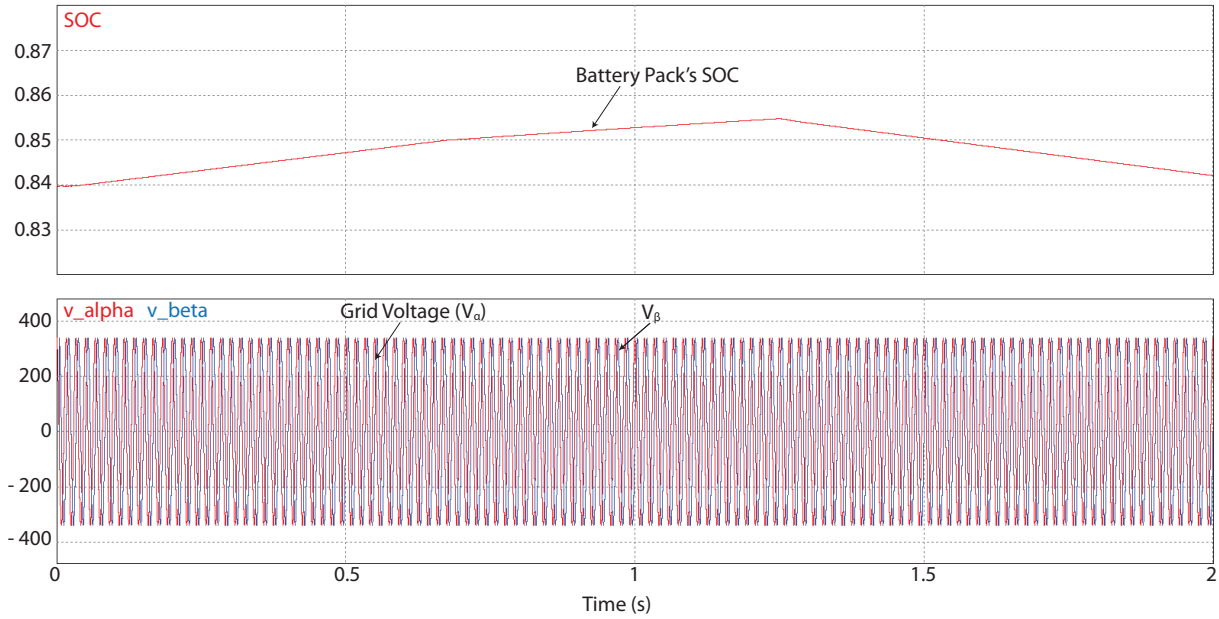

Figure 5.17: Simulation results for full-bridge AC-DC + full-bridge DC-DC. Top: battery pack's SOC. Bottom: V_α and V_β.

5.2.3 Analysis

The simulation results for the two proposed bidirectional battery chargers demonstrate their abilities to charge the battery pack in CC and CV charging modes, and their abilities to perform V2G power transfer. The full-bridge + bidirectional buck-boost configuration has the advantages of having lower voltage ripples at the dc-link and using fewer controllable switches. From the dc inductor current results for buck-boost and full-bridge converters, it can be seen that the current ripple in the latter case is smaller. This is due to the fact that in full-bridge converter under unipolar voltage switching, the effective switching frequency observed at the output terminals is two times the actual switching frequency. However, full-bridge converter has four switches making the switching losses two times that of buck-boost converter which has only two switches. The final decision on the topology type needs to be done based on a case study.

Chapter 6

Experimental Results of Full-Bridge DC-DC Converter Prototype

One important milestone in developing the bidirectional battery charger is to construct a lab prototype to verify the charger performance by comparing simulation results with the experimental results. Due to time constraint, only a full-bridge DC-DC converter was implemented based on the analysis and designed presented in Chapter **??**. This chapter presents experimental results along with a cost analysis for the prototype. The discussion in sensing circuit design, hardware component selection and ADC calibration is presented in Appendix B

The lab prototype is intended to demonstrate bidirectional power flow capability between the DC-link and the battery, as well as to demonstrate constant-current (CC) and constant-voltage (CV) charging schemes at low power levels.

6.1 Experimental Results

The completed lab prototype of the full-bridge DC-DC converter is shown in Figures 6.1 and 6.2. Testing of the lab prototype was performed in two stages. The first stage of the testing utilized a controllable source and a controllable load to perform initial PI tuning, to ensure the sensing circuits' feedbacks are accurate, and to verify the constant-current constant-voltage (CCCV) charging scheme is functioning. The second stage of the testing

used lead-acid batteries to demonstrate bidirectional power flow between the two terminals of the converter. This section discusses the performance of the lab prototype, and factors that might have negatively affected the performance.

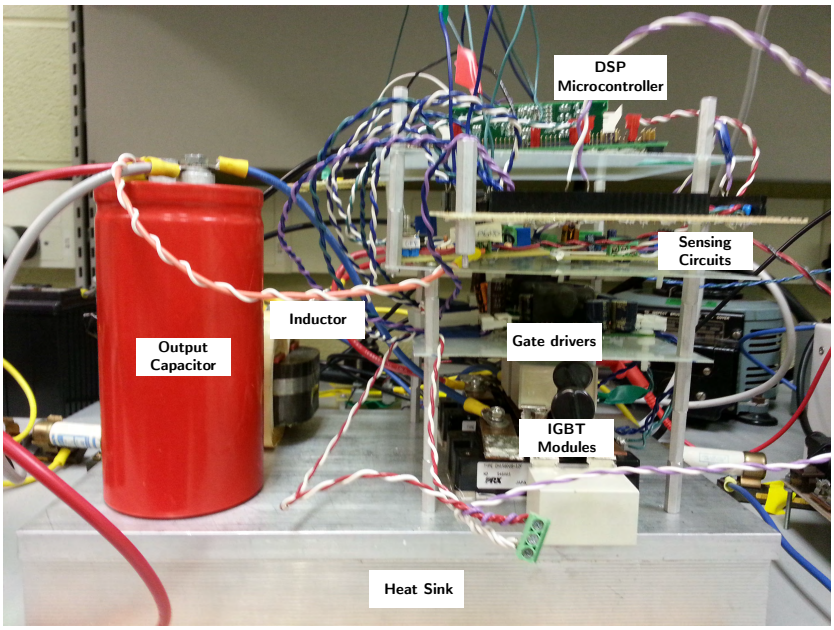

Figure 6.1: Front view of the lab prototype

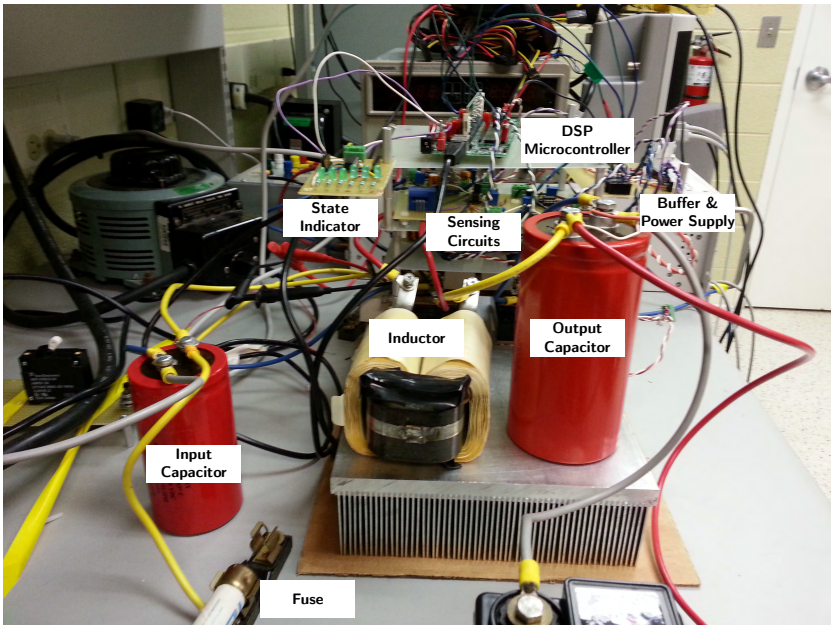

Figure 6.2: Side view of the lab prototype

6.1.1 Constant Resistive Load

In the first round of testing, a constant resistive load was used instead of the battery pack. In addition, a controllable DC source, set at 40V, was utilized as the dc-link voltage source for the converter instead of using battery pack because the controllable DC source has the capability to control the current limit, which is desirable for initial PI tuning. Figure 6.3 shows the arrangement of the controllable DC source and the resistive load with the full-bridge DC-DC converter.

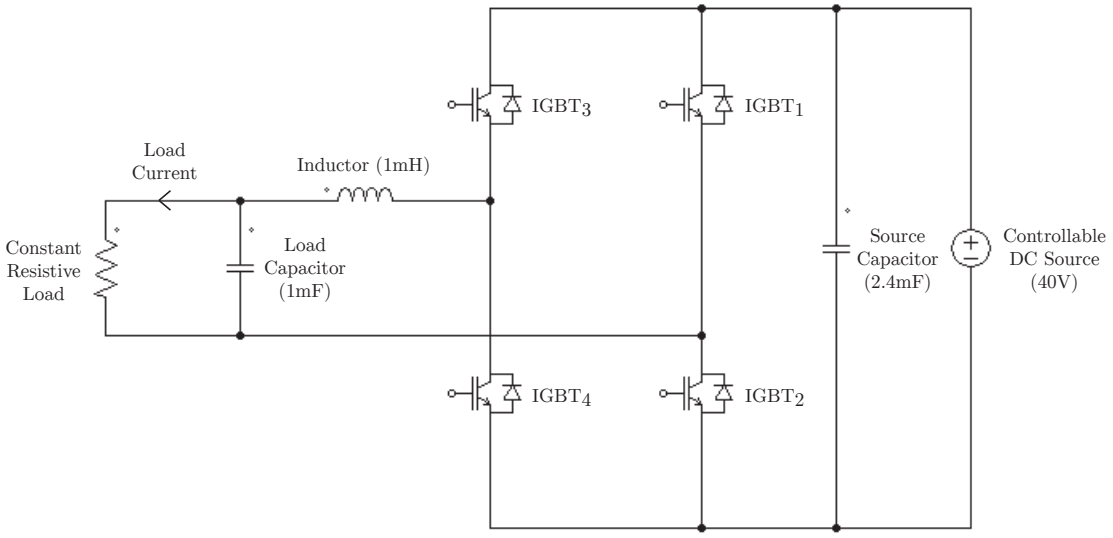

Figure 6.3: Circuit diagram of full-bridge DC-DC converter connected with resistive load

Figure 6.4 shows the PWM signal output from DSP and the IGBT gating signal for the same IGBT switch. The successful control and operation of the IGBT can be realized when the PWM signal and the gate drive switching signal both display identical duty ratio, and that the PWM signal swings from 0 to 3V and the gate drive signal swings from -8V to 15V. The smooth edges in the gate drive switching signal were caused by the charging and discharging actions of the IGBT gate capacitor.

To avoid inrush current from the controllable source when the converter is activated, the output capacitor was precharged to 13V by operating the converter at a fixed duty ratio before transitioning to charging mode. Figure 6.5 shows the capacitor voltage waveform when the capacitor was precharged.

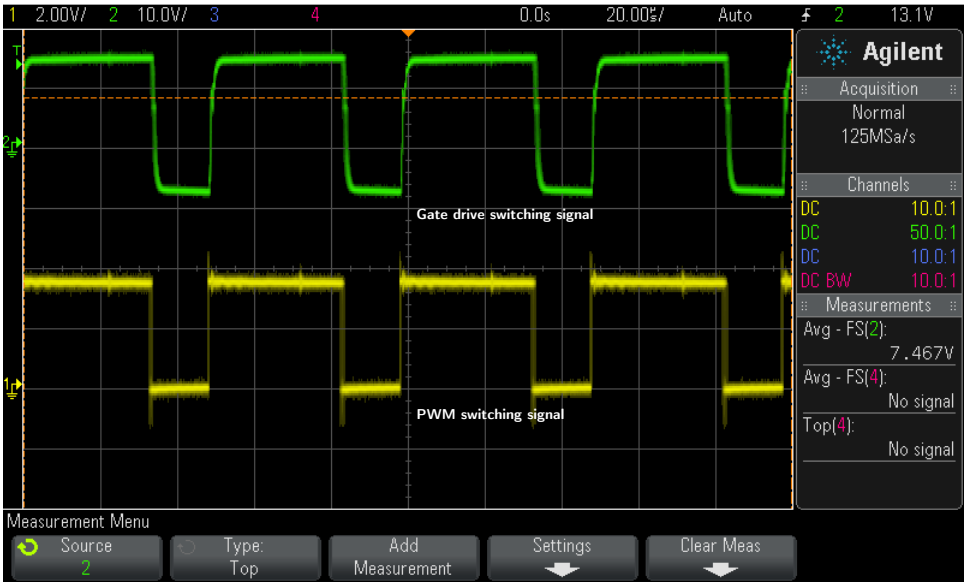

Figure 6.4: PWM and gate drive switching signals

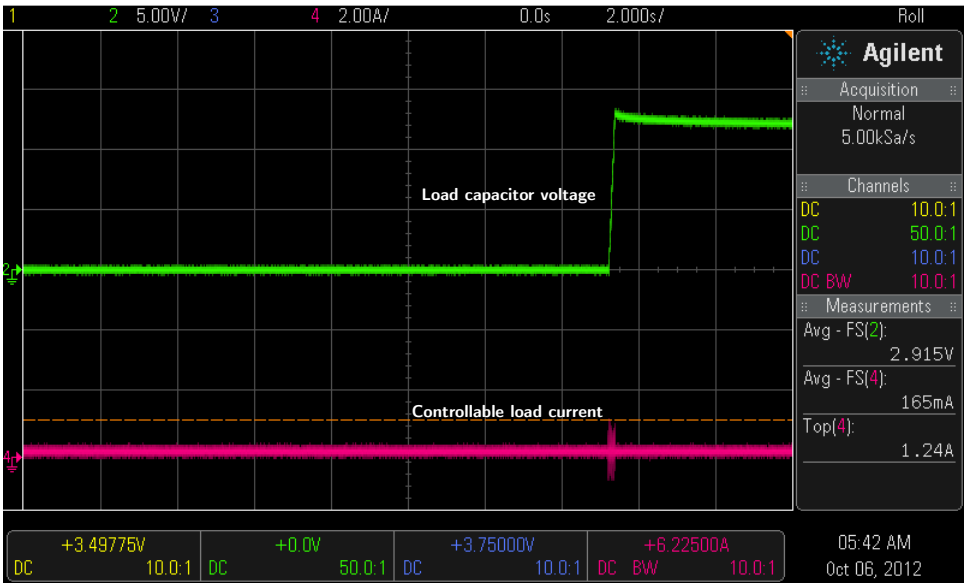

Figure 6.5: Precharging the load capacitor

After precharging the capacitor, the converter was controlled to feed a 6Ω constant

resistive load using CC-CV scheme. Figures 6.6 to 6.9 shows the voltage and current waveforms when the converter was operating in different modes and/or transitioning between different modes. Figure 6.6 displays the load-side capacitor voltage and current when the converter was controlled to charge the load-capacitor using CC scheme at 4A. The waveforms in Figure 6.7 show the transition from CC to CV charging, where the target load voltage was set at 20V. Figure 6.8 continues to display CV scheme but also presents the short transient effect on the load capacitor voltage when the resistive load was disconnected from the converter while maintaining the target voltage at the load capacitor. Lastly, Figure 6.9 shows the discharge of the load capacitor after the converter shutdown.

It can be seen that the lab prototype can produce clean waveforms during steady-state operation and can achieve smooth transitions between different operating modes when feeding a constant resistance load.

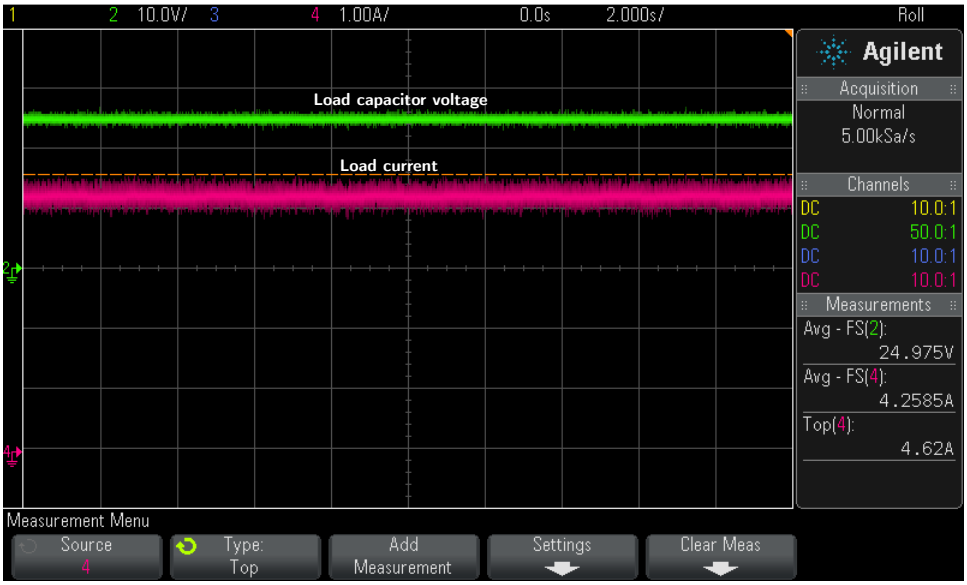

Figure 6.6: Constant-current charging for a constant resistive load

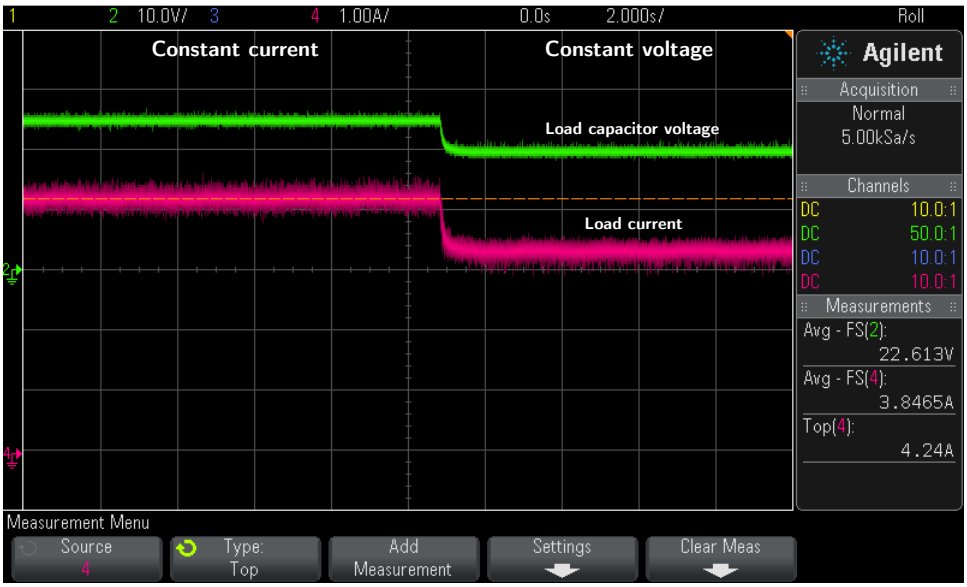

Figure 6.7: Constant-current constant-voltage charging transition

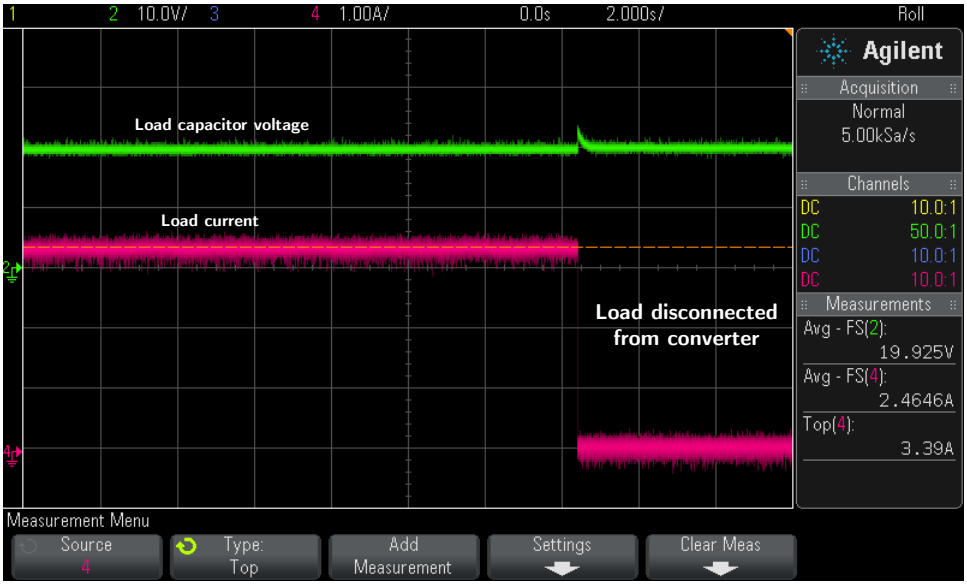

Figure 6.8: Constant-voltage feedback when load was disconnected from converter

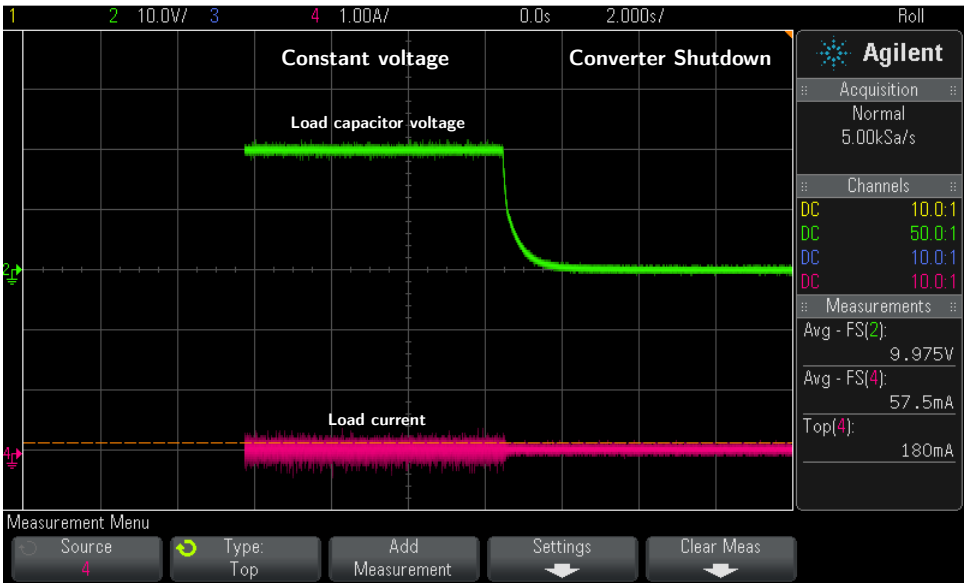

Figure 6.9: Shutting down the converter

6.1.2 Bidirectional Power Flow

To demonstrate the prototype's ability to perform bidirectional power flow, lead-acid batteries were placed at both terminals of the prototype to act as both energy storage and energy source, as shown in Figure 6.10. Two lead-acid batteries connected in series were placed on the DC-link terminal and one lead-battery was used to represent the battery pack to satisfy the requirement that it must be at a lower voltage level than the dc-link. Figure 6.11 shows the experimental setup. Refining the PI values in the control loops was necessary because these batteries have dynamic characteristics that require quicker response control loops.

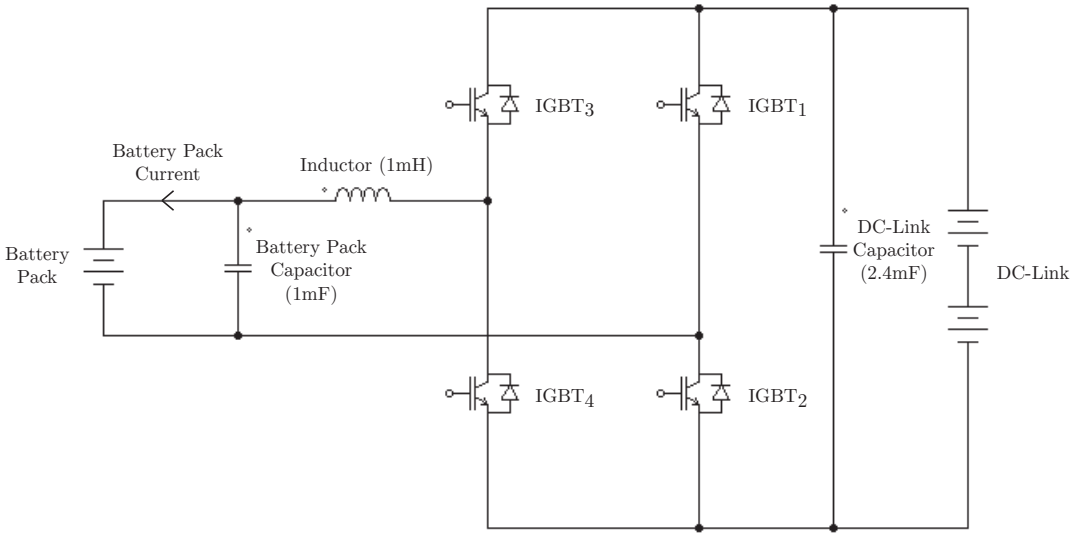

Figure 6.10: Circuit diagram of full-bridge DC-DC converter connected with battery packs

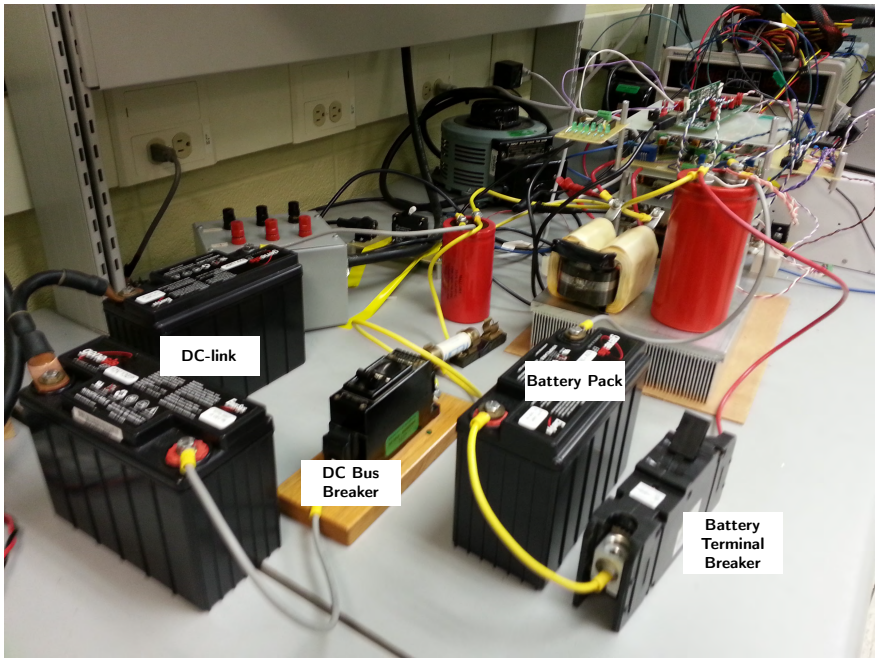

Figure 6.11: Experimental setup for demonstrating bidirectional power flow

Figures 6.12 to 6.15 show the converter performance in realizing bidirectional power flow. In Figure 6.12, the output capacitor was precharged to 13V after the converter was initiated to avoid inrush current, which resulted in battery pack's current to increase smoothly.

Figure 6.13 demonstrates the charging and discharging ability of the prototype and their transients. After precharging the capacitor, the converter charged the battery pack using CC charging scheme at 4A for 10 seconds before transitioning to discharging the battery pack at 2A for 10 seconds. Finally, the converter transitioned back to CC charging. Smooth current transients and small battery voltage fluctuations can be observed in between different modes of operation.

Figure 6.14 shows the performance of CV charging and the smooth transition between CC and CV modes. It also reveals that the CV control loop has a better error tracking than the one in CC.

The last waveform (Figure 6.15) incorporates all the operation modes of the converter. It began by precharging the capacitor, followed by bidirectional power flow, then moved onto CV charging, and ended by shutting down the converter.

Overall, the experimental results from the lab prototype prove that the chosen topology and control techniques developed in Chapter **??** can achieve bidirectional power flow and can charge the battery using CC or CV charging scheme.

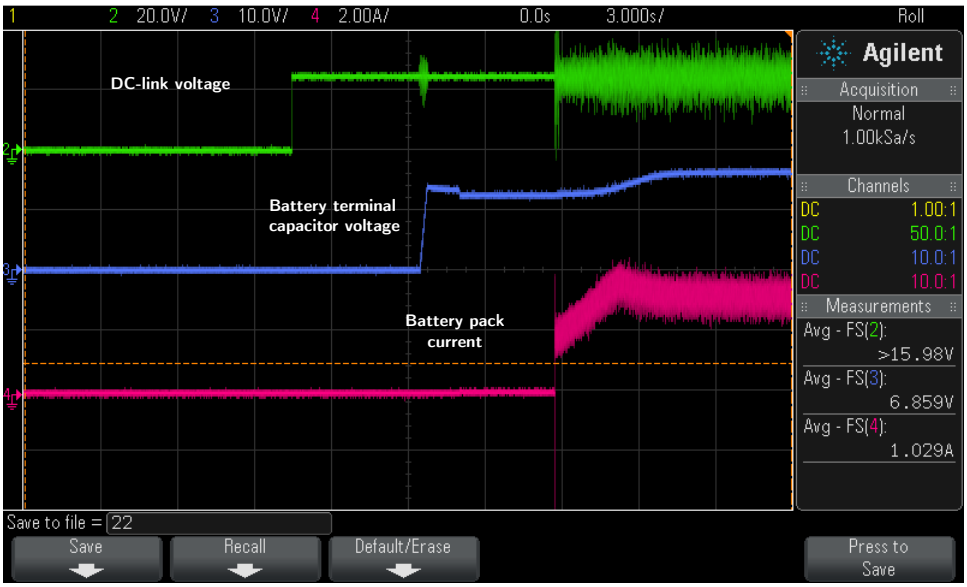

Figure 6.12: Precharging the capacitor

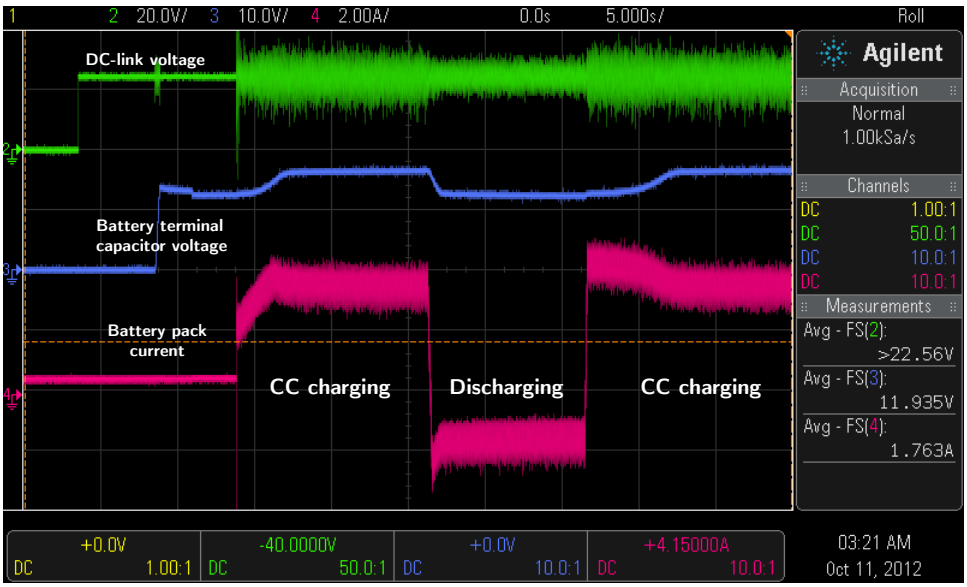

Figure 6.13: Bidirectional power flow

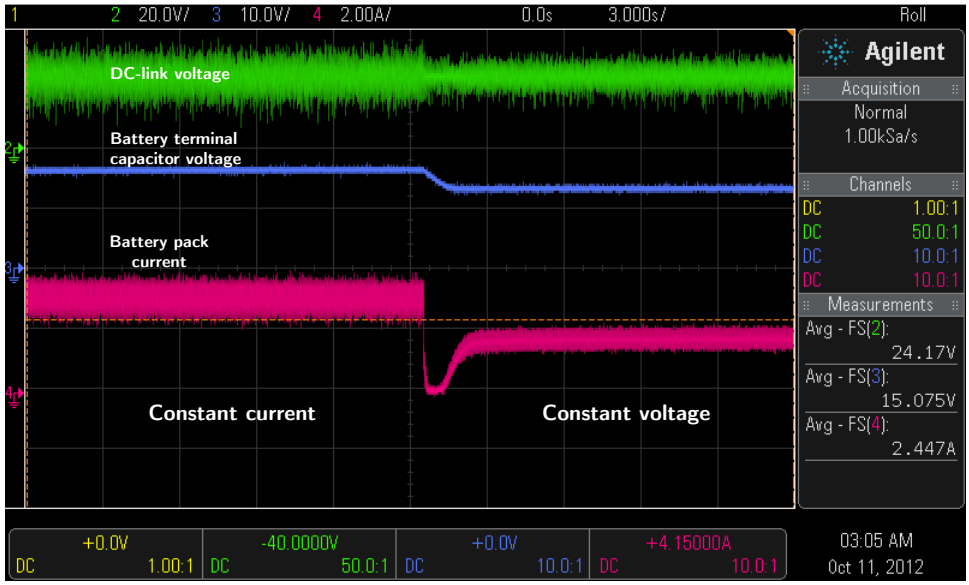

Figure 6.14: Constant-current constant-voltage charging transition

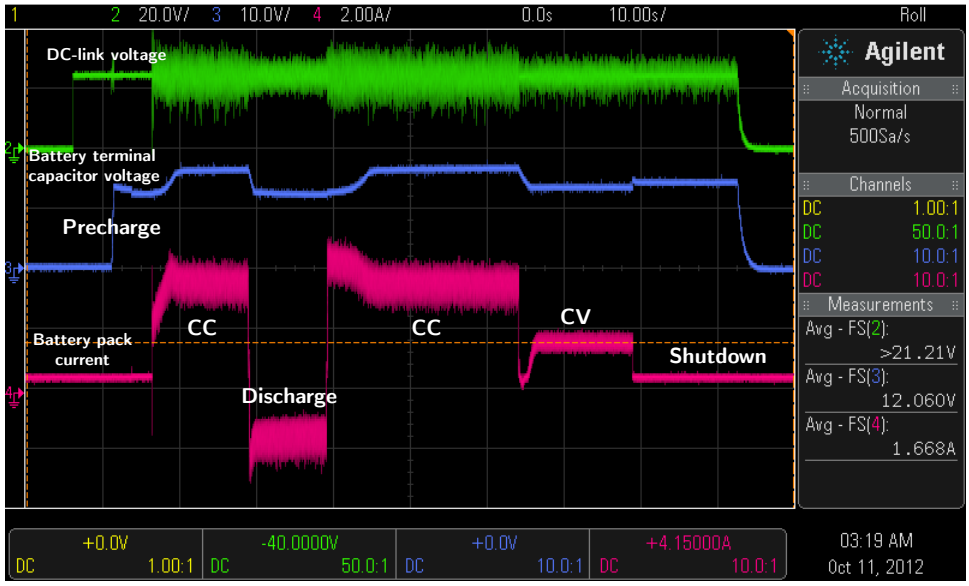

Figure 6.15: Waveform showing the different transitions

6.1.3 Efficiency

One important metric to evaluate the performance of a converter is efficiency. The efficiency of the lab prototype was considered for two cases: CC charging and CV charging.

Constant Current Charging

The following data was collected during constant-current charging. An efficiency of 74.64% was achieved in this charging scheme.

DC-link voltage = $24.5V$
DC-link current = $2.8A$
Battery erminal voltage = $16V$
Battery current = $3.2A$

$$\text{Efficiency}_{CC} = \frac{(16) \cdot (3.2)}{(24.5) \cdot (2.8)} = 74.64\% \tag{6.1}$$

Constant Voltage Charging

The following data was collected during constant-voltage charging. In this charging scheme, an efficiency of 73.46% was achieved.

DC-link voltage = $24.5V$
DC-link current = $1.2A$
Battery terminal voltage = $13.5V$
Battery current = $1.6A$

$$\text{Efficiency}_{CV} = \frac{(13.5) \cdot (1.6)}{(24.5) \cdot (1.2)} = 73.46\% \tag{6.2}$$

Efficiency Analysis

The efficiency of the converter is slightly lower in CV mode compared that in CC mode. This slight difference in the calculated efficiencies could be a result of data collection errors due to the ripples in the waveforms. There are many factors that can negatively affect the efficiency of the converter but one notable contributor that can degrade the efficiency is noise.

This prototype exhibited poor performance when operating at a current levels under $1A$ or at a voltage level under $10V$, and this was mainly caused by the low signal-to-noise (SNR) ratio. At such low current and voltage levels, the sensing circuits are incapable of tracking the values due to high level of noise pollution, and thus causing the control loops to response inaccurately and create high ripples. These ripples were most apparent in the charging current waveforms. However, when operating at a higher power level, the SNR becomes larger and the feedback values become more accurate, and consequently the control loops can operate more effectively.

Methods that were used to reduce noise in the prototype included placing capacitors at every power supply and at every IC between its supply pin and ground pin, using wires that were as short as possible, and creating signal pair, where each signal wire was always paired with a ground wire and they were twisted together. All the mentioned methods attempted to reduce the noise developed by ground loops.

More efforts must be made for noise reduction in order to improve the efficiency of the lab prototype. One considerable future work is to fabricate the sensing circuits and gate drive circuits onto one multi-layer PCB to increase the surface area of the ground plane and to decrease the length of the path between components.

6.2 Cost Analysis

Table 6.1 lists the major components needed for the construction of the full-bridge converter and their respectively costs. The bill of material does not include the cost of heat sink, small filtering capacitors, prototyping boards and other small components used. A rough estimate of the total cost for the DC-DC converter was close to $1600 CAD. The cost of the inductor constitutes the largest portion of the total cost of the prototype. Although

the $1600 amount can be considered a small percentage in the overall price of a plug-in vehicle, the building cost of the converter is expected to be significantly lower in the actual manufacturing stage. The reason for this is that because the prices listed in Table 6.1 are retail prices, which are greatly marked up from the high-volume purchases prices. When manufacturing of the converter in high volume, these components would be purchased at a lower price due to the large quantity of acquisition.

Table 6.1: Build of material for full-bridge DC-DC converter

Component Description	**Quantity**	**Unit Cost (CAD)**	**Total Cost (CAD)**
IGBT Module (CM150DUS-12F)	2	95.25	190.50
Gate Drive Prototype Board (BG2C)	2	21.46	42.92
Gate Driver (VLA507)	4	5.14	20.56
DC-to-DC converter (VLA106-15242)	4	13.75	55.00
2.4mF Capacitor (EAP242X500X5R3PD)	1	211.64	211.64
1mF Capacitor (EAP102X500W4L3PH)	1	105.00	105.00
Current Transducer (CAS 15-NP)	1	23.60	23.60
TMS320F2808 DSP Experimenter Kit	1	101.72	101.72
1mH Inductor	1	700*	700
0.1μf Snubber Capacitors	4	10.06	40.24
390V MOV (ERZV20D391)	4	1.52	6.08
Analog Optocoupler (HCNR200)	2	4.39	8.78
Single Amplifier (AD8031)	3	3.63	10.89
Dual Amplifier (AD8032)	2	5.60	11.20
Total Cost			**1528.13**
*This is the estimated cost since the part had been purchased a while ago and available in the lab.			

The price of a $8kW$ commercially-available unidirectional EV charger costs $2289 CAD [70]. This EV charger provides a wide ac input voltage range from $85V$ to $265V$. It has a maximum nominal output voltage at $312V$ with a maximum output current at $22A$. It has been assumed that the components in this EV charger are purchased at high-volume prices. Consequently, the cost of a $15kW$ battery charger for plugin vehicle is expected

to be greater than $2289 in the actual manufacturing. For this reason, the cost to build a full-bridge DC-DC converter as part of a two-stage battery charger for plugin vehicle is affordable.

Chapter 7

Conclusions and Future Work

7.1 Summary of Contributions

Vehicle electrification is a promising technology for reducing fossil fuel dependency, increasing environmental friendliness due to low tailpipe emissions and having higher energy efficiency. On-board rechargeable battery packs in plugin hybrid electric vehicles (PHEVs) and electric vehicles (EVs) can be recharged by directly connecting to the utility grid using a plug. The concept of Vehicle-to-Grid (V2G) has gained interest because on-board batteries have many desirable benefits for utility grid support, including peaking shaving and reactive power compensation. To aid in the promotion of V2G, the research of this thesis has focused on the development of a bidirectional battery charger for plugin vehicles in order to provide a power electronic interface that allows bidirectional power transfer between the utility grid and the on-board batter pack. The following summarizes the main contributions of the thesis.

- A modified equivalent electrical circuit battery model to represent the transient and steady-state behaviour of battery cells.
- A technique to determine the equivalent impedance of a battery pack.
- A DQ controller for single-phase grid-connected AC-DC converter in a bidirectional battery charger.
- Novel two-stage level-two bidirectional on-board battery charger configurations.

7.2 Conclusions

In Chapter 2, an overview on the three classifications of charging levels was provided. A detailed literature review of exisiting bidirectional battery charger topologies was also presented. It was found that bidirectional battery chargers are classified as single-stage and two-stage topologies. Single-stage topologies are simple, but are limited to low power charging. Two-stage topologies are more widely employed due to their performance in high-voltage charging, but require a tradeoff in size and weight.

Chapter 3 presented the specifications of the proposed bidirectional battery, as well as provided insight into the equivalent electrical battery model. This model is effectively in capturing the transient and steady-state behaviours of Li-ion, NiMN and leac-acid batteries. It was found that the series resistor in the battery model controls the instantaneous rise/drop in the terminal voltage at the beginning of a recovery period. The two parallel RC networks in the battery model characterize the short-term and long-term transients of a battery cell. In addition, it was found that the open circuit voltage of a battery is different during charging and discharging for a certain %SOC. Lastly, Chapter 3 provided an in-depth explanation for calculating the equivalent imepdance of a battery pack, which is useful in modeling a battery pack in simulation programs.

Chapter 4 provided an detailed comparison of three control techniques for the AC-DC converter. The results showed that the method with closed-loop control for power factor could not provide accurate power factor control and retuning of PI controller was necessary whenever a new power factor was desired. The method with open-loop control for power factor does not use a PI controller to track the power factor error, and it is able to provide more accurate power factor control. Furthermore, it was found that linear PI control techniques have nonzero steady-state error when tracking time-varying quantities, and tuning of the PI controllers based on the trial-and-error approach is a difficult task. The main advantage of using a synchronous frame controller is that all time-varying quantities are transformed into time invariant quantities, allowing the controller for the AC-DC converter to be designed in a manner similar to the controller for a DC-DC converter, achieving zero steady-state error. Simulations results also showed that the DQ controller could perform accurate power factor control. For these reasons, it was concluded that the DQ controller is a better technique for controlling a full-bridge AC-DC converter.

In Chapter 5, analysis was performed for six DC-DC topologies based on their in-

ductor size, voltage stress and component count. Comparison results showed that both the bidirectional buck-boost DC-DC converter and the full-bridge DC-DC converter were favourable topologies for the battery charger. The bidirectional buck-boost converter has a simple structure and lower component count in comparison with the full-bridge converter. However, the full-bridge converter provides more controllability and can handle higher power levels. Simulation results showed that the charger configuration that incorporates a bidirectional buck-boost has low voltage ripples at the dc-link and uses only two controllable switches. However, the two full-bridge converters configuration achieves lower current ripples and smoother transient response. The final decision on the topology type for the battery charger needs to be done based on a case study.

In Chapter 6, a lab proptotye of a full-bridge DC-DC converter was built, and experimental results demonstrated bidirectional power flow through three operation modes: CC charging, CV charging and CC discharging.

7.3 Future Work

The following items are proposed as future work for the bidirectional battery charger design:

- Building a lab prototype for a full-bridge AC-DC converter can be implemented to verify the performance of the DQ synchronous frame controller, even though simulation results revealed promising performance of the controller. Experimental results are also crucial for the analysis transient behaviour and converter efficiency.

- Noise reduction/elimination. The efficiency of the full-bridge DC-DC converter prototype can be improved by reducing noise in the waveforms. The high current ripples observed in the output waveforms have detrimental effects on the converter efficiency, and thus noise reduction is necessary to counteract these effects.

- Other DC-DC converter topologies and isolated topologies. This thesis has identified two DC-DC converter topologies that are suitable for the bidirectional battery charger, but there is room for research on other converter topologies that can improve the charger efficiency. Also, isolated topologies could be considered in order to provide extra safety measures required by the new standards, even though isolation transformers add to the overall weight.

- Round trip efficiency. In terms of overall efficiency of the battery charger, there is a need to investigate the round trip efficiency. A battery charger with a low round trip efficiency does not justify V2G power transactions.

APPENDICES

Appendix A

Battery Model Parameters Extraction Procedures

The experimental procedures described here are used to extract steady-state and transient parameters for the equivalent electrical circuit battery model. This set of procedures provides a rapid test to characterize the non-linear behaviour of lead-acid, nickel metal hydride and lithium-ion batteries, modified from [71]. It should be noted that the procedures outlined here are designed for a single battery cell. Additional cell balancing circuitry is required in order to apply the same procedures for a multi-battery pack. Furthermore, this set of procedures assumes that the battery temperature is controlled and maintained at a certain value by the battery management system.

A.1 Test System

The pieces of equipment required for the experiment are as follows:

- SOC meter
- Controllable source
- Controllable load
- Data acquisition unit (DAQ)

If the SOC meter works on the principle of coulomb counting, then it would need an initial SOC reference point. In this case, the reference point should be at 100% SOC so that it can be easily achieved by fully charging the battery cell.

A.2 Experimental Procedures

1. Charge the battery cell to 100% SOC. Different battery chemistries require different charging schemes. Refer to the battery datasheet for proper charging instructions.
2. Use a DAQ to record the %SOC and terminal voltage of the battery cell for the entire duration of the experiment. Using the experimental setup shown in Figure A.1(a), discharge the battery cell using a controllable load at 0.5C until SOC reduced by 5%.
3. At the end of the dissipation period, rest the battery cell for 30 minutes to allow it to recover its available capacity.
4. Repeat steps 2 and 3 until the SOC of the battery cell has reduced to 15%.
5. At this point, the experiment reverses its operation mode from discharging mode to charging mode. Using the experiment setup shown in Figure A.1(b), charge the battery cell using a controllable source at 0.5C and pause at the end of each interval marking a 5% increase in SOC.
6. Similarly to discharging mode, at each charging interval, allow the cell to rest for 30 minutes.
7. Repeat steps 5 and 6 until the battery cell's SOC reaches 100%.
8. Repeat steps 1 to 7 using different current levels. Allow at least 4 hours for the battery cell to rest between each experiment run.

A.3 Curve Fitting

Once all raw datapoints are collected, the next step is to perform curve fitting to obtain the model parameters' single-variable functions. Curve fitting can be done using the Curve

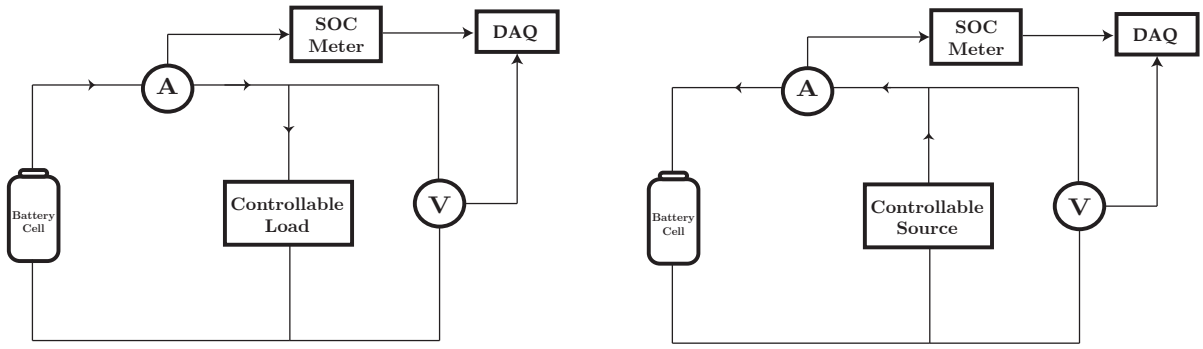

(a) Discharging a battery cell

(b) Charging a battery cell

Figure A.1: Experimental setup

Fitting Toolbox in Matlab. The toolbox requires two sets of datapoints, referred as X and Y. For this experiment, set X denotes to the set of all SOC datapoints and set Y contains the set of all terminal voltage datapoints for a single experiment run. Both datasets contain datapoints from V_1 until the end of the 30-minute recovery period. There is no pre-determined sampling frequency but a sufficient number of datapoints are needed to maintain the accuracy of the fitted curves.

The Matlab toolbox inherently contains many pre-loaded types of curve fitting. For this purpose, 'custom equation' should be selected for this type of curves. When a new custom equation is selected, the toolbox will show a new window with two tabs, labeled as "Linear Equations" and "General Equations". Under the "General Equations" tab, enter equations (3.2). The five variables a, b, c, d and e will automatically appear in the same window with three input boxes to enter the starting point, and lower and upper bounds for each unknown variable.

The objective in curve fitting is to fit a curve with a 95% confidence bound for all variables using the toolbox. Choosing an appropriate initial starting point, lower and upper bounds for each variable will accelerate the curve fitting process. Although the values of the variables are battery depended, one can set a reasonable boundary for variables b, d and e. Typically, the short-term time constant for a lithium-ion battery cell is in the range of tens of seconds while the long-term time constant is in hundreds of seconds. Variable e is the DC offset and thus, it should be the voltage level at which the fitted curve begins.

Once curve fitting is completed, the model parameters (R_{series}, $C_{transient_S}$, $R_{transient_S}$, $C_{transient_L}$ and $R_{transient_L}$) for a particular %SOC can be calculated using equations (3.3) to (3.6). This curve fitting procedure can be repeated for the datapoints collected for each charging/discharging level. The single-variable function for each model parameter can be obtained by first taking an average of the calculated values for a particular %SOC. Then, combining the datapoints for all %SOC, perform curve fitting again using the equation format described in equations (3.7) to (3.11).

Appendix B

Converter Prototype Implementation Details

B.1 Hardware Implementation

The hardware implementation of the lab prototype involved component selection and the design of the sensing circuits. The following discussion provides an overview of the selected components' characteristics used in the lab prototype and a detailed analysis on the sensing circuitry.

B.1.1 DSP Microcontroller

Texas Instrument TMS320F2808 32-Bit Digital Signal Processor (DSP) was chosen as the microcontroller for the lab prototype. The attractive features of this DSP include fast CPU (100MHz), 128KB of Flash memory, 16 PWM outputs, 35 GPIO channels, 16 channels of 12-bit ADC with a high conversion rate (160ns), and floating point calculation support. The TMS320F2808 Experimenter Kit was chosen to use alongside with the DSP for quick prototyping and testing. This experimenter kit has a docking station with access to all signals, and features on-board USB JTAG emulation.

B.1.2 IGBT Switches and Gate Drivers

The switches for the battery charger were implemented using Powerex CM150DUS-12F insulated-gate bipolar transistor (IGBT) modules. Each module consists of two IGBTs in a half-bridge configuration with each transistor having a reverse-connected super-fast recovery freewheeling diode. Furthermore, each transistor is rated at 600 volts and 150 amperes.

In order to protect the IGBTs from excessive transient voltage and high dv/dt, a metal-oxide varistor (MOV) with a clamping voltage of 390V and a 0.1F snubber capacitor were placed in parallel with collector-emitter terminals of each IGBT.

The Powerex BG2C Universal Gate Drive Prototype Board was selected to provide the gate signal needed to drive the IGBT modules. Each prototype board contains a two-channel gate drive circuit, which utilizes two Powerex VLA507 hybrid gate drivers and two Powerex VLA106-15242 DC-to-DC converters. The DC-to-DC converters are intended to provide fully isolated control power for each driving channel.

The functional block diagrams of the hybrid gate drive and DC-to-DC converter are shown in Figure B.1(a) and B.1(b), respectively. The drivers use opto-couplesr to provide isolation for the control signals. The DC-to-DC converter operates from a 15VDC input and uses a transformer to provide isolation for the gate drive power. A regulated 24VDC output is split using a resistor and a zener diode to provide +15.8V and -8.2V for the hybrid gate driver [72].

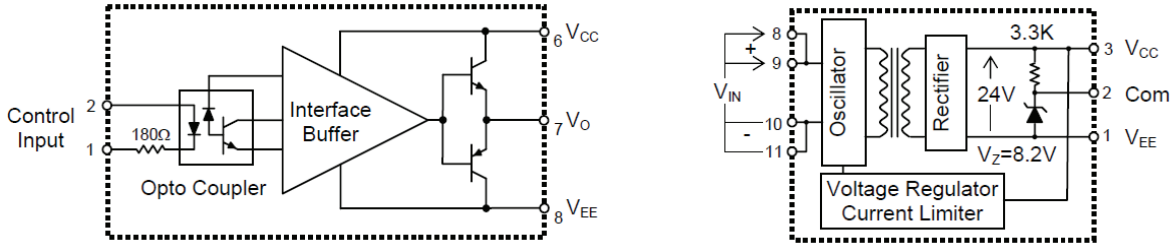

(a) Hybrid gate driver

(b) DC-to-DC converter

Figure B.1: Block diagrams of the gate driver and the isolated DC-to-DC converter

Apart from the series gate resistance (R_g), all the components on the gate driver proto-

type board were selected based on the recommendations provided in the application notes. The value of R_g has significant impact of the dynamic performance of the IGBT. In this application, R_g is designed to be 10Ω to have a good compromise between switching speed and dv/dt.

Figure B.2 shows the wiring diagrams for the gate driver prototype board. The control input signals, IN1 and IN2, are standard 5V CMOS logic and are used to control IGBTs 1 and 2, respectively. These signals are active low signals, meaning that the IGBTs are turned off when these signals are pulled high. A CMOS buffer (TI74HC04) was used to actively pull these signals low in the on state and to filter out noise pollution.

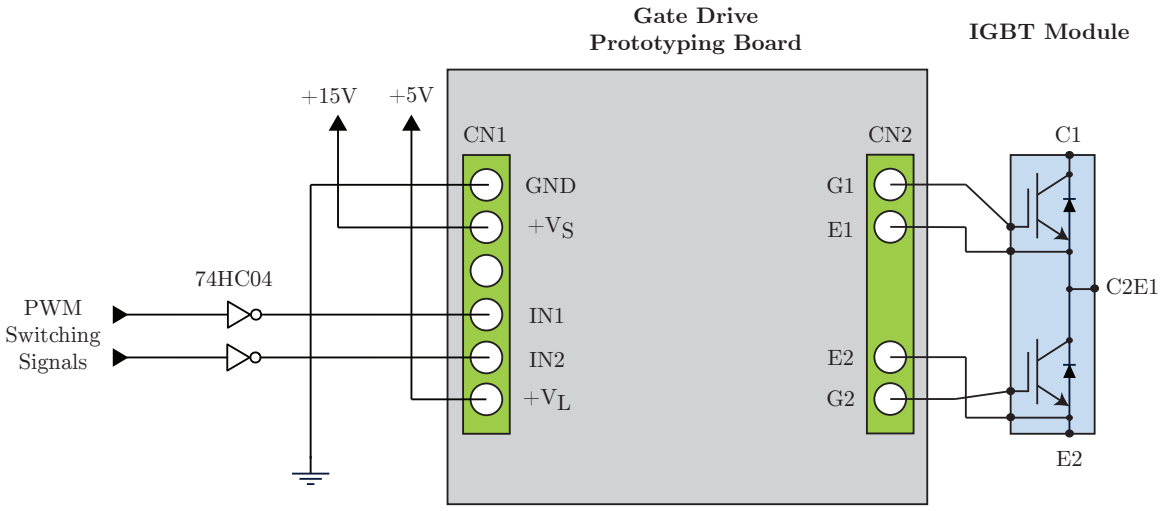

Figure B.2: Gate driver prototype board wiring diagram

B.1.3 Battery

Genesis Purelead EP lead-acid batteries were used to form the battery pack and act as the DC-link voltage source for bidirectional power flow demonstration. Each Genesis battery has a capacity of 13Ah and the plot in Figure B.3 is used to accurately estimate the remaining charge in the battery by correlating the open-circuit voltage with the %SOC [73].

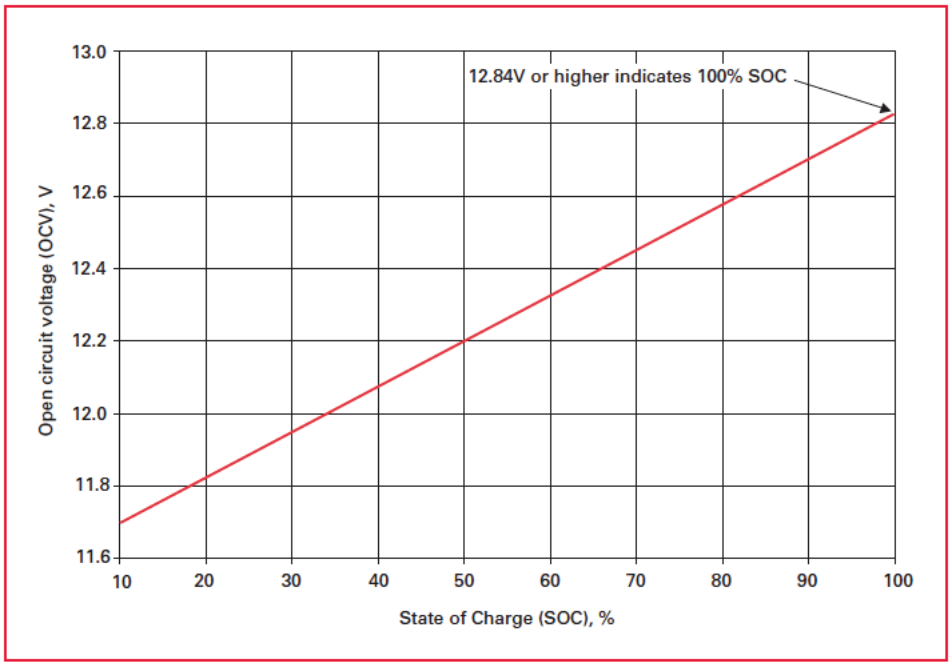

Figure B.3: Open circuit voltage vs. state of charge

B.1.4 Capacitors

The capacitor used on the dc-link is a 2.4mF, 500VDC electrolytic capacitor with a current ripple limit of ±11A. The capacitor used on the battery side is a 1mF, 500VDC electrolytic capacitor with a current ripple limit of ±11.7A. Both capacitors are manufactured by DuraCap. These capacitance values were selected based on the capacitance values used in simulation and the current ripples processed by the capcitances shown in simulation results.

B.1.5 Inductors

The inductor used at the battery terminal side is rated at 1mH. This inductance value was selected since it is the closest inductance value available in the lab to the 0.5mH inductor used in simulations.

B.1.6 DC Voltage Sensing Circuit

The circuit in Figure B.4 was used to sense dc-link voltage and battery voltage. The DC voltage is first given to a voltage divider to produce an output voltage of 3V DC maximum, as required for the DSP ADC channels. The ratio of the fixed reistaor and potentiometer determines the input voltage range that the sensing circuit can process. Following the voltage divider, the scaled-down voltage goes through a voltage follower for unity-gain buffering. Other than the low-pass filter (LPF), the rest of the circuit is for analog isolation purposes. The HCNR200 from Avago Technolgoies is selected as the high-linearity analog optocoupler for isolation. Due to analog isolation, two isolated power supplies were needed. One +5VDC supply was used for the portion of the circuit up to the input photodiode and another +5VDC supply was used for the portion of the circuit from the output photodiode to the low-pass filter. The 650kΩ potentiometer was adjusted to ensure the gain from the voltage follower to the low-pass filter is unity. The low-pass filter was designed to have a corner frequency of 9.9kHz to filter out high-frequency noise. U1 is an Analog Devices AD8032 dual amplifier and was chosen to save board space. Finally, U2 is an Analog Device AD8031 single amplifier.

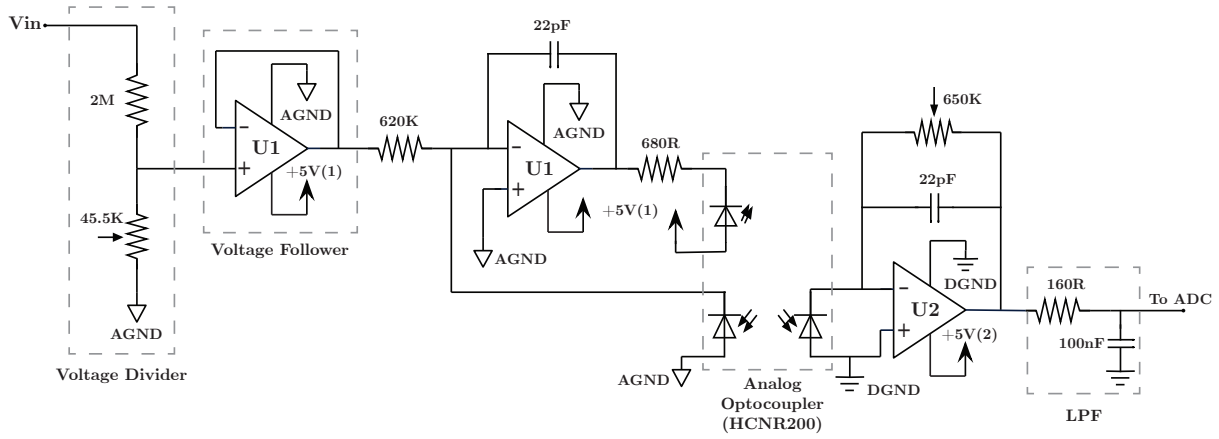

Figure B.4: DC voltage sensing circuit

B.1.7 Current Processing Circuit

Control of the DC-DC converter requires current feedback from the current at the battery terminals. Current measurement was done using LEM current transducer CAS 15-NP. The current transducer provides galvanic isolation, so no additional isolation circuit is required. It has a measuring range from -51A to 51A with an output voltage from 0.375V to 4.625V. Because the output voltage range is beyond what the ADC channels can accept and the transducer would load the ADC channels if they are directly connected, a voltage scaling and decoupling circuit is required. Figure B.5 shows the current processing circuit.

The processing circuit begins and ends with a low-pass filter for decoupling and filtering purposes. Equations (B.1) and (B.2) illustrate the voltage at the negative and positive inputs of the amplifier U3. The design of the voltage divider prior to U3 was based on the fact that both voltages at the input terminals of U3 should be equal and the ratio between V_1 and V_2 is 5:3.

$$\text{Negative op-amp input: } \frac{V_2 \times 51K}{51K + 51K} = \frac{1}{2}V_2 \tag{B.1}$$

$$\text{Positive op-amp input: } \frac{V_1 \times 300K}{700K + 300K} = \frac{3}{10}V_1 \tag{B.2}$$

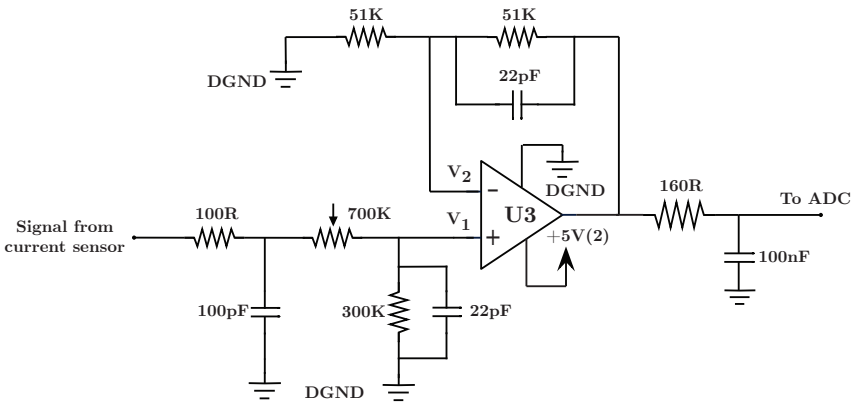

Figure B.5: Current processing circuit

B.2 Software Implementation

Software development for TMS320F2808 is performed using Code Composer Studio IDE in C language. The microcontroller is responsible for real-time data acquisition and manipulation, control algorithm computation, switching signal generation, and system protection.

B.2.1 ADC Calibration

The 12-bit ADCs found in DSP inherently have gain and offset errors that affect the accuracy of the ADCs. Figure (B.6) shows the plot of the ideal and actual gain of an ADC. The ideal gain has a one-to-one linear relationship between the input and output with no offset, as described by equation (B.3). However, in the actual case, the ADC exhibits gain and offset errors, which are governed by equation (B.4).

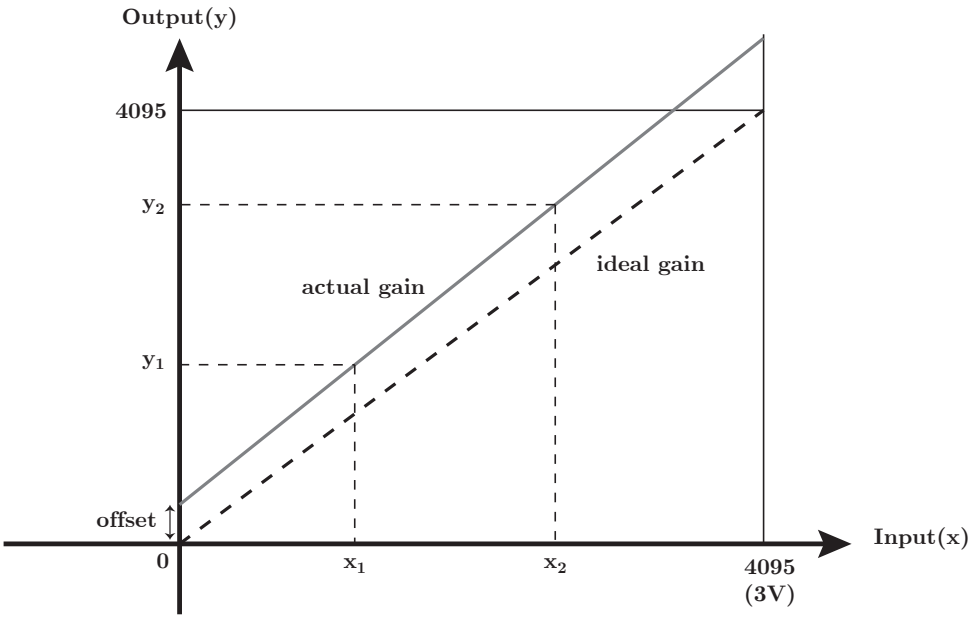

Figure B.6: Ideal and actual gain of ADC

$$y = x \tag{B.3}$$

$$y = a_a x + b_a \tag{B.4}$$

ADC calibration is required in order to compensate for the errors caused of non-unity gain and offset. The objective of ADC calibration is to find a multiplier δ and an offset γ, such that

$$\delta(a_a x + b_a) + \gamma = x \tag{B.5}$$

In order to solve for δ and γ it is desirable to solve equations B.6 and B.7.

$$a_a \delta = 1 \tag{B.6}$$

$$b_a \delta + \gamma = 0 \tag{B.7}$$

Figure B.7 shows the block diagram of signal sensing process. The calibration process begins by calculating the ideal ratio between the sensed analog signal to the DSP digital value, as given in equation (B.8). The input range is the range of values that the voltage sensing circuit or the current transducer can process. For example, if the voltage sensing circuit has a sensed range from 0 to 100V then the input range would be 100. If the current transducer has a measuring range from -51A to 51A, then the value for input range would be 102. The value 4096 represents the number of discrete values a 12-bit ADC has, and the value 3 represents the analog input of the ADC. After solving for multiplier δ and offset γ, the actual ratio between the sensed analog signal to the DSP digital value can be calculated using equation (B.9).

Figure B.7: Block diagram of signal sensing process

$$\text{Ideal Ratio } = R_{ideal} = \frac{\text{Input Range}}{3} \times \frac{3}{4096} \tag{B.8}$$

$$\text{Actual Ratio } = R_{actual} = \delta \cdot R_{ideal} - \gamma \tag{B.9}$$

References

[1] J. Wood, G. Long, and D. Morehouse, "Long-Term World Oil Supply Scenarios: The Future Is Neither as Bleak or Rosy as Some Assert," 2004. [Online]. Available: http://www.eia.gov/pub/oil_gas/petroleum/feature_articles/2004/worldoilsupply/oilsupply04.html

[2] Department of Infrastructure, Transport, Regional Development and Local Government, "Transport energy futures: long-term oil supply trends and projections. Report 117," March 2009. [Online]. Available: http://www.manicore.com/fichiers/Australian_Govt_Oil_supply_trends.pdf

[3] "Historial Crude Oil Prices," June 2012. [Online]. Available: http://inflationdata.com/inflation/inflation_rate/historical_oil_prices_table.asp

[4] N. Haluzan, "Pollution from fossil fuels facts," January 2011. [Online]. Available: http://pollutionarticles.blogspot.ca/2011/01/pollution-from-fossil-fuels-facts.html

[5] Intergovermental Panel on Climate Change, "Renewable Energy Sources and Climate Change Mitigation: Special Report of the Intergovermental Panel on Climate Change," 2012. [Online]. Available: http://srren.ipcc-wg3.de/report/IPCC_SRREN_Full_Report.pdf

[6] D. Tencer, "Number Of Cars Worldwide Surpasses 1 Billion; Can The World Handle This Many Wheels?" October 2011. [Online]. Available: http://www.huffingtonpost.ca/2011/08/23/car-population_n_934291.html

[7] S. Han and D. Divan, "Bi-Directional DC/DC Converters for Plug-in Hybrid Electric Vehicle (PHEV) Applications," in *Applied Power Electronics Conference and Exposition (APEC), 2008. 23rd Annual IEEE*, Feb 2008, pp. 784–789.

[8] "Electric Vehicles (EVs)," July 2012. [Online]. Available: http://www.fueleconomy.gov/feg/evtech.shtml/

[9] A. Khaligh, "Plug-In Hybrid Electric Vehicles: Sustainable Driving to 21st Energy Future," Illinois Institute of Technology, Tech. Rep., 2010.

[10] K. Morrow, D. Karner, and J. Fracfort, "Plug-in hybrid electric vehicle charging infrasture review," U.S. Department of Energy Vehicle Technologies Program, Tech. Rep., Nov 2008.

[11] Hybridcenter.org, "Hybrids Under the Hood (part 2)," 2010. [Online]. Available: http://www.hybridcenter.org/hybrid-center-how-hybrid-cars-work-under-the-hood-2.html

[12] S. S. Raghavan, O. C. Onar, and A. Khaligh, "Power Electronic Interfaces for Future Plug-in Transportation Systems," in *IEEE Power Electronics Society Newsletter*, 2010, pp. 23–26.

[13] M. Kisacikoglu, B. Ozpineci, and L. Tolbert, "Examination of a PHEV bidirectional charger system for V2G reactive power compensation," in *Applied Power Electronics Conference and Exposition (APEC), 2010. 25th Annual IEEE*, Feb 2010, pp. 458–465.

[14] ——, "Effects of V2G Reactive Power Compensation on the Component Selection in an EV or PHEV Bidirectional Charger," in *Energy Conversion Congress and Exposition (ECCE), 2010 IEEE*, Sep 2010, pp. 870–876.

[15] ——, "Reactive Power Operation Analysis of a Single-Phase EV/PHEV Bidirectional Battery Charger," in *Power Electronics and ECCE Asia (ICPE & ECCE), 2011 IEEE 8th International Conference on*, May 2011, pp. 585–592.

[16] Waterloo Institute for Sustainable Energy, University of Waterloo, "Towards an Ontario Action Plan for Plug-In-Electric Vehicles," May 2010. [Online]. Available: http://plugndriveontario.ca/pdf/Waterloo%20PHEV%20Report%20June%202010%20FINAL.pdf

[17] C. Chan and K. Chau, "An overview of power electronics in electric vehicles," *Industrial Electronics, IEEE Transactions on*, vol. 44, no. 1, pp. 3–13, Feb 1997.

[18] I. Khan, "Battery chargers for electric and hybrid vehicles," in *Power Electronics in Transportation, 1994. Proceedings.*, Oct 1994, pp. 103–112.

[19] B. Singh, B. Singh, A. Chandra, K. Al-Haddad, A. Pandey, and D. Kothari, "A review of single-phase improved power quality AC-DC converters," *Industrial Electronics, IEEE Transactions on*, vol. 50, no. 5, pp. 962–981, Oct 2003.

[20] B. Lin, D. Chen, and H. Tsay, "Bi-Directional AC/DC Converter Based on Neutral Point Clamped," in *Industrial Electronics (ISIE), 2001. Proceedings. IEEE International Symposium on*, vol. 1, 2001, pp. 619–624.

[21] J. Boys and A. Green, "Current-forced single-phase reversible rectifier," *Electric Power Applications, IEE Proceedings B*, vol. 136, no. 5, pp. 205–211, Sep 1989.

[22] M. Cirrincione, M. Pucci, and G. Vitale, "Current harmonic compensation by a single-phase shunt active power filter controlled by adaptive neural filtering," *Industrial Electronics, IEEE Transactions on*, vol. 56, no. 8, pp. 3128–3143, Aug 2009.

[23] B. Lin, D. Chen, and T. Hung, "Half-bridge neutral point diode clamped rectifier for power factor correction," *Aerospace and Electronic Systems, IEEE Transactions on*, vol. 38, no. 4, pp. 1287–1294, Oct 2002.

[24] B. Lin and T. Hung, "Single-phase half-bridge converter topology for power quality compensation," *Electric Power Applications, IEE Proceedings-*, vol. 149, no. 5, pp. 351–359, Sep 2002.

[25] B. Lin, T. Hung, and C. Huang, "Bi-directional single-phase half-bridge rectifier for power quality compensation," *Electric Power Applications, IEE Proceedings-*, vol. 150, no. 4, pp. 397–406, Jul 2003.

[26] B. Lin and T. Yang, "Single-phase half-bridge rectifier with power factor correction," *Electric Power Applications, IEE Proceedings-*, vol. 151, no. 4, pp. 443–450, Jul 2004.

[27] P. Krein, "Electrostatic discharge issues in electric vehicles," *Industry Applications, IEEE Transactions on*, vol. 32, no. 6, pp. 1278–1284, Nov 1996.

[28] S. Vaishnav and H. Krishnaswami, "Single-stage isolated bi-directional converter topology using high frequency AC link for charging and V2G applications of PHEV," in *Vehicle Power and Propulsion Conference (VPPC), 2011 IEEE*, Sep 2011, pp. 1–4.

[29] A. Verma, B. Singh, and D. Shahani, "Grid to vehicle and vehicle to grid energy transfer using single-phase bidirectional AC-DC converter and bidirectional DC-DC converter," in *Energy, Automation, and Signal (ICEAS), 2011 International Conference on*, Deb 2011, pp. 1–5.

[30] B. Bilgin, A. Emadi, and M. Krishnamurthy, "Design considerations for a universal input battery charger circuit for PHEV applications," in *Industrial Electronics (ISIE), 2010 IEEE International Symposium on*, Jul 2010, pp. 3407–3412.

[31] ——, "Universal input battery charger circuit for PHEV applications with simplified controller," in *Applied Power Electronics Conference and Exposition (APEC), 2011 26th Annual IEEE*, Mar 2011, pp. 815–820.

[32] T. Kato and K. Miyao, "Modified hysteresis control with minor loops for single-phase full-bridge inverters," in *Industry Applications Society Annual Meeting, 1988., Conference Record of the 1988 IEEE*, Oct 1988, pp. 689 –693 vol.1.

[33] F. Peng, W. Zhu, K. Zhou, and M. Cheng, "A full-bridge full-wave high frequency link inverter with active clamper and its control," in *Electrical and Control Engineering (ICECE), 2011 International Conference on*, Sep 2011, pp. 4246 –4249.

[34] W. Haitao, S. Yize, and P. Lele, "Binary particle swarm optimization algorithm for control of single-phase full-bridge inverter," in *Power and Energy Engineering Conference (APPEEC), 2010 Asia-Pacific*, Mar 2010, pp. 1 –4.

[35] Z. Xuhui, X. Wen, Z. Feng, and G. Xinhua, "A new control strategy for bi-directional dc-dc converter in electric vehicle," in *Electrical Machines and Systems (ICEMS), 2011 International Conference on*, Aug 2011, pp. 1 –4.

[36] X. Zhou, S. Lukic, S. Bhattacharya, and A. Huang, "Design and control of grid-connected converter in bi-directional battery charger for Plug-in hybrid electric vehicle application," in *Vehicle Power and Propulsion Conference (VPPC), 2009. IEEE*, Sep 2009, pp. 1716–1721.

[37] X. Zhou, G. Wang, S. Lukic, S. Bhattacharya, and A. Huang, "Multi-function bi-directional battery charger for plug-in hybrid electric vehicle application," in *Energy Conversion Congress and Exposition (ECCE), 2009. IEEE*, Sep 2009, pp. 3930–3936.

[38] D. Segaran, D. G. Holmes, and B. P. McGrath, "High-performance bi-directional AC-DC converters for PHEV with minimised DC bus capacitance," in *IECON 2011 - 37th Annual Conference on IEEE Industrial Electronics Society*, Nov 2011, pp. 3620–3625.

[39] Y. Lee, A. Khaligh, and A. Emadi, "Advanced Integrated Bidirectional AC/DC and DC/DC Converter for Plug-In Hybrid Electric Vehicles," *Vehicular Technology, IEEE Transactions on*, vol. 58, no. 8, pp. 3970–3980, Oct 2009.

[40] D. Erb, O. Onar, and A. Khaligh, "Bi-directional charging topologies for plug-in hybrid electric vehicles," in *Applied Power Electronics Conference and Exposition (APEC), 2010. 25th Annual IEEE*, Feb 2010, pp. 2066–2072.

[41] ——, "An integrated bi-directional power electronic converter with multi-level AC-DC/DC-AC converter and non-inverted buck-boost converter for PHEVs with minimal grid level disruptions," in *Vehicle Power and Propulsion Conference (VPPC), 2010 IEEE*, Sep 2010, pp. 1–6.

[42] S. Lacroix, E. Laboure, and M. Hilairet, "An integrated fast battery charger for electric vehicle," in *Vehicle Power and Propulsion Conference (VPPC), 2010 IEEE*, Sept 2010, pp. 1 –6.

[43] G. Pellegrino, A. Vagati, P. Guglielmi, and B. Boazzo, "Performance comparison between surface-mounted and interior PM motor drives for electric vehicle application," *Industrial Electronics, IEEE Transactions on*, vol. 59, no. 2, pp. 803–811, Feb 2012.

[44] E. Sulaiman, T. Kosaka, and N. Matsui, "High power density design of 6-slot-8-pole hybrid excitation flux switching machine for hybrid electric vehicles," *Magnetics, IEEE Transactions on*, vol. 47, no. 10, pp. 4453–4456, Oct 2011.

[45] M. Hasegawa, S. Yoshioka, and K. Matsui, "Position sensorless control of interior permanent magnet synchronous motors using unknown input observer for high-speed drives," *Industrial Applications, IEEE Transactions on*, vol. 45, no. 3, pp. 938–946, May 2009.

[46] R. Surada and A. Khaligh, "A novel approach towards integration of propulsion machine inverter with energy storage charger in plug-in hybrid electric vehicles," in *IECON 2010 - 36th Annual Conference on IEEE Industrial Electronics Society*, Nov 2010, pp. 2493–2498.

[47] O. Hegazy, J. Van Mierlo, and P. Lataire, "Design and control of bidirectional DC/AC and DC/DC converters for plug-in hybrid electric vehicles," in *Power Engineering, Energy and Electrical Drives (POWERENG), 2011 International Conference on*, May 2011, pp. 1–7.

[48] S. Haghbin, K. Khan, S. Lundmark, M. Alaküla, O. Carlson, M. Leksell, and O. Wallmark, "Integrated chargers for EV's and PHEV's: examples and new solutions," in *Electrical Machines (ICEM), 2010 XIX International Conference on*, Sep 2010, pp. 1–6.

[49] S. Haghbin, S. Lundmark, M. Alakula, and O. Carlson, "Grid-connected integrated battery chargers in vehicle applications: Review and new solution," *Industry Applications, IEEE Transactions on*, Early Access 2012.

[50] S. Haghbin, M. Alakula, K. Khan, S. Lundmark, M. Leksell, and O. Wallmark, "An integrated charger for plug-in hybrid electric vehicles based on a special interior permanent magnet motor," in *Vehicle Power and Propulsion Conference (VPPC), 2010 IEEE*, Sep 2010, pp. 1–6.

[51] LEAF WIKI, "Battery, Charging System," Sep 2011. [Online]. Available: http://nissanleafwiki.com/index.php?title=Battery,_Charging_System

[52] L. D. Roper, "Chevy Volt," Jun 2012. [Online]. Available: http://www.roperld.com/science/ChevyVolt.htm

[53] InfoBarrel, "Toyota Prius Battery Life," May 2012. [Online]. Available: http://www.infobarrel.com/Toyota_Prius_Battery_Life

[54] "IEEE standard for interconnecting distributed resources with electric power systems," *IEEE Std 1547-2003*, pp. 1 –16, 2003.

[55] F. V. Conte, "Battery and battery management for hybrid electric vehicles: a reivew," in *Eletrotechnik & Informationstechnik*, Sep 2006, pp. 424–431.

[56] C. Lampton, "How Electric Car Batteries Work," 2012. [Online]. Available: http://auto.howstuffworks.com/fuel-efficiency/vehicles/electric-car-battery1.htm

[57] U.S. Department of Energy, "Batteries for Hybrid and Plug-In Electric Vehicles," Jul 2012. [Online]. Available: http://www.afdc.energy.gov/vehicles/electric_batteries.html

[58] A123 Systems, "Lithium Battery Products," 2012. [Online]. Available: http://www.a123systems.com/lithium-battery.htm

[59] Z. Chen, Z. Nie, Y. Fu, and C. Mi, "A bidirectional power converter for battery of plug-in hybrid electric vehicles," in *IECON 2010 - 36th Annual Conference on IEEE Industrial Electronics Society*, Nov 2010, pp. 3049–3053.

[60] T. Kim and W. Qiao, "A hybrid battery model capable of capturing dynamic circuit characteristics and nonlinear capacity effects," *Energy Conversion, IEEE Transactions on*, vol. PP, no. 99, pp. 1 –9, 2011.

[61] S. B. Kjaer, J. K. Pedersen, and F. Blaabjerg, "A Review of Single-Phase Grid-Connected Inverters for Photovoltaic Modules," *Industrial Applications, IEEE Transactions on*, vol. 41, no. 5, pp. 1292–1306, Sep 2005.

[62] J. Benjanarasut and B. Neammanee, "The d-, q-axis Control Technique of Single Phase Grid Connected Converter for Wind Turbines with MPPT and Anti-Islanding Protection," in *Electrical Engineering/Electronics, Computer, Telecommunications and Information Technology (ECTI-CON), 2001. 8th International Conference on*, May 2011, pp. 649–652.

[63] P. Barbosa, L. Rolim, E.H.Watanabe, and R. Hanitsch, "Control strategy for grid-connected DC-AC converters with load power factor correction." Generation, Transmission and Distribution. IEEE Proceedings, Sep 1998, pp. 487–491.

[64] J. Salaet, S. Alepuz, A. Gilabert, J. Bordonau, and J. Peracaula, "D-Q Modeling and Control of a Single-Phase Three-Level Boost Rectifier with Power Factor Correction and Neutral-Point Voltage Balancing," in *Power Electronics Specialists COnference, 2002. IEEE 33rd Annual*, 2001, pp. 514–519.

[65] A. Roshan, R. Burgos, A. C. Baisden, F. Wang, and D. Boroyevich, "A D-Q Frame Controller for a Full-Bridge Single Phase Inverter Used in Small Distributed Power Generation Systems," in *Applied Power Electronics Conference and Exposition (APEC), 2007. 22th Annual IEEE*, Feb 2007, pp. 641–647.

[66] U. Miranda, M. Aredes, and L. Rolim, "A DQ Synchronous Reference Frame Control for Single-Phase Converters." Power Electronics Specialists Conference (PESC), 2005. IEEE 36th, Jun 2005, pp. 1377–1381.

[67] B. Bahrani and A. Rufer, "Vector Control of Single-Phase Voltage-Source Converters Based on Fictive-Axis Emulation," *Industrial Applications, IEEE Transactions on*, vol. 47, no. 2, pp. 831–840, Mar 2011.

[68] R. Schupbach and J. Balda, "Comparing DC-DC Converters for Power Management in Hybrid Electric Vehicles." Electric Machines and Drives Conference (IEMDC), 2003. IEEE Internation, Jun 2003, pp. 1369–1374.

[69] Y. Du, X. Zhou, S. Bai, S. Lukic, and A. Huang, "Review of Non-isolated Bi-directional DC-DC Converters for Plug-in Hybrid Electric Vehicle Charge Station Application at Municipal Parking Decks," in *Applied Power Electronics Conference and Exposition (APEC), 2010. 25th Annual IEEE*, Feb 2010, pp. 1145–1151.

[70] EV Assemble, "Elcon 8000W HF/PFC LiFePO4 Charger," 2012. [Online]. Available: http://www.evassemble.com/index.php?main_page=product_info&cPath=3&products_id=27

[71] S. Abu-Sharkh and D. Doeffel, "Rapid test and non-linear model characterisation of solid-state lithium-ion batteries," vol. 130, 2004, pp. 266–274.

[72] Powerex, "Application Notes: BG2C - Universal Gate Drive Prototype Board," Feb 2006. [Online]. Available: http://www.pwrx.com/pwrx/docs/bg2c.pdf

[73] *Genesis Purelead XE and EP Application Manual*, 7th ed. Enersys, Sep 2006.